CENTRO DE INVESTIGACIÓN Y DE ESTUDIOS AVANZADOS
DEL INSTITUTO POLITÉCNICO NACIONAL
UNIDAD MÉRIDA
DEPARTAMENTO DE FÍSICA APLICADA

Electron Dynamics in Anisotropic Dirac Materials: Homogeneously Strained Graphene

Tesis que presenta

Yonatan Betancur Ocampo

para obtener el grado de

Doctor en Ciencias

en la especialidad de

Física Teórica

dirigida por:

Dr. Romeo Humberto de Coss Gómez

Mérida, Yucatán, México. Marzo de 2017.

CENTRO DE INVESTIGACIÓN Y DE ESTUDIOS AVANZADOS
DEL INSTITUTO POLITÉCNICO NACIONAL
UNIDAD MÉRIDA
DEPARTAMENTO DE FÍSICA APLICADA

Dinámica de Electrones en Materiales de Dirac Anisotrópicos: Grafeno Tensionado Homogéneamente

Tesis que presenta

Yonatan Betancur Ocampo

para obtener el grado de

Doctor en Ciencias

en la especialidad de

Física Teórica

dirigida por:

Dr. Romeo Humberto de Coss Gómez

Mérida, Yucatán, México. Marzo de 2017.

Dedicado con amor a mis hijos
Yeudiel Isai y Jair Iona Betancur Arjona,
y a mi esposa
Danahí Suhail Arjona Maldonado.

Acknowledgements

I would like to thank my advisor Dr. Romeo de Coss Gómez, whose teaching, time, criticism, and suggestions, this thesis would have not been possible. His patience, enthusiasm, and knowledge were useful in my research activity. Also, I would like to thank my doctoral committee which were conformed by Dr. José Ángel Méndez Gamboa, Dr. Víctor Sosa Villanueva, Dr. Francisco Carlos Larios Forte, and Dr. José Gabriel Merino Hernández. Their valuable contributions allowed to improve the quality of this thesis. A special thanks to Dr. Guillermo Coudourier Maruri, who made important suggestions in the proofreading.

I gratefully acknowledge the funding support given by the Consejo Nacional de Ciencia y Tecnología (Conacyt), without the scholarship my PhD physics studies at Cinvestav-Mérida would have been impossible. Also, I thank to Dr. Virendra Gupta and Dr. Romeo de Coss for his funding support when the PhD scholarship finished. I thank the friendly support of the members staff of Applied Physics Department at Cinvestav-Mérida. I thank to Dr. Geonel Rodríguez Gattorno for his invaluable help and encouregement in the conclusion of my PhD studies. Thank you to Dr. Cristina Vargas, Dr. Víctor Sosa, Dr. José Mustre de León, Dr. Antonio Bouzas, Dr. Juan José Alvarado, Dr. Francisco Larios, Dr. Román Castro, Dr. Pascual Bartolo, and Dr. Cristian Moukarzel for their contributions in my academic training. Many thanks to Zhirnay Rodríguez, Yolanda Acosta, María Antonienta Martínez, Monserrat Solís, and Sofía Alonzo, their work helped me much over the years. I would like to thank my fellow group members: Carlos Ramos, Miguel Cifuentes, Maryel Contreras, Juan Pech, Raúl Duarte, and Guillermo Cordourier for his friendship and inspiring conversations.

Finally, I wish to thank my family for their invaluable help and understanding. I would like to thank my wife and sons for their love and encouraging me to overcome difficulties. I thank to my family from Colombia, Mexico and Switzerland for their support.

Agradecimientos

Agradezco a Dios por la vida y todos los favores que he recibido, de darme una familia, amistades y la oportunidad de vivir experiencias edificantes que me han permitido crecer personal, emocional y espiritualmente. Conocer personas que tendré en mi memoria por el resto de mis días. El llegar a un lugar que, en un comienzo, no me había imaginado estar, conocer su gente, su cultura y tradiciones maravillosas, como lo ha sido México para mí, en especial la ciudad de Mérida. Conocer y compartir con tantas personas valiosas en estos siete años y medio de estar en el Cinvestav-Mérida, que si los nombrara ocuparía muchas páginas de esta tesis.

Agradezco al Conacyt por darme una beca para la realización de mis estudios de Doctorado, la cual me ha sido de gran ayuda en la manutención personal y familiar. Muchas gracias al Cinvestav y Conacyt por el apoyo brindado en la asistencia a congresos. Al Dr. Virendra Gupta y Dr. Romeo de Coss Gómez por su apoyo económico después de terminada la beca de doctorado. Al Dr. Geonel Rodríguez Gattorno por su labor como coordinador académico, por ayudarme en lo personal y animarme a concluir la última parte en el proceso de titulación, así como en la elaboración del trámite de renovación anual de la visa ante el Instituto Nacional de Migración. También, doy mis agradecimientos a Zhirnay Rodríguez, Yolanda Acosta, María Antonienta Martínez, Monserrat Solís, y Sofía Alonzo, cuyo trabajo ha sido de gran ayuda en todos los trámites académicos.

Agradezco al Dr. Romeo de Coss Gómez quien es mi asesor de tesis de Doctorado en la especialidad de Física Teórica, que sin su ayuda, tiempo, críticas, enseñanzas y sugerencias esta tesis estaría lejana de ser el trabajo que es. Al comité sinodal conformado por el Dr. José Ángel Méndez Gamboa, Dr. Víctor Sosa Villanueva, Dr. Francisco Carlos Larios Forte, y el Dr. José Gabriel Merino Hernández, cuyos aportes permitieron mejorar la calidad del trabajo de esta tesis. Al Dr. Guillermo Cordourier Maruri por su revisión detallada e importantes sugerencias en la elaboración del escrito. A mis compañeros del grupo: Carlos Ramos, Miguel Cifuentes, Maryel Contreras, Juan Pech, Raúl Duarte y Guillermo Cordourier por sus reflexiones acerca de mi trabajo y por brindarmen su amistad. A los Profesores del Cinvestav-Mérida: Dra. Cristina Vargas, Dr. Víctor Sosa, Dr. José Mustre de León, Dr. Antonio Bouzas, Dr. Juan José Alvarado, Dr. Francisco Larios, Dr. Román Castro, Dr. Pascual Bartolo, y Dr. Cristian Moukarzel por dedicar su tiempo en mi formación académica durante la realización de mis estudios de Maestría y por ofrecermen su apoyo en momentos críticos. Un especial agradecimiento a Raúl Duarte, Maryel Contreras y Juan Pech por ayudarmen en momentos económicos difíciles.

Por último, quiero agradecer a mi esposa Danahí Suhail Arjona Maldonado y a mis hijos Yeudiel Isai y Jair Iona por todo su amor y felicidad que me dan, por todos los momentos inolvidables buenos y difíciles que hemos vivido, en ustedes encontré lo que buscaba, y he recibido como regalo el valor y la fuerza para afrontar los retos de la vida. Agradezco a mi suegra, Lilia Maldonado López por ayudarme en múltiples ocasiones, he recibido de su parte el mismo trato que se le da a un hijo. A mi tía Patricia por su ayuda durante varios años. Agradezco a mis padres Jairo de Jesús Betancur Arcila y María Miriam Ocampo Correa por su amor, felicidad, educación, salud, apoyo económico y moral que me han dado por tantos años, a quienes extraño mucho desde la distancia, al igual que a mis hermanos y demás familiares que se encuentran en Colombia.

Abstract

In recent years, a fruitful research topic in condensed matter combining relativity theory and quantum electrodynamics ideas has emerged in a new class of materials called Dirac materials, which constitute an important platform in the realization of effective models inspired in the quantum field theory. These materials provide an interesting feedback between condensed matter and fundamental physics. Whereas the introdcution of anisotropy and inhomogeneity in such systems lead to a wide variety of phenomena and applications so far unexplored. Thus, in this thesis the effect of anisotropy and inhomogeneity on electron dynamics in Dirac materials is studied using a Geometrical Approach (GA), which provides a direct understanding of the electronic properties derived from an effective hamiltonian describing massless Dirac fermions. Due to the anisotropy, some of these Dirac materials show in their low-energy electronic structure, a distorted Dirac cone whose geometrical parameters are captured from an effective hamiltonian Dirac. This is a generalization of the Dirac-like hamiltonian known in pristine graphene. This hamiltonian has a parameter set with defined geometrical meaning, introduced through a canonical transformation of the linear momentum. The parameters can be determined fitting of electronic band structure from ab-initio calculations, as well as from available experimental data, or to be directly related with Tight-Binding (TB) parameters.

Within GA, we predict the modulation of the Fermi velocity in homogeneously strained graphene, being an important parameter present in most of the electronic properties. The modulation of Fermi velocity could be evidenced through expansion or contraction of the Landau Levels (LLs) spectra referenced to the pristine case. The last was explored with Density Functional Theory (DFT) calculations and TB approach to nearest neighbors, finding that LLs spectra is contracted (expanded) when graphene is stretched (shrunken) under the same magnetic field. In particular, we analyze the effect of uniaxial, shear, isotropic and mixed strain

on LLs energies, observing that a dominant isotropic expansion enhances the LLs contraction. These findings suggest that homogeneous deformations in graphene can be evaluated by measuring the changes in the LLs spectra, due to the linear behaviour of the effective Fermi velocity in the elastic regime for non pure shear strains. These results help to set the LLs spectroscopy in strained graphene, which could be used for the determination of relevant quantities as the anisotropic Fermi velocity, Hall resistance, Grüneisen parameters, Poisson ratio and related electronic properties.

Likewise from GA, we found that charge carriers inciding on the interface between two anisotropy Dirac materials obeys an unconventional Snell's law. We show that such law allows the develop of an electron quantum optics where collimators, total internal reflectors, valley beam splitters, negative refraction and valley filters can be obtained. A realization for graphene is possible by designing a system with two different homogeneously strained graphene sheets. These features would allow to build a series of novel devices inspired by well known optical devices, beyond of graphene.

Resumen

En años recientes, un fructífero tema de investigación en materia condensada que combina ideas de la teoría de la relatividad y electrodinámica cuántica ha surgido en una nueva clase de materiales denominados materiales de Dirac, los cuales constituyen una plataforma importante en el desarrollo de modelos efectivos inspirados en la teoría cuántica de campos. Estos materiales establecen un puente interesante entre materia condensada y física fundamental. La introducción de la anisotropía e inhomogeneidad en tales sistemas, lleva a una gran variedad de fenomenologías y aplicaciones hasta ahora inexploradas. Es por esto, que en esta tesis se estudia el efecto de la anisotropía e inhomogeneidad sobre la dinámica de los electrones en materiales de Dirac es usando un Enfoque Geométrico (EG), el cual provee una directa comprensión de las propiedades electrónicas derivadas desde un hamiltoniano efectivo el cual describe a los fermiones de Dirac sin masa. Debido a la anisotropía, algunos de estos materiales de Dirac muestran en su estructura electrónica de baja energía, un cono de Dirac distorsionado cuyos parámetros geométricos son incorporados desde un hamiltoniano de Dirac efectivo. Esta es una generalización del hamiltoniano de Dirac conocido en el grafeno prístino. Tal hamiltoniano tiene un conjunto de parámetros con un significado geométrico definido, introducido a través de una transformación canónica del momento lineal, y que pueden ser determinados desde la interpolación de las bandas de energía obtenidas con cálculos ab-initio, a partir de datos experimentales o relacionados directamente con los parámetros del método de enlace fuerte.

Con el EG, predecimos la modulación de la velocidad de Fermi en grafeno deformado homogéneamente, siendo un parámetro importante en la mayoría de las propiedades electrónicas, que podría ser evidenciado a través de la expansión o contracción del espectro de Niveles de Landau (NL), con respecto al caso prístino. Esto último, fue explorado usando el método de enlace fuerte a primeros vecinos, encontrando que el espectro de NL es contraído o expandido cuando el grafeno es deformado para el mismo campo magnético. En particular, analizamos el efecto de la deformación uniaxial, cortante, isotrópica y sus combinaciones sobre las energías de los NL, observando que con una dominante expansión isotrópica mejora la contracción de los NL. Estos hallazgos sugieren que las deformaciones homogéneas en el grafeno pueden ser evaluadas midiendo los cambios en el espectro de NL, debido al comportamiento lineal de la velocidad de Fermi efectiva en el régimen de elasticidad lineal para deformaciones no cortantes puras. Estos resultados ayudarían a desarrollar las espectroscopía de NL en grafeno deformado, la cual podría ser usada para la determinación de cantidades relevantes como la velocidad de Fermi efectiva, la resistencia Hall, los parámetros de Gruneisen, la razón de Poisson y propiedades electrónicas relacionadas.

Igualmente desde el EG, encontramos que los portadores de carga que inciden sobre la interfaz de dos materiales de Dirac anisotrópicos obedecen una ley de Snell no convencional. Mostramos que tal ley permite desarrollar una óptica cuántica de electrones obteniéndose colimadores, reflectores total internos, divisores de haces de valle-pseudospin, lentes convergentes y filtros de valle de pseudospin. Una realización de esta óptica es posible diseñando un sistema con dos diferentes láminas de grafeno tensionadas homogéneamente. Estas características permitirían construir una serie de nuevos dispositivos inspirados en dispositivos ópticos conocidos, más allá del grafeno.

Contents

Introduction

Graphene is the first two-dimensional material discovered with an one atom of thick, which is conformed by a honeycomb mesh of carbon atoms [1]. The simplest way to obtain graphene is exfoliating highly oriented pyrolytic graphite with the micromechanical cleavage technique, allowing to separate the graphite layers tighten with Van der Waals interactions [1]. The monolayer graphite called graphene has been studied intensively in the last ten years due to its exceptional and unique electronic properties. The band structure had been studied theoretically by Wallace since 1946, considering a Tight-Binding approach of graphite, where the monolayer presents a semimetallic phase in low energy [2]. One of the most outstanding phenomenologies discovered is the anomalous quantum Hall effect, evidencing that charge carriers are analog to massless Dirac fermions with a linear dispersion relation. Thus, the electrons and holes in graphene can be described by a Dirac-like hamiltonian, showing its pseudo-relativistic behavior at low-energy excitations [3]. Due to this feature, an intriguing issue in physics called Klein's paradox can be tested [4]. Klein paradox consists in that incident charge carriers with energies less than the electrostatic potential can cross a barrier without backscattering, which is classically forbidden. The Klein paradox was tested in high-energy physics experiments several decades ago without success [5, 6]. Not least surprising, other discovered properties in graphene are a high thermal conductivity of about 2-4 $\mathrm{kW\cdot m^{-1}K^{-1}}$ [7], transparency with transmittance of white light about of 97.7 % [8]. Also, graphene has the highest crack point under strain, being the strongest material known with a Young's modulus of 1 TPa and a tensile strength of 130 GPa [9], as well as a high Fermi velocity of $1 \times 10^6 \mathrm{ms}^{-1}$ approximately [3]. Further, it is an excellent conductor with mobility $\mu \approx 200,000\ \mathrm{cm^2V^{-1}s^{-1}}$ [10]. For these discoveries, A.K. Geim and K.S. Novoselov were awarded with the Nobel prize in 2010.

Many of the graphene's properties have been studied under anisotropic conditions, such as the application of a mechanical strain, with the aim of tailoring properties or to reach new phases from a topological phase transition [11, 13, 14, 15, 16]. Although, graphene is a very promising material for technological applications, its gapless semimetallic phase is an impediment for the realization of electronic devices. The hope for a gap opening in graphene was concentrated on the spin-orbit interaction, but the constant coupling of this interacion is practically negligible. Thus, several alternatives have been explored to generate a gap opening, one way is creating graphene nanostructures, known as nanoflakes [17, 18, 19]. Other options are the implementation of patterning that consists to induce atomic defects on graphene sheet [20], and the application of a mechanical strain [11]. The last represents a more clean way to control the graphene properties, which is not going in detriment of the main features of graphene. Thus, a new branch in the study of graphene was created, called the strain-engineering of graphene. However, the gap opening through strain-enginnering has been very discussed and until nowadays, there is not experimental evidence that confirms it in graphene.

A wide group of materials similar to graphene, whose low-energy carrier excitations behave as massless Dirac fermions, have been denomined as Dirac materials [12]. Frequently is reported the prediction of new Dirac materials [25], some have already been synthesized as MoS_2 by chemical vapor deposition [41] and phosphorene by mechanical exfoliation [42] and studied under applied strain [43, 44]. The great interest behind the study of two dimensional Dirac materials, apart of their exotic properties which represent a very important motivation, is manifold. One of the main reasons is due to the technological potential: to control the carrier density by the application of a gate voltage, to sinthesize Dirac materials with high mobility, to find a quantum Hall effect, to get a field effect transistor and to decrease the limit of miniturization of electronic devices are some of main goals about research on Dirac materials. The knowledge of this technological potential offered by the Dirac materials would lead to a new age in electronics with a probably substitution of the silicon. Others motivations arise from the possibility to design novel devices that exploit the pseudo-relativistic behavior of the charge carriers. For example, a condensed matters devices that mimic known effects in light optics-case, taking advantage of the analogy between photons and massless Dirac Fermions, but with the opportunity of using electromagnetic interactions, finding exotic effects. Likewise, Dirac materials offer the possibilty of explore new physics and testing of effective models developed in high-energy physics. Further, Dirac materials establish a bridge between condensed matters and high-energy physics, cosmology, statistical mechanics, chemistry and elasticity, that in most cases, provides a fruitful feedback on the fundamental physics. The discover of exotic effects as the topological magnetoelectric effect [21] was predicted from the modification of standard Maxwell's equations in three-dimensional topological insulators and it is one of the many examples of the phenomenological richness present in the arising of new Dirac materials. Nowadays, the study of Dirac materials has an enormous increment of works reported in the last years, mainly in graphene, with several reviews adressed to oriented specific aspects such as electronics properties [22], transport [23], strain-engineering [15], strong magnetic fields [24] and among others, consolidating in one of the most studied contemporary hot topics in physics. The knowlegment of new Dirac materials as dichalcogenides [25], topological insulators [21], organic Dirac materials [26], silicene [27], germanene [28, 29], Weyl semimetals [30], *d*-wave superconductors [12], phosphorene [31], molecular graphene[32], artificial graphene[16, 33], graphyne, graphdiyne, graphone, and graphane [34] have had a significantly evolution after the discovery of graphene.

From the theoretical point of view, different authors have established effective models to describe the charge carrier dynamics in Dirac materials taking into account the strain. Strain produces remarkable effects on the electronic band structure, mainly in low-energy excitations, such as the displacement of the Dirac points with respect to the high-symmetry points in the first Brillouin zone, the change of the transversal cross section and the tilting of the Dirac cone with respect to the vertical symmetry axis. The proposed effective models can be classified in two groups: the first corresponds to models considering the expression of a hamiltonian with respect to the high symmetry points in the first Brillouin zone. In the second group, the hamiltonian is expanded around the new Dirac points where the current configuration is the corresponding to the strained system. The first group develops an effective Dirac-like hamiltonian that takes on account the Dirac material's symmetries. The analogy of these models with related ideas of quantum electrodynamics and general relativity has brought to the designation of *Quantum Field Theory in Curved Spaces* (QFTCS) [15]. The second group establishes an effective hamiltonian around the Dirac point, whose dispersion relation captures the main features of the band structure near to the Fermi level. Both point of views are useful in the understanding of the behavior of the charge carriers of the Dirac materials under strain. Some terms that are contained in both effective hamiltonians correspond to the same physical interpretation, but with different values in the coupling constants. For example, for the case under homogeneous strain, QFTSC contents two physical quantities completely absent in the models of the second group. Those quantities are associated to scalar and vector potentials that for the case of inhomogeneous strain can induce pseudo-magnetic fields. For homogeneous strain due to the spatial independence, the generatation of pseudo-electromagnetic fields is absent, but the pseudo-scalar and vector potential are strain dependents. Thus, many authors prefer to study theoretically the effects of strain using the pseudo-vector and scalar potentials, neglecting the Dirac cone anisotropy. Pseudomagnetic fields generated by strain are an interesting phenomenology, due to the possibility of design electromagnetic devices working without the use of electromagnetic fields. The presence of pseudo-magnetic fields was confirmed experimentally in graphene nanobubbles as well as in molecular and artificial graphene [32, 35, 36], with values of pseudo-magnetic fields of 1000 T, which is a value higher than the conventional magnetic fields obtained in the laboratory. Some authors consider that both approaches are equivalent due to the similarities in the physical description of some phenomenologies [11, 37, 38, 39] but with quantitative differences. However, the most popular and used theory corresponds to the first group above mentioned, which predicts some phenomenologies on strained graphene still not yet experimentally confirmed.

The contribution of the present thesis corresponds to the second group aforementioned, generalizing the existing models in the literature, and extending the strain-engineering ideas to a more general concept: anisotropic Dirac cones. That anisotropy can have different origins such as chemical manipulation, rearranged configuration of the system or stress in the material producing changes on the electronic band structure [11, 33, 36, 40]. Thus, the anisotropy can be introduced in the effective Dirac-like hamiltonian either through Fermi velocity tensor, canonical transformation on the linear momentum, or from a renormalized linear momentum and spin rotation. The three ways of introducing anisotropy in the hamiltonian are equivalent. We show that all the information of the anisotropy is stored in a matrix whose parameters, describing an especific material, can be obtained from Tight-Binding (TB) calculations, *ab-initio* calculations using Density Functional Theory (DFT) or experimental data. The anisotropy matrix elements are related with geometrical parameters of the Dirac cone. For this reason, the proposed model is called Geometrical Approach, which provides a direct way to link and tailor electronic, optical, and transport properties with the anisotropy of the Dirac cone through the renormalization of the Fermi velocity. In this thesis, homogeneously strained graphene is the case study system chosen for the implementation of two applications of the Geometrical Approach:

i) Landau Levels Spectroscopy: In a material, the charge carriers moving in a magnetic field have a quantized energy spectrum known as Landau levels (LLs). Using the Geometrical Approach, it was found that this spectrum can be modulated by changing the effective Fermi velocity, resulting from the variation of the Dirac cone geometrical parameters. It was predicted that applying homogeneous strain can be produced an expansion or contraction of the density of states (DOS) respect to the equilibrium spectra. Thus, the value of the effective Fermi velocity can be extracted, as well as other related properties such as Hall resistance and conductivity. We have shown that the expansion or contraction of the LLs spectra can be used as test in the measurement of the effective Fermi velocity, due to the discrepancies in the prediction of the effective Fermi velocity by the proposed effective models in graphene. That result is relevant to the development of LLs spectroscopy in Dirac materials.

ii) Electron Quantum Optics: due to the analogy between photons and massless Dirac fermions, we found that in a $p-n$ junction between two anisotropic Dirac materials, the incident charge carriers are refracted in the interface following a unconventional Snell's and reflection law, which was derived using the Geometrical Approach. Since the two Dirac materials in a $p-n$ junction show different anisotropies, the refraction of the Dirac fermions is valley-dependent. These features allow to propose a series of electron-optics devices based on Dirac materials, for instance, such as: reflectors, collimators, valley-filters, Veselago and super divergent lenses, and valley-beam splitters.

The two mentioned physical systems were explored in homogeneously strained graphene using a TB description in the most of cases and DFT in specific cases. These systems represent a narrow window of the great scope of the Geometrical Approach, because many systems presenting Dirac cones can be explored as well as other phenomenologies.

Chapter 1

Overview on strain engineering and effective models for graphene and related systems

Graphene presents exceptional electronic, elastic and transport properties, becoming a material very promising for technological applications. Nevertheless, graphene's gapless semiconductor nature is an impedement for the development of electronic nanodevices. This problem has led to explore several alternatives: on the one hand, a tentative solution is the proposal of two-dimensional materials with similar properties that graphene. Nowadays, a great list of materials had been considered as candidates, such as the recently synthesized dichalcogenides or phosphorene [41, 42], having a Spin-Orbit Interaction (SOI) higher than graphene as a gap generator. On the other hand, nanoflakes and nanoribbons of graphene [17, 18] presents a band gap energy, but the edge roughness detriments their electronic properties. Therefore, other ways have been referred and one route to create a robust gap in graphene, without damage of their main features, is offered by strain engineering of graphene [11, 40, 45, 46]. This topic provides the possibility of the obtention of a gap opening through the induction of a Topological Phase Transition (TPT) from a semi-metallic phase with two Dirac cones to a band insulator. Further, the strain engineering opens a wide range of possibilities to modulate the electronic, optical and transport properties, allowing the design of novel devices operating with high pseudomagnetic fields [35, 47]. One important motivation has been the development of novel experimental techniques for the application of in-plane strains on graphene [48, 49], waking the interest about the confirmation of the predictions in several proposed models. Other striking related topic is the combination of doping and strain effects, allowing the exploration of new topological phases [50]. Recently, the possible transition to a superconductor state in graphene through the combination of strain and doping was inquired [51].

In this chapter is presented the development of the main ideas that had arised about this topic: the effect of strain on electronic properties of graphene and related materials, showing how these effects were embodied in several effective models. Thus, the dynamics of Dirac fermions for low energy regime can be described from an effective hamiltonian, which is constructed with the required symmetries of the system. Likewise, different perspectives of these effective models are exposed, as well as their predictions and experimental confirmations.

1.1 Brief description of Graphene

Graphene is the first two-dimensional material and it is conformed by a hexagonal lattice of carbon atoms with sp^2 hybridization, where $2p_z$ orbital is perpendicular to the plane. The hexagonal lattice can be seen as built through benzene rings whose hydrogen atoms are substituted by carbon atoms. The possibility about its synthetization was initially questioned, because a suspended two-dimensional crystal must be mechanical unstable. However, the stability of graphene is warrantied due to the mechanical similarity with soft membranes [52]. Its synthesizing was performed through micromechanical cleavage technique since 2004 by A.K. Geim and K.S. Novoselov [1]. They were awarded with the Nobel prize in 2010 due to the great technological potential that possess graphene further clarify intricated concepts of fundamental physics. The theoretical study of graphene's electronic properties proceeded several decades ago [2], since the graphene sheet was considered as the basic constituent of carbon allotropes among them the graphite, the carbon nanotubes, and the fullerenes.

The graphene physical properties can be well described using the Tight-Binding (TB) approach to nearest neighbors with energies to the Fermi level [24]. The hexagonal lattice is separated by two triangular sublattices, where the unit cell contents two carbon atoms. The lattice vectors are denoted as $\vec{a}_1^0$ and $\vec{a}_2^0$ as shown in Fig. 1.1 (a), together the position $\vec{\delta}_j^0$ with

$j = 1, 2$ and 3 for the three nearest neighbors, where the superscript 0 indicates the values corresponding to pristine graphene. With a Cartesian system whose x-axis is chosen along the Zig-Zag (ZZ) direction, the nearest atom positions are written as $\vec{\delta}_1^0 = a(\frac{\sqrt{3}}{2}, -\frac{1}{2})$, $\vec{\delta}_2^0 = a(0, 1)$ and $\vec{\delta}_3^0 = a(\frac{-\sqrt{3}}{2}, -\frac{1}{2})$, being $a = 1.42$ Å the C-C equilibrium distance. Likewise, the vectors of the reciprocal lattice are given by $\vec{b}_1^0 = (2\pi/A_c^0)\vec{a}_2^0 \times \hat{z}$ and $\vec{b}_2^0 = (2\pi/A_c^0)\hat{z} \times \vec{a}_1^0$, so the first Brillouin zone is a hexagon with high symmetry points K and K'.

The TB approach to nearest neighbors reproduces the ground electronic band structure only considering the p_z orbital, which is decoupled with σ orbital. The overalp terms in the TB calculation are neglected because the p_z wavefunction decays quickly and it is expected to be vanish for distances bigger than 1Å. Thus, the unique parameter in the TB calculation is the hopping parameter t, having an estimated value of 2.71 eV [22]. Therefore, when the TB hamiltonian is diagonalized, the dispersion relation has the shape shown in Fig. 1.1 (b). One of the most striking aspects of this dispersion relation is the appareance of energy surfaces with cone shape. The conduction and valence bands are touched at called Dirac points, which coincides with the high symmetry points K and K' of the first Brillouin zone. Such aspect was corroborated using angle resolved photoemission spectroscopy (ARPES) [53], which was the first experimental evidence of the electronic band structure of graphene. The presence of Dirac cones around the high symmetry points of the first Brillouin zone can be appreciated in Fig. 1.1 (c). This special feature of the energy bands are obtained from the diagonalization of the TB hamiltonian, expanding it around the Dirac point to first order in the wave vector $\vec{q}$, leading to

$$H = \frac{3ta}{2} \begin{pmatrix} 0 & q_x - iq_y \\ q_x + iq_y & 0 \end{pmatrix}, \tag{1.1}$$

describing the dynamic of the electrons for low-energy excitations ($E << t$), where the dispersion relation is $\epsilon_q = s\frac{3at}{2}|\vec{q}|$, with $s = \mathrm{sgn}(E)$. Equation (1.1) is similar to a Dirac-like hamiltonian within continuum limit [22, 24]

$$H = v_F \vec{\sigma} \cdot \vec{p}, \tag{1.2}$$

where $\vec{p} = \hbar\vec{q}$ is the linear momentum, $v_F = 3ta/2\hbar$ is the Fermi velocity playing the role of the light velocity c, whose ratio is roughly estimated to be $c/v_F \approx 300$ [22]. The Pauli

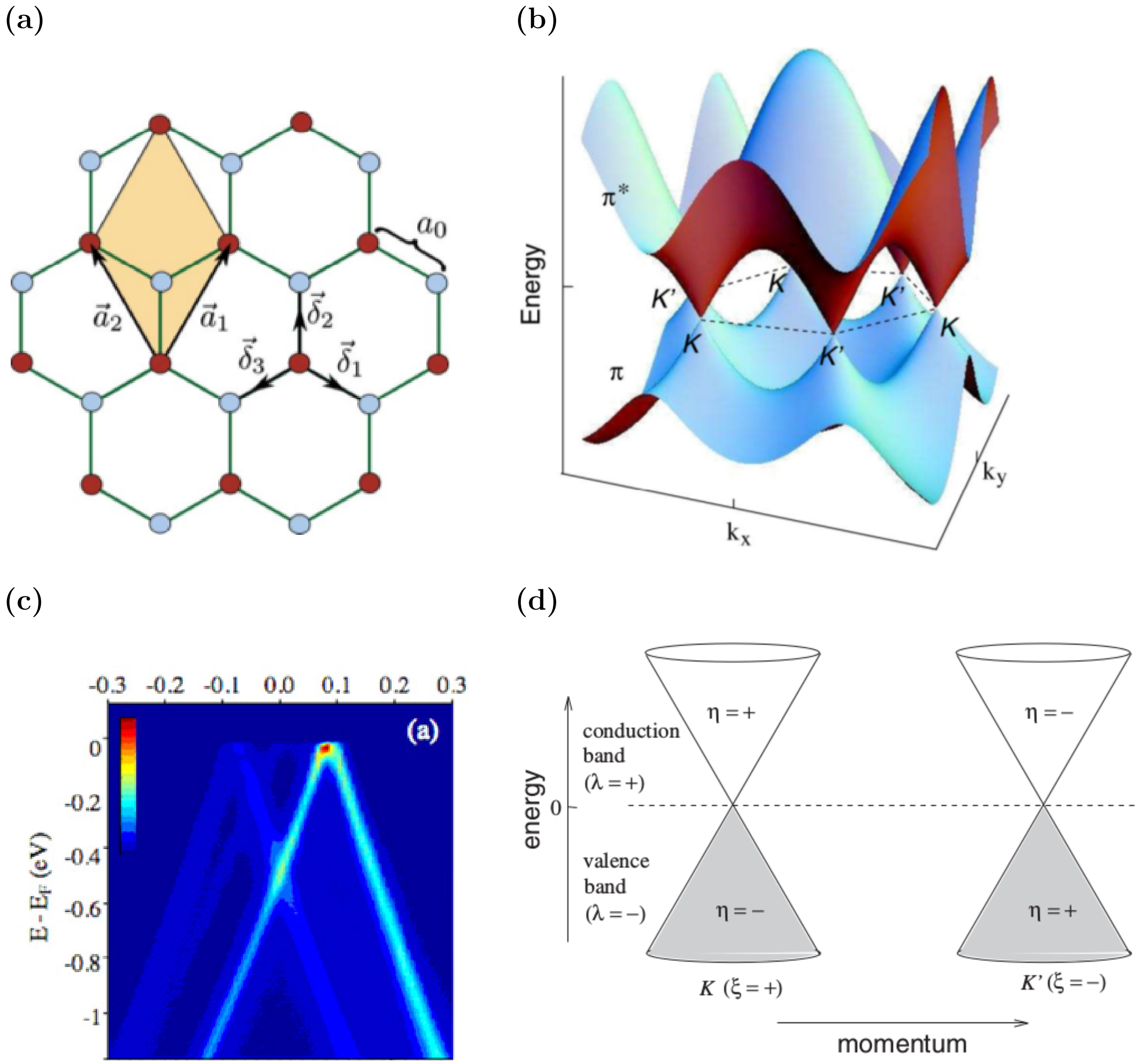

Figure 1.1: Scheme of a honeycomb lattice of pristine graphene and its electronic band structure around the Dirac points. (a) Hexagonal lattice is separated by two triangular sublattices A and B where its lattice vectors $\vec{a}_1^0$ and $\vec{a}_2^0$ and the neighboring sites $\vec{\delta}_1^0$, $\vec{\delta}_2^0$ and $\vec{\delta}_3^0$ are shown. The red and blue circles denote the carbon atom positions for the A and B triangular sublattices, respectively. (b) Plot of the dispersion relation obtained from TB method in graphene. (c) The first observation of the electronic band structure around the Dirac points using ARPES. (d) Illustration of the concepts of pseudospin sublattice and pseudospin valley. These figures were taken from refs. [11, 24, 53].

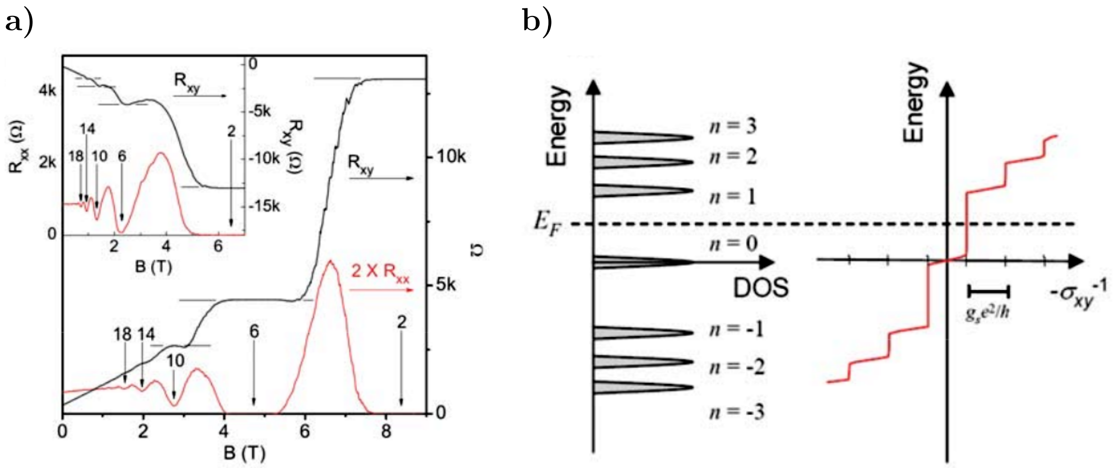

Figure 1.2: Experimental evidence of an anomalous quantum Hall effect in graphene. (a) Measurements of the magnetoresistance (red) and Hall resistance (black) showing the apparition of an anomalous quantum Hall effect. (b) DOS presents a serie of peaks due to the Landau level quantization of the massless Dirac fermions in presence of a uniform magnetic field, causing plateaus on the Hall conductivity. These figures were taken from ref. [54].

matrices denoted by $\vec{\sigma}$ discriminates the contribution of the two triangular sublattices, different of the true physical spin of the particle in relativistic scenary. One identical hamiltonian (1.2) is obtained at other unequivalent Dirac point K' due to the time reversal symmetry. Hence, a 4×4 diagonal block representation of the Dirac-like hamiltonian of the form $H_D = v_F \tau_z \otimes \vec{\sigma} \cdot \vec{p}$ is reached, being τ_z the z-component of the Pauli matrix acting on a pseudospin valley space [24]. Thus, the two first (last) components of the four-spinor $\Psi_q = (\psi^A_{q,+}, \psi^B_{q,+}, \psi^B_{q,-}, \psi^A_{q,-})$ represent the lattice components of a massless Dirac fermions from the pseudospin valley K^+ (K^-) which coincides with the high symmetry point K (K') in pristine graphene. Usually in high-energy physics, the helicity operator is defined as $\hat{h} = \vec{\sigma} \cdot \vec{p}/|\vec{p}|$, and for massless Dirac fermions it commutes with the Dirac hamiltonian, being a good quantum number. The helicity eigenvalues are $\eta = +1$ or $\eta = -1$ indicating that the spin is parallel or antiparallel along of the movement direction, respectively. A relation among s, η and pseudospin valley ξ is given by $s = \eta\xi$ showing that electrons from different valleys have opposite chiralities, further electrons and holes always have different quiralities for the same valley, one pictorial representation about this is shown in Fig. 1.1 (d).

The resemblance between electrons in graphene and relativistic particles were revealed from experimental realization of an anomalous quantum Hall effect [3, 54]. Measurements of magnetorresintance R_{xx} and Hall resistance R_{xy} showed some common features to the integer quantum Hall effect (IQHE): the apparition of Shubnikov-de Haas oscillations on R_{xx} as a function of the magnetic field B, and the presence of plateaus over R_{xy} and conductivity σ_{xy}, due to the Landau levels quantization, as seen in Fig. 1.2 (a). However, the Hall conductivity in graphene $\sigma_{xy} = (4e^2/h)(N + 1/2)$ becomes different to the conventional $\sigma_{xy} = (4e^2/h)N$, where e is the charge of electron, h the Planck's constant, and N is an integer. Therefore, a unusual behavior of the QHE can be observed, since the transition from lowest hole to the lowest electron is not interrupted passing through zero, as shown in Fig. 1.2 (b). Thus, a half-integer quantum Hall effect was observed whose explaination can be formulated from the Landau levels (LLs) spectrum of ultrarelativistic particles [3, 54].

$$E_n = \mathrm{sgn}(n)\frac{\hbar v_F}{l_B}\sqrt{2(|n| + 1/2 \pm 1/2)}, \tag{1.3}$$

where l_B is the magnetic length, $\mathrm{sgn}(n) = +1$ (-1) indicates the Landau level energy for electrons (holes), and $\pm 1/2$ corresponds to a LLs spectrum for massless Dirac fermions with pseudospin $+1/2$ and $-1/2$. From equation (1.3), we noted that levels with $|n| \geq 1$ present a double degeneracy. This is because all levels are occupied by Dirac fermions with parallel and antiparallel pseudospins to exception of the zero-level with only a pseudospin projection. In consequence, the zero-level is shared equally by electrons and holes, as shown in Fig. 1.2 (b).

The concept of pseudospin sublattice and the analogy between electrons and massless Dirac fermions, were the essential elements for the proposition of graphene as the first experimental realization of the Klein tunneling (KT) [55]. Since 1929, O. Klein predicted that a relativistic particle with kinetic energy lesser than the potential barrier height can cross it without retro-dispersion independently of its wide [5]. The experimental evidence of the KT using the elementary particles through nuclear processes or from astro-physics have been so far impossible. The phenomenon was called as Klein's paradox due to its counterintuitive nature. A conceptual scheme of the nowadays called KT in graphene is shown in Fig. 1.3 (a), where incident electrons are shown crossing a potential barrier whose height exceeds the electron energy. The potential barrier can be created using local chemical doping with the aim of generate holes,

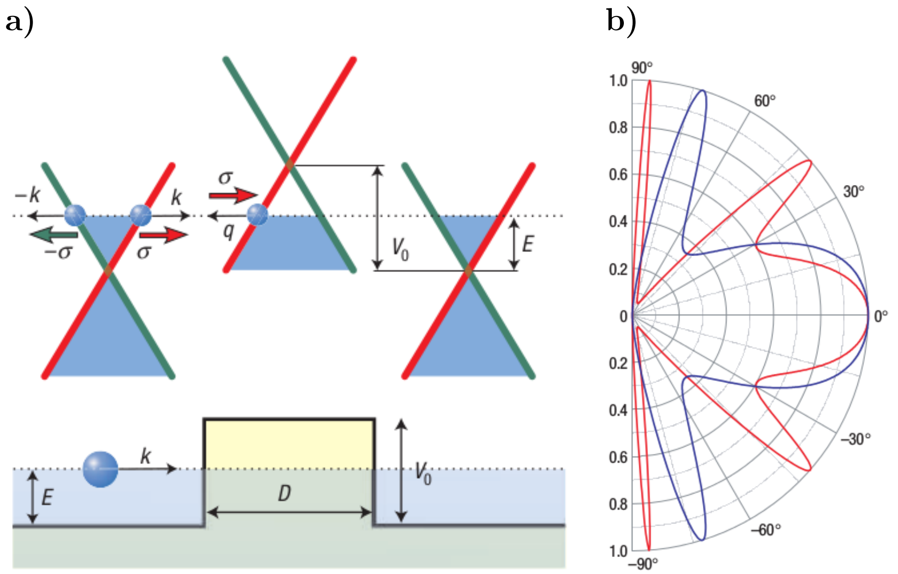

Figure 1.3: Scheme of the Klein tunneling in graphene. (a) Kinematical construction and physical system that illustrate how the potential barrier becomes transparent for Dirac fermions with normal incidence and an energy lesser than barrier height. (b) Transmission probability as a function of incidence angle for electrons of graphene incidenting with energy $E = 80$ meV on a potencial barrier of wide $D = 100$ nm and heights $V_0 = 200$ (blue) and $V_0 = 285$ meV (red). These figures were taken from ref. [4].

producing an energy displacement of the linear dispersion relation. Thus, the electrons pass to the same valley branch due to the conservation of pseudospin, since electrons and holes have their pseudospins aligned along the movement direction when a normal incidence is considered. Hence, when KT occurs the potential barrier is transpararent. The transmission probability was derived for different incidence angles in [4]. This can be obtained solving the Dirac equation inside and outside of the barrier, and applying the continuity conditions on the wavefunctions in the borders, obtaining

$$T(\phi) = \frac{\cos^2\phi\cos^2\phi_R}{\cos^2\phi\cos^2\phi_R\cos^2(q_xD) + (1 - ss'\sin\phi\sin\phi_R)^2\sin^2(q_xD)}, \tag{1.4}$$

where ϕ and ϕ_R are the incident and refraction angle, respectively. The signs s and s' are defined as $s = \text{sgn}(E)$ and $s' = \text{sgn}(E - V)$, q_x is the linear momentum along x and D is the barrier wide. Equation (1.4) presents resonances when $q_xD = n\pi$ doing that $T(\phi) = 1$. For normal incidence $\phi = 0$, the potential barrier is completely transparent independently of the wide D,

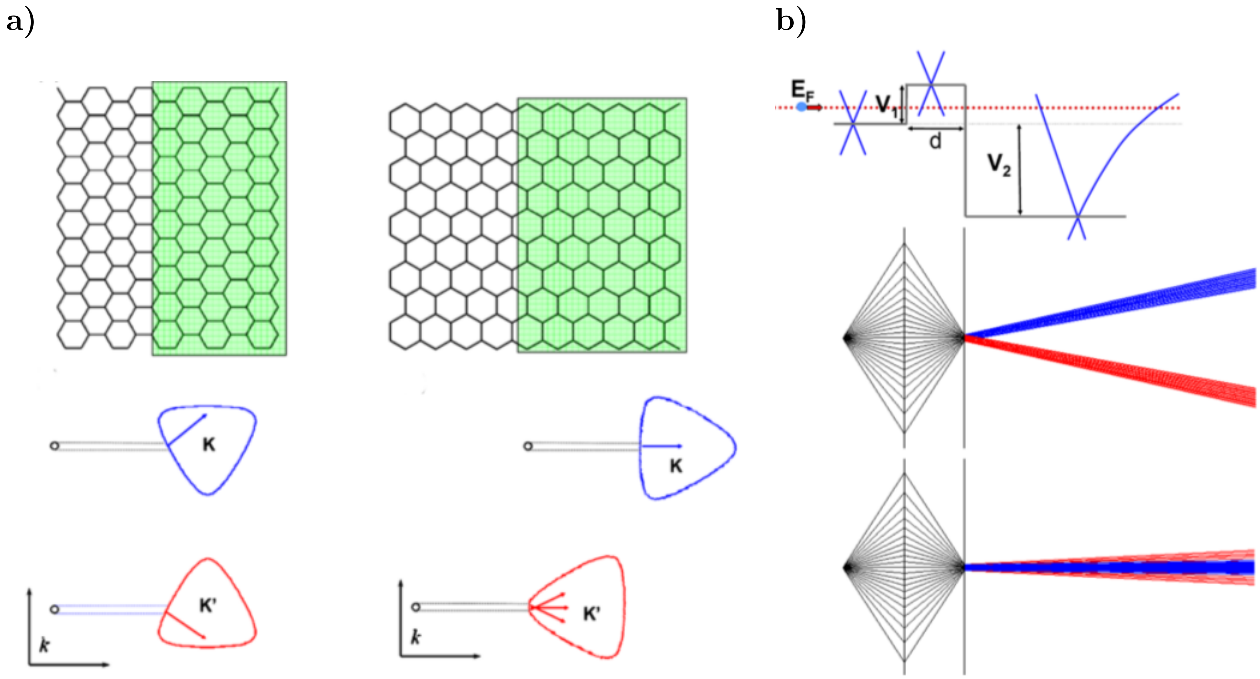

Figure 1.4: Pictorial representation of the collimation and valley beam splitter in graphene. (a) Top: valley beam splitter and collimation are obtained using a graphene $p-n$ junction with interface along ZZ and AC direction, respectively. The green area denotes the region doped with holes at energies where the trigonal warping becomes relevant. Bottom: a kinematical construction shows how the refraction of Dirac fermions is valley-dependent using an interface along ZZ direction, caused by the trigonal warping distortion. An interface along AC direction changes the orientation of the trigonal warping, producing an effect of collimation at K valley together with a little dispersion at other valle. (b) Top: Potential profile of a $n-p-n^-$ junction and kinematic scheme of electrons transmission. Bottom: a focal source located at n-region emits electrons towards the p-region, which acts as a lens that directs the beams to the convergence point. In the n^- region, the trigonal warping produces the valley beam splitting or the collimation above mentioned. These figures were taken from ref. [56].

which is manifestation of the KT. An illustration of the transmission probability as a function of incidence angle is shown in Fig. 1.3 (b).

It was also demonstrated that systems conformed by $p-n$ junction in graphene acts as a convergent lens of massless Dirac fermions, in a similar way to the refraction of light in metamaterials [57]. Such mechanism could be used to separate and collimate valley polarized currents when graphene is doped beyond its linear energy regime. The trigonal warping distortion and the relative orientations of the p and n regions are the responsible of a valley splitting, which could have a relevant importance in the generation valley polarized currents in electronic devices. This valley degree of freedom could be used as carry information [56]. In Figs. 1.4 (a) and (b) were illustrated the orientation of the p and n regions and their respective kinematical construction, showing how the collimation and valley beam splitter can be obtained using trigonal warping distortion. The main disadventage of this proposal is that the use of energy values beyond linear region could present many practical problems.

1.2 Gap opening and Fermi velocity modulation in shear and uniaxially strained graphene

Strain does not only modify the bond lengths, also affect the electronic band structure, allowing to serve as modulator of the electronic properties. It is known from *ab-initio* calculations, that it is not neccesary to count with a constitutive equation for study the effects caused by strain. Therefore, an instructive and complementary exercise result of the comparison between numerical and analytical calculations that involve strain. The example is shown for strained graphene, where the analytical route can be done using TB method and elasticity theory.

In order to observe how the strain in graphene changes the energy landscape and induce a Topological Phase Transition (TPT) from a semimetallic to an insulator phase, it is necessary to determine through elasticity theory, the bond lengths and the new position of the carbon atoms on the current configuration. Thus, for uniaxial or shear strain in graphene, the bond lengths was obtained, expanding to first order the strain tensor components [11]

$$\frac{\delta_1}{a} = 1 + \frac{3}{4}u_{xx} - \frac{\sqrt{3}}{2}u_{xy} + \frac{1}{4}u_{yy} \tag{1.5}$$

$$\frac{\delta_2}{a} = 1 + u_{yy} \tag{1.6}$$

$$\frac{\delta_3}{a} = 1 + \frac{3}{4}u_{xx} + \frac{\sqrt{3}}{2}u_{xy} + \frac{1}{4}u_{yy}, \tag{1.7}$$

the modification of the position of carbon atoms lead also to a reciprocal lattice distortion and

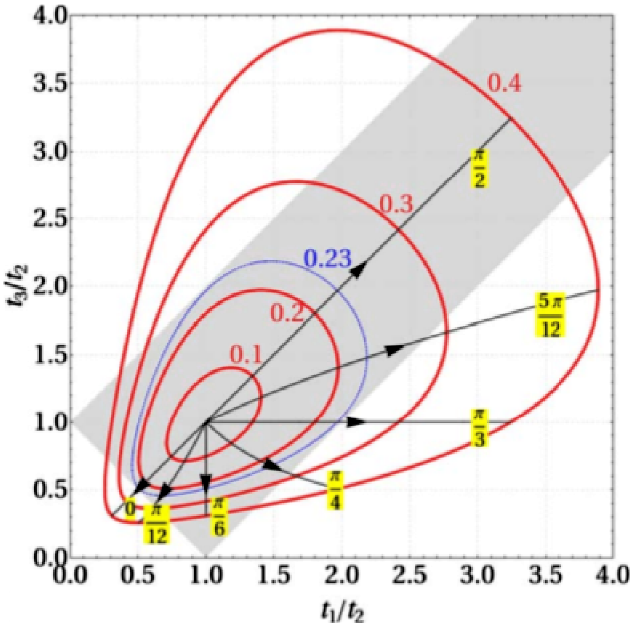

Figure 1.5: Topological phase transition described from the nearest hopping parameters with a TB approach for uniaxially strained graphene. Gray and white area represent the semimetallic and insulator phase, respectively. The black (red) curves show the hopping factors as a function only of the tensile strain (tension angle). The blue isostrain curve has the minimal critical tensile strain $\epsilon = 0.23$ where the TPT is reached for the tension angles $\theta = 0, \frac{\pi}{3}, \frac{2\pi}{3}$. This figure was taken from ref. [11].

a shift of the high symmetry points.

The hopping parameters of a TB approach to nearest neighbors are frequently related with the bond lengths through an exponential decay rule [11]. Then, it is possible to find the strain values where the TPT is reached. About this, Pereira et. al. [11] demonstrated how a gap opening can be induced through uniaxial strain, which is illustrated in Fig. 1.5. In this plot, the shadded rectangular area is the semi-metallic phase, where all points satisfy the triangular inequallity $|t_i - t_j| \leq t_l \leq t_i + t_j$ with $i \neq j \neq l$ between hopping factors [14, 58]. Outside this region, the strain converts to graphene in an insulator with a gap which can be robust when the tensile strain is increased. The red and black curves are parametrized trajectories of the tensile strain ϵ and tension angle θ of the hopping parameters. Iso-strain (red) curves are function of the angle θ, while the iso-angular (black) curves are function of the tensile strain ϵ. Along Arm-

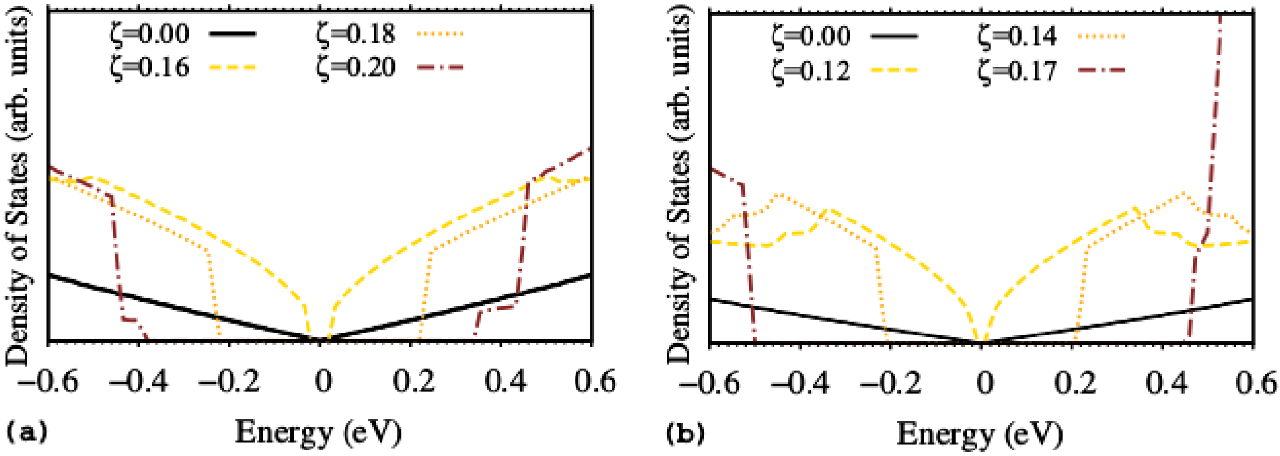

Figure 1.6: DOS as a function of shear strain ζ. (a) The gap opening is obtained at $\zeta = 0.16$ using shear strain. (b) The combination of uniaxial and shear strain induces a band gap for a strain value $\zeta = 0.12$. These figures were taken from ref. [45].

Chair (AC) direction, a gap opening can not be generated since the trajectory is always within the shadded area. In contrast, along ZZ direction a more appropiated trajectory to induce a gap is obtained, leaving the shadded area for a critical tensile strain value of 23 % approximately. Although, uniaxial strain guarantees the induction of a gap in graphene, the excessive value of the tensile strain around 23 % is very near to the breaking point [9] and an experimental observation could not be possible. However in other work, a critical tensile strain of 16 % was predicted for shear strained graphene from a TB approach, having a lower gap threshold for shear strain than uniaxial strain [59]. Theoretical DOS around the Fermi level as a function of shear strain parameter, evidenced a gap opening. With the combination of uniaxial and shear strain, the critical strain value can be less to 12 %, as shown in Fig. 1.6. Those works indicate that the use of other strain types could obtain a gap threshold with smaller critical values. This was already explored by Naumov and Bratkovsky through a periodic inhomogeneous strain from *ab-initio* methods [46].

In other works, DFT calculations have also been performed at cases of uniaxial and homogeneous strain [45, 46, 60, 61, 62, 63, 64, 65, 66, 67]. There are several aspects where DFT method and TB approach match, the most prominent is the moving of the Dirac cones toward a merging. Indeed, the most effective way to merge the Dirac points is straining along ZZ direction. Likewise, the shifting of Dirac points with respect to high symmetry points was observed, but the prediction of a gap opening has been highly disputed. The anhilation of Dirac points at merging does not lead inmediately to a gap opening, due to that the σ^* band is pushed down toward the Fermi level. This prevent the total opening of a gap. The last, was observed taking into account the relaxation of the atomic positions [46, 66, 67]. Recently, Kerszberg and Suryanarayana [62] studied homogeneous strains in graphene and found that with a stretching of 11 % along ZZ direction, and shrinking -20 % along AC direction, a gap of 1 eV can be opened. Their calculations were done without relaxation of the atomic positions. Thus, the relaxation of the atomic positions seems to be a key point in the understanding of the strain engineering graphene's bandgap.

Other treated aspect of the graphene's strain engineering is the modulation of the electronic, optical and transport properties. The study of the modulation of the graphene's properties through the strain is mainly focused in the anisotropy of the Fermi velocity. To understand the anisotropic behavior of Fermi velocity is essential in the study of strained graphene, because it is involved in the most of the physical observables. Thus, tuning the Fermi velocity also affects to the observable depend on it. TB and DFT calculations [66, 67, 68] show that the Fermi velocity decreases under uniaxial strain with an evident anisotropy along ZZ and AC directions. The tuning on the Fermi velocity has influence on the increment of work function [66], the optical conductivity [37, 69] and LLs spectra [67, 68], for citing some examples. Two recently experimental reports had evidenced the inhomogeneity and anisotropy of the Fermi velocity. The first was performed for graphene grown on a Rh foil [70], where the spatial variation of the Fermi velocity is due to the ripples caused by the induced strain. In the second work, graphene was grown on BN [71] obtaining that the strain varied with the height of the ripple. Then, the Fermi velocity can be estimated through the measurements of the DOS. On the other hand, the Fermi velocity also is modified with the doping, where the electron-electron exchange interactions produce a Fermi velocity renormalization as well as a distortion of the Dirac cone [50, 72, 73, 74]. Experimental works reported variations of the Fermi velocity as a function of the electron density, observing that it is increased when electron density decreases [73, 74]. Rostami and Azgarid theoretically studied how the Fermi velocity changes with the use of uniaxial strain and doping, noting that the charge compressibility is tuned through the Fermi velocity modulation [72], in agreement with previous experimental results [75].

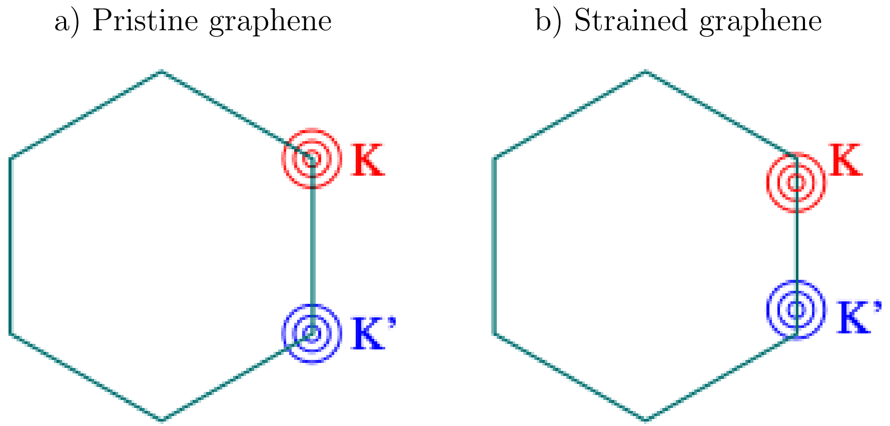

Figure 1.7: Geometrical illustration of the Dirac and high symmetry points in the first Brillouin zone. (a) For pristine graphene these points coincide while in (b) for strained graphene, the points do not coincide anymore. This figure was taken from ref. [22].

In summary, the three main effects caused by strain are exhibited as follow due to their importance in the development of several known effective models [15, 24, 37, 38]:

(i) *The shifting of the Dirac points.* In pristine graphene, the Dirac points match with the high symmetry points of the first Brillouin zone. For strained graphene, these points are shifted with respect to high symmetry points of the deformed first Brillouin zone. From TB approach to nearest neighbors of uniaxially strained graphene, and assuming that the lattice remains undeformed, the Dirac points position were calculated exactly along ZZ and AC directions [11]

$$\vec{K}_D = \left(\pm\frac{2}{\sqrt{3}}\arccos\left[-\frac{t_2}{2t_1}\right], 0\right), \tag{1.8}$$

where t_1 and t_2 are related with the strain tensor components through the Papaconstantopoulus' rule [76]. New high symmetry points were given directly in terms of uniaxial strain parameters

$$\vec{K} = \frac{4\pi}{3\sqrt{3}}\left(1 - \frac{1}{2}\epsilon(1-\nu), -\epsilon(1+\nu)\sin[2\theta]\right), \tag{1.9}$$

where ν is the Poisson's ration, ϵ is the tensile strain and θ indicates the strain direction. The Fig. 1.7 shows the shifting of the Dirac points with respect to the high symmetry points of the deformed first Brillouin zone.

(ii) *Deformed cross section of the Dirac cone.* It was probed from TB and DFT calculations that the transversal cross section of the Dirac cone is elliptical within low energy regime ($E < 1$

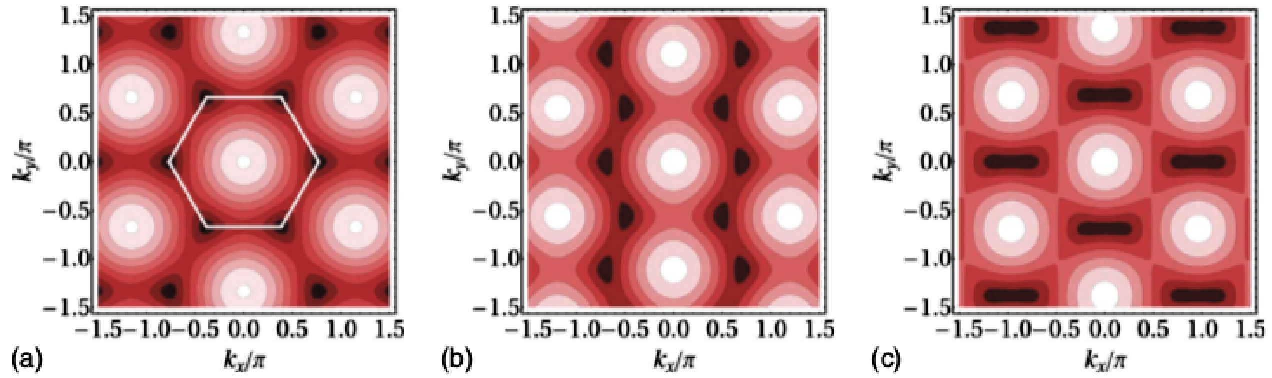

Figure 1.8: Energy contours for (a) pristine graphene, (b) uniaxially strained graphene along AC direction with a value of tensile strain $\epsilon = 0.2$, and (c) along ZZ direction with $\epsilon = 0.2$. Figure took from ref. [11].

eV) for homogeneous strain with a shear strain contribution different to zero [11, 38, 66, 67]. Beyond low energy regime, it is necessary to include trigonal warping effects for the study of intriguing phenomenologies [24, 37]. The distortion of the Dirac cone has important consequences in the electronic ground-state properties, such as LLs expansion/contraction, Fermi velocity modulation [24, 68, 67], optical conductivity [37, 77], and anisotropic conductivity of strained graphene [78]. The deformed cross section of the Dirac cone has been studied from effective models with an expanded TB hamiltonian around Dirac point [24, 37, 38, 67]. In Fig. 1.8 is illustrated how the transversal section changes as a function of uniaxial strain [11].

(iii) *Electron-hole asymmetry: overlap and tilted Dirac cones.* In an earlier report about pristine graphene [79], it was observed an asymmetry between the valence and conduction for π band around the Dirac points, known as electron-hole asymmetry. This asymmetry was described with the inclusion of overlap parameters in the TB approach to nearest neighbors. These parameters are smaller than the hopping parameters. In strained graphene, the electron-hole asymmetry arises by the overlapping of the p_z wavefunctions and when the next nearest neighbors hoppings in the TB calculations are taken into account. In most of the cases, the overlap parameters are neglected due to their small value. Expanding the TB hamiltonian around Dirac point, the next nearest neighbors hopping parameters are responsible for the tilting of the Dirac cones [68], which can have a main contribution for uniaxial strain beyond 15 % along ZZ direction [67]. Other Dirac-like systems, as the organic salt α-(BEDT-TTF)$_2$I$_3$

for instance, presents a tilting of the Dirac cones greater than graphene [68]. Thus, the effect of tilt on electronic properties as magnetophonon resonance can be evidenced [80, 81].

1.3 Effective models for strained graphene

The effects mentioned in the above section have been embodied in several effective models describing the dynamics of Dirac fermions in strained graphene. The most known is the Quantum Field theory in Curved Spaces (QFTCS) model. Within this theory, a hamiltonian was constructed taking inot account the symmetries of the system, namely using group theory for high symmetry points. Each term of the hamiltonian represents some of the effects caused by strain [15]. One interesting result of the QFTCS was the connection of the strain tensor components with pseudo scalar and vector potentials, as a pseudo-electromagnetic field. The QFTCS is successful because many predictions have been experimental confirmed such as pseudo-LLs in graphene like-systems such as molecular graphene [32] and hexagonal optical lattices [36]. This has led to the proposition of electromagnetic devices operating without electromagnetic fields, since the inhomogeneous strain produces pseudomagnetic fields. For instance, a quantum Hall effect without magnetic field could be observed.

On the other hand, effective models have been developed taking into account an effective Weyl-like hamiltonian around Dirac point. From this point of view, the description of the effects caused by homogeneous strain can be performed without the use of pseudo scalar and vector potentials. All the information of strain is mainly captured from the distortion of the Dirac cone, which has been neglected in most of the works using QFTCS. Each author from this perspective have studied different aspects of the electronic band structure with its particular assumptions. A third proposal consists in the study of the electron dynamics through the development of an effective hamiltonian, which is expanded around the invariant time reversal M point of the first Brillouin zone. Further, this consideration has the advantage of describe a possible TPT from the semimetallic phase which involves two Dirac cones, to insulator phase where the Dirac points are merged. Herein, each effective model with its predictions and experimental confirmations will be exhibited.

1.3.1 Quantum field theory in curved spaces

This approach arises of the similarity of involved physical concepts among Quantum Field Theory, general relativity and strained graphene [47]. Since electrons in strained graphene also behave as massless Dirac fermions, an anisotropic Dirac equation is needed. From symmetry group analysis, it is possible to construct a hamiltonian that describes the dynamics of massless Dirac fermions in strained graphene. The system presents twelve symmetries, where the hamiltonian must commutate under these symmetry operations. Hence, a proposed hamiltonian [15, 82, 83] that provides a direct relation with the strain tensor components for non-uniform strain is given by

$$H = H_0 + \sum_{i=1}^{6} g_i H_i + \sum_{i=1}^{6} \tilde{g}_i \tilde{H}_i. \tag{1.10}$$

The first term is the Dirac-like hamiltonian for pristine graphene. The second term, corresponds to the sum of the contributions which are invariant to the symmetry operations for in-plane strains. The second sum is over the six terms that are invariant under the symmetry operations for out-plane strains. These last terms have identical form than the terms in-plane, doing the substitution $u_{ij} \to \partial_i h \partial_j h$, where h is the displacement out-plane, g_i and $\tilde{g}_i$ are the coupling constants that can be obtained from DFT calculation, TB approach or experimental data available. The six terms H_i will be exposed in the following with their respective physical interpretation:

(i) $H_1 = (u_{xx} + u_{yy})\mathbb{I}$, *pseudo scalar potential*. It is a term that can be obtained expanding the TB hamiltonian around the high symmetry point in the deformed first Brillouin zone. Its effect on electronic band structure is very similar to an external electric field, but it is only caused by strain and it can not be considered as an induction of an electric field due to the strain. It was described for first time in the study of electron-phonon scattering in carbon nanotubes [84]. However, ab-initio calculations for electron-phonon interactions estimated that the coupling constant g_1 can be neglected [85].

(ii) $H_2 = (u_{xx} - u_{yy})\sigma_x - 2u_{xy}\sigma_y$, *pseudo vector potential*, where σ_x and σ_y are the Pauli matrices which discriminates the pseudo-spin of A and B triangular sublattices. This term proceeds of the shift in the momentum space of the Dirac cone and it is embodied by a pseudo vector potential, which is very similar to the vector potential in the gauge theory of electromagnetic fields. Its analogy with vector potential of the magnetic field, allowed the prediction of a quantum Hall effect without magnetic field [40], and several analogies with the photonic crystals [36, 86] and quantum confinement [11]. Experimental works in molecular graphene [32], artificial graphene [36], and graphene nanobubbles [35, 87] have confirmed the observation of pseudo LLs due to generation of fictitious magnetic fields [35].

(iii) $H_3 = [(u_{xx} - u_{yy})q_x - 2u_{xy}q_y]\mathbb{I}$, *Dirac cone tilt*, where q_x and q_y are the coordinates of the linear momentum around high symmetry point K. Its effects on the electron dynamics is almost neglegible for strained graphene [24, 67]. However, for uniaxial strain along ZZ direction, its effects are possible to observe on the Fermi velocity beyond 15 % of tensile strain [67]. The tilt of the Dirac cone is responsible of the photoinduction of valley currents [88], magneto-phonon resonance [80, 81], and other effects on the quantum transport [89]. In materials like the organic salt α-(BEDT-TTF)$_2$I$_3$, an appreciable tilting of the Dirac cones was observed [26].

(iv) $H_4 = (u_{xx} + u_{yy})(\sigma_x q_x + \sigma_y q_y)$, *Isotropic Fermi velocity.* This term corresponds to the separation of the strain tensor between isotropic and shear strain contribution. It was obtained from the expansion of the hopping parameters to first order, in the strain tensor components when a TB approach to nearest neighbors was considered. It has been generalized for non-uniform strain, establishing a spatial dependency of the Fermi velocity [83].

(v) $H_5 = u_{ij}\sigma_i q_j$, *Anisotropic Fermi velocity.* This term appears in the same process described above for the H_4 term, taking into account the shear strain contribution. Likewise that H_4, also is valid for non-uniform strain, leading to a spatial and anisotropic description of the Fermi velocity, which is of relevant importance because it is involved in almost all the physical observables of Dirac-like systems.

(vi) $H_6 = [\partial_y(u_{xx} - u_{yy}) + 2\partial_x u_{xy}]\sigma_z$, *Gap opening term.* The effect of this term is very similar to the Zeeman coupling associated to the generation of a pseudo-magnetic field, caused by the inhomogeneity of the strain profile. Further, it offers a new mechanism for the induction of a gap opening in graphene [90].

From this approach, the Fermi velocity tensor can be related with strain tensor components, deriving the terms H_4 and H_5 with a TB model to nearest neighbors. Then, the TB hamiltonian is expanded around a high symmetry point of the undeformed first Brillouin zone $\vec{K} = (4\pi/3a\sqrt{3}, 0)$. Assuming that the hopping parameters change linearly with the bond lengths as $t_j \approx t(1 - \beta\frac{\delta_j}{a})$ [83], the elements of the Fermi velocity tensor are

$$v_{ij} = v_F[\delta_{ij} - \frac{\beta}{4}(2u_{ij} + \delta_{ij}u_{kk})], \tag{1.11}$$

where $v_F = 3ta/2\hbar$ is the Fermi velocity in pristine graphene. The value of the effective Fermi velocity is extracted calculating the squared root of the tensor determinant (1.11)

$$v_F^* = v_F[1 - \frac{\beta}{2}(u_{xx} + u_{yy})]. \tag{1.12}$$

This expression is obtained for comparison with expressions calculated from other effective models. Besides the Fermi velocity prediction, other phenomenologies such as the generation of pseudo electromagnetic fields, zero field quantum Hall effect [40], quantum confinement and electron collimation [69], valley beam splitter [91, 92, 93], and the Goos-Hänchen effect [91] were studied from the present approach. They were predicted initially for strained graphene, but later extended to other graphene-like systems as artificial graphene [36], molecular graphene [32] and graphene nanobubbles [87]. Some of these predictions have been confirmed experimentally [32, 36, 35, 94]. Herein, it is exposed some proposals about this model:

Pseudo electromagnetic fields by strain engineering. The terms H_1 and H_2 of the hamiltonian (1.10) are related with pseudo scalar and vector potentials, respectively. For inhomogeneous strain, these potentials

$$V_s(\vec{r}) = g_1[u_{xx}(\vec{r}) + u_{yy}(\vec{r})] \tag{1.13}$$

$$\vec{A}(\vec{r}) = \pm g_2(u_{xx}(\vec{r}) - u_{yy}(\vec{r}), -2u_{xy}(\vec{r})) \tag{1.14}$$

generate effective electromagnetic fields, where the sign ± indicates the pseudospin valley [15]. Since the coupling constant g_1 is neglegible, only a pseudomagnetic field could be observed [47]. Guinea *et. al.* proposed that applying a strain aligned along three main crystallographic directions, a uniform and strong pseudomagnetic field is induced exceeding 10 T, as shown in Fig. 1.9 [40]. In consequence, a Landau quantization is induced by the ficticious magnetic field which must be evidenced with the appearence of peaks in the DOS. The required conditions were experimentally obtained by Levy *et. al.* through graphene grown on Pt(111) where nanobubbles were formed on the surface [35], LDOS measurements allowed the observation of pseudo-LLs as well as the induction of pseudomagnetic field greater than 300 T.

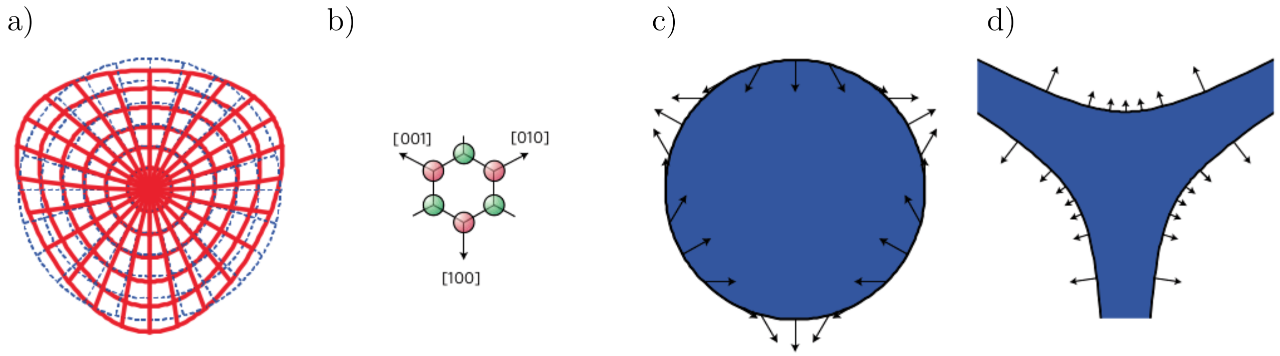

Figure 1.9: Schematic representation of a triaxial strain for the generation of a pseudomagnetic field in graphene. (a) Geometric distortion caused by triaxial strain (red) in comparison with biaxial strain (blue). (b) Specific directions for application of a triaxial strain in graphene. (c) The black arrows are the external forces that must be loaded upon a perimeter's disc of graphene sample and (d) shows the distortion caused for these forces. The figures were taken from ref. [40].

Following this, the searching for pseudomagnetic fields was extended to other systems with similar electronic features that graphene. One example is the molecular graphene, which consists of a distorted hexagonal arrangement of CO molecules adsorbed by Cu(111), that behaves as a nearly free two-dimensional electron system (2DES). Through chemical manipulation, the position of CO molecules were modified for simulating a triaxial strain configuration as shown in Fig. 1.10, where a pseudo Landau quantization can be evidenced.

In other system, a strained honeycomb photonic lattice was designed with dielectric waveguides simulating a triaxially strained hexagonal lattice, see Fig. 1.11. Monochromatic light propagates through the structure tunnelling between neighbouring sites, that are evanescently coupled to one another site [36]. The coupling strength between the waveguides is analog to the hopping parameter in a TB approach to nearest neighbors obeying an exponential decay rule as a function of the separation among waveguides. Thus, solving the coupled-mode equations associated to the problem, a band structure very similar to the obtained in graphene was found. These similarities have been used as a bridge that connects graphene physics with optics [95, 96, 97], leading to the first experimental demonstration of a pseudomagnetic field in optics, which was evidenced from DOS due to apparition of resonance peaks, attributed to the

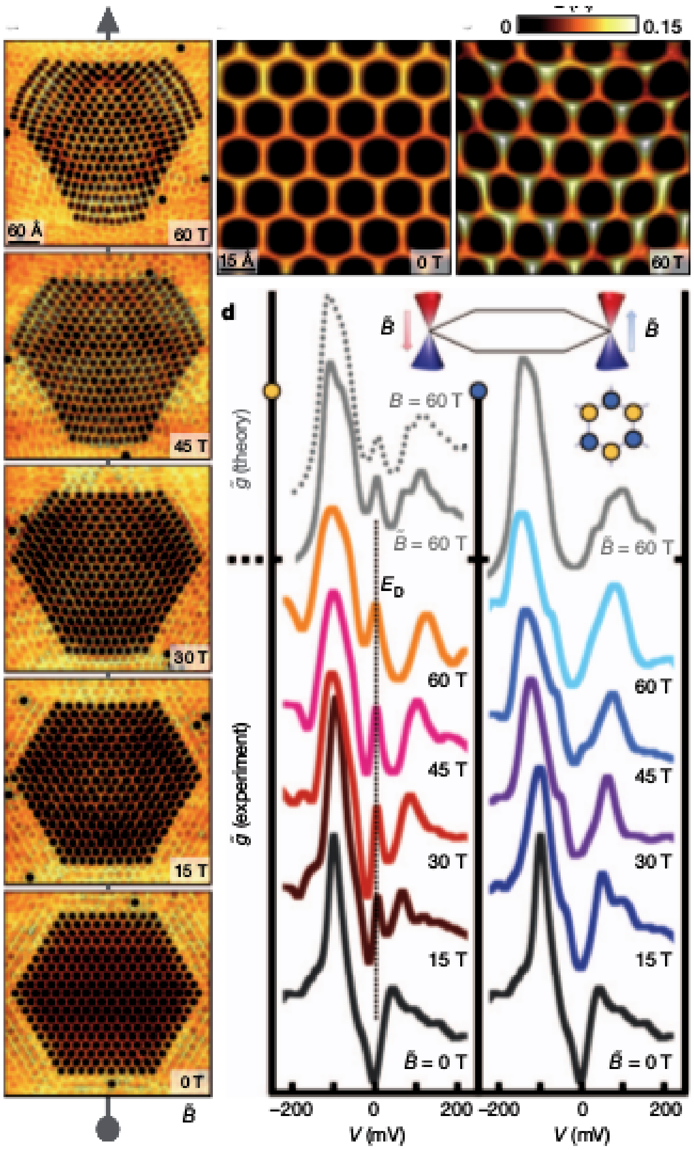

Figure 1.10: Sequences of a triaxial strain simulation using a modifiable arrangement of CO molecules adsorbed by Cu(111). The emergence of pseudomagnetic field is observed in the DOS presenting LLs quantization. Figure took from ref. [32].

generation of photonic LLs [36].

Quantum confinement, tunneling and electron quantum optics analogies. Under this approach, many reported works only incorporated the H_2 term, whose effect on the band structure is the shifting of the Dirac points with respect to the high symmetry points. The other effects of deformation like the tilting of the Dirac cone were considered as corrections. For instance, Pereira and Castro Neto studied the charge carriers transmission on a uniaxially strained

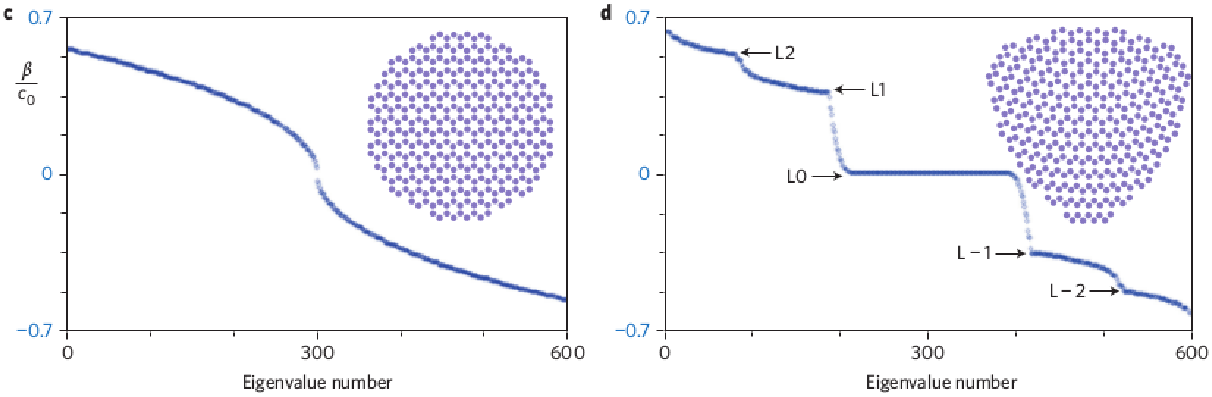

Figure 1.11: Observation of LLs quantization produced by pseudomagnetic field in a triaxially strained honeycomb photonic lattice. This figure was taken from ref. [36].

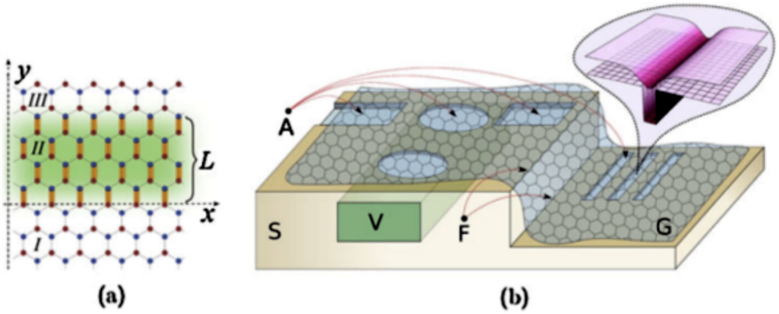

Figure 1.12: (a) Illustration of a strained graphene barrier, the region I and III is conformed by pristine graphene and region II by strained graphene. (b) An experimental proposal of the system shown in (a). Figure took from ref. [69].

graphene region with the interface oriented along ZZ direction [69]. Fig. 1.12 shows a scheme of the system with its possible experimental implementation, where the region I and III are formed by pristine graphene and the region II by uniaxially strained graphene and a potential barrier. Therefore, the electrons and holes satisfy the Dirac equation in the region I and III. In the region II, the description of the charge carriers behavior must be taken into account through the inclusion of a constant pseudo vector potential induced by the uniaxial strain, and entering in the Dirac-like hamiltonian via minimal substitution. From this perspective, KT was shown to be affected under uniaxial strained, having an angular shift which is caused by a finite pseudo vector potential. It is possible to get a quantum confinement, suppressing the transmission

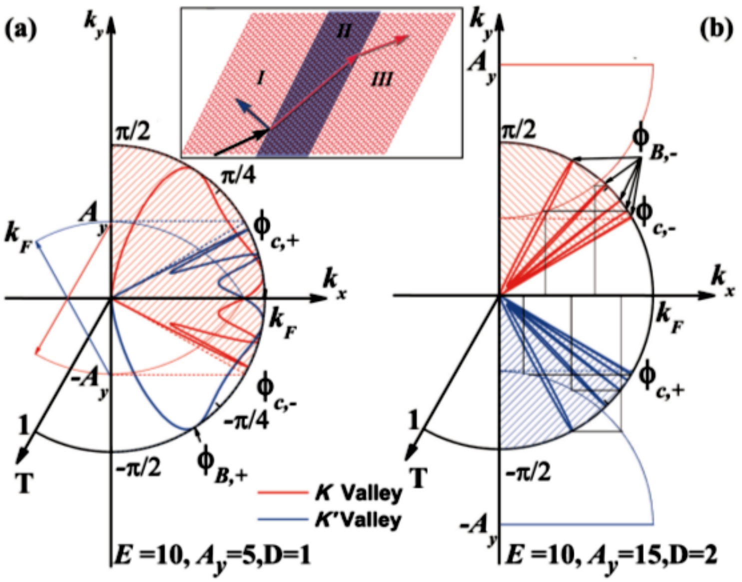

Figure 1.13: Polar electron transmission curves from K (red) and K' (blue) valley as a function of the incidence angle for the system shown in the inset. (a) A valley beam splitter was obtained with $E = 10$, $A_y = 5$ and $D = 1$ and (b) a valley filter with $E = 10$, $A_y = 15$ and $D = 1$. The figure and units are taken and defined in [91].

with a strong pseudo vector potential when the tensile strain is increased. Beam collimation can be obtained for a high potential barrier and a slight doping in the region I. Nevertheless, the inclusion of the Dirac cone distortion has an important contribution already pointed out by other authors [98].

Using the same system and considerations, Zhai *et al.* proposed the realization of optical-like devices [91, 92]. They found that the refraction of Dirac fermions within the strained graphene barrier is valley dependenting, the unpolarized incident beam is divided into two valley-dependent refracted beams. Thus, the strained graphene barrier works as a valley-beam splitter. While for other values of strain, the Dirac fermions from a certain valley are totally reflected and from the other one are refracted, then the barrier works as a valley filter. Also, it was predicted a lateral shift of the reflected beam, of the same way as the Goos-Hänchen effect of the light [99, 100, **?**]. Fig. 1.13 shows the electron transmision for a set of the strain values that illustrate a valley beam splitter and a valley-filter [91].

Returning to the above discussion, the vector potential (1.14) only describes the shifting of

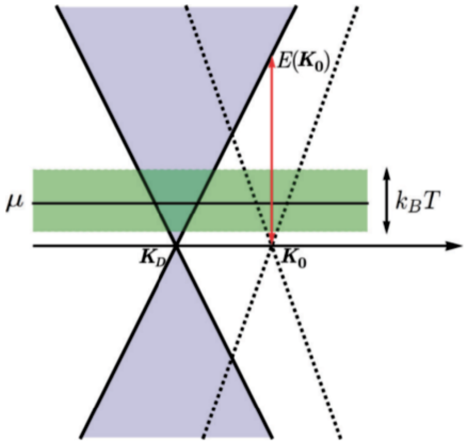

Figure 1.14: Pictorial representation of the Dirac cones in pristine (dotted line) and strained (solid line) graphene with the width of energy (green area) allowed to finite temperature in the observation of a pseudomagnetic field. Red arrow shows as QFTCS could predict a pseudomagnetic field outside the green observable region. This figure was taken from ref. [38].

the Dirac points, but the inclusion of the Dirac cone distortion in graphene and in other Dirac materials with a significant tilting must have a non-negligible contribution. This is because when the Dirac cone changes its shape, the group velocity has not the same direction that the linear momentum. Thus, the predicted optical-like effects with Dirac Fermions for strained graphene [69, 91, 92, 99] should be revisited taking into account the Dirac cone distortion.

Criticism about quantum field theory in curved spaces. The derivation of the H_2 term of this approach, that perfectly describes the most of the results exhibited above, was obtained by first time expanding the TB hamiltonian around high symmetry point of the unstrained first Brillouin zone [47, 84, 102]. All information of the strain was captured by the hopping parameters, establishing a linear relation between hopping and strain tensor components, which is resulted of expand the exponential scaling rule to first order. In a related work, was proved that the exponential scaling rule can be dependent of the strain profile in graphene [60]. In almost all the reports about the topic [11, 37, 38, 40, 72, 103], the exponential scaling rule has been used indiscriminately as a universal rule. On the other hand, it was noted that the terms H_3, H_4 and H_5 and the absence of an explicit inclusion of the lattice deformations in the direction cosines in the TB approach, could have observable effects hitherto ignored. Aware of these shortcommings, Kitt *et al.* tried to solve the absence of an explicit inclusion of the lattice deformations, finding corrections and also a K-dependency of the pseudo-magnetic field, but considering again a linear relation between the hopping parameters and strain tensor [90, 104, 105, 106]. The linear relation between the hopping parameters and strain tensors components led to the effective hamiltonian (1.10) linearly related with the strain tensor [15, 83, 106]. Hence, the previous estimation of the coupling constants through DFT calculations, have been performed without take into account the relaxation of atomic positions. Thus, a different proposal should allow the estimation of coupling constants from more realistic calculations, where the relaxation of the atomic positions could be considered [67]. The hamiltonian (1.10) indicates us that the QFTCS model only is valid and applicable to Dirac materials within a linear regime, even knowing that there are experimental and theoretical evidence that graphene is a material with a considerable nonlinear elasticity range [35, 107, 108]. On this point, Crosse developed a differential geometry method, consisting in the derivation of a strain theory for large displacements of finite lengths terms [103]. With this proposal, a comparable pseudomagnetic field with respect to the linear strain contribution was obtained. Other solution was given by Ramezani *et al.*, who revisited the QFTCS model using a TB approach to nearest neighbors, where a systematic expansion of the exponential scaling rule in terms of the strain tensor to second order was developed. Thus, previous results was generalized adding seven extra terms to second order in the hamiltonian (1.10), that leads to a best description of the pseudo-magnetic field effects beyond of the linear region [39]. However, the performing of an expansion of the hamiltonian around the high symmetry point could not guarantee the linearity of the dispersion relation. Therefore, the hamiltonian (1.10) must be once more modified, adding extra terms to second order in the linear momentum, apart of the terms aforementioned by Ramezani. Other overlooked aspect was pointed out by Oliva-Leyva and Naumis [38]: a TB hamiltonian of strained graphene expanded around an arbitrary point, different to the Dirac point, could not explain correctly the obtention of a pseudo-magnetic field for in-plane deformations, as pictorial represented in Fig. 1.14. This is because at finite temperature the energy $E(K_0)$ could be out of the required range $|E(K_0) - \mu| \leq k_B T$ for its observation. These necessary modifications in the description of the electron dynamics from the QFTCS make it requires too many terms, converting it in a limitated effective model. Hence, a suitable explanation of the induction of pseudomagnetic field and other related effects must be performed from an approach with an effective hamiltonian developed around the Dirac point.

1.3.2 Effective model for motion and merging of Dirac points in Dirac materials

The model proposed by Montambaux *et al.*, takes into account the motion and merging of Dirac points in two-dimensional crystals with Dirac cones in its electronic band structure [13, 24, 109, 110]. From TB approach, an effective hamiltonian was derived for low energy regime, expanding the hamiltonian around the M point of the first Brillouin zone and keeping the quadratic term in q_x. The so called universal hamiltonian was obtained

$$H(\vec{q}) = \begin{pmatrix} 0 & \Delta + \frac{q_x^2}{2m^*} - icq_y \\ \Delta + \frac{q_x^2}{2m^*} - icq_y & 0 \end{pmatrix}, \tag{1.15}$$

where $\vec{q}$ is the linear momentum vector around the M point, m^* is an effective mass along x axis, c is an associated velocity to the y-direction, and Δ is the parameter that drives the TPT shown in Fig. 1.15. The physical meaning of Δ is phase-dependent, $-\Delta$ is the energy at the M point which corresponds to a saddle point for the conduction band within semimetallic phase, while 2Δ is the band gap value in the insulator phase. All these quantities can be related with the hopping parameters and the atomic positions of the crystal [13]. Diagonalizing the hamiltonian (1.15), the following dispersion relation was obtained

$$E(\vec{q}) = \pm\sqrt{(\Delta + \frac{q_x^2}{2m^*})^2 + c^2q_y^2}, \tag{1.16}$$

which are the energy bands shown in Fig. 1.15. Since the system is invariant under time-reversal operation, the apparition of Dirac points occur in pairs, one located at K_D point and the other in $-K_D$. Mathematically, the Δ parameter moves two opposite Dirac point to merge at the time-reversal invariant M point. Thus, when $\Delta < 0$ the involved Dirac points in the TPT are separated having each one opposite Berry's phase and the dispersion relation (1.16) displays two insulated Dirac cones. For $\Delta = 0$, the Dirac points have merged in M point occurring the TPT, where the Berry's phases are annihilated. Hence, the two Dirac cones disappear and in their place a hybrid surface between a Dirac cone along q_y direction and a paraboloid along the

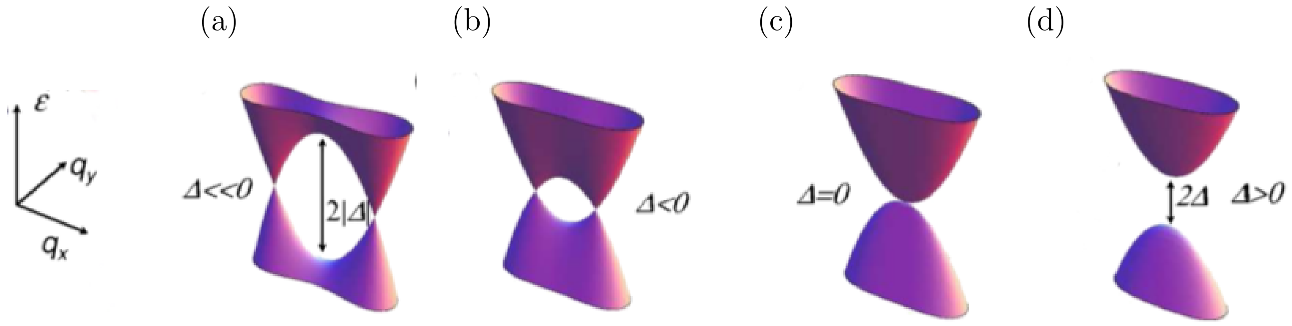

Figure 1.15: Merging of two Dirac cones when the parameter Δ is increased from (a) to (d) and changing the sign at TPT for $\Delta = 0$ in (c). The dispersion relation stays linear along the q_y direction [13].

other direction is obtained. Therefore, novel physical effects could be observed for merging of Dirac points. Although, this TPT seems to be inaccessible for graphene, other systems such as α-(BEDT-TTF)$_2$I$_3$ [26], cold atoms in optical lattices [16, 111] and VO$_2$/TiO$_2$ heterostructures [112] offer an opportunity to appreciate this phenomenology. In the case of $\Delta > 0$, the Dirac material presents an insulator phase with a parabolic dispersion relation.

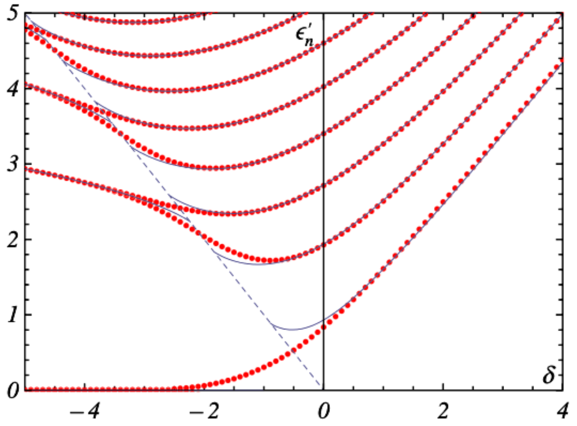

Figure 1.16: Evolution of LLs spectra through the universal parameter $\delta(\Delta)$ for the levels $n = 0, 1, 2$ and 3. Dotted red curves are obtained solving numerical differential equation derived from effective hamiltonian (1.15), and blue curves are calculated from semi-classical quantization rule. Dashed line indicates the value of energy in the saddle point, where a progressive lifting of the two valley degeneracy occurs when Δ is increased. Figure took from ref. [110].

LLs as a function of the Δ *parameter.* The Landau level spectrum in presence of a magnetic

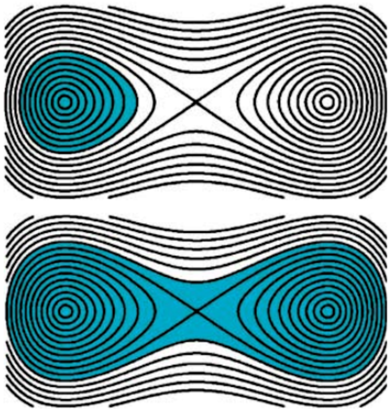

Figure 1.17: Isoenergy contour curves and blue areas that represent the orbit area $S(\epsilon) = 2\pi enB$ covering one valley and $S(\epsilon) = 2\pi e(n + 1/2)B$ for both valleys, in the determination of the LLs from semi-classical quantization rule. This figure was taken from ref. [109].

field was studied in detail under this approach [13, 109]. It was found that the dependency of the LLs with the magnetic field changes through the TPT. Fig. 1.16 shows the evolution of LLs as a function of the adimensional δ parameter defined as $\delta = \Delta\left(\frac{2}{m^*\omega^2 c^2}\right)^{1/3}$ for the levels $n = 0, 1, 2$ and 3, where the red dotted curves represent the numerical solution of the differential equation derived from the hamiltonian (1.15) with magnetic field B. The blue solid curves are obtained from semi-classical quantization rule $S(\epsilon) = 2\pi(n + \gamma)eB$, where $S(\epsilon)$ is the area of the orbit of ϵ energy in reciprocal space shown in Fig. 1.17, and γ is a phase related with the Maslov contribution and Berry's phase [113]. Thus, analytical expressions can be given for LLs spectra [13]

$$F_- = \sqrt{1-r}\left[E\left(\sqrt{\frac{2r}{r-1}}\right) - (r+1)K\left(\sqrt{\frac{2r}{r-1}}\right)\right], \qquad r < -1 \tag{1.17}$$

$$F_+ = \sqrt{|r|}\left|2E\left(\sqrt{\frac{r-1}{2r}}\right) - (r+1)K\left(\sqrt{\frac{r-1}{2r}}\right)\right|, \qquad r > -1. \tag{1.18}$$

where $r = \epsilon/\Delta$, $K(x)$ and $E(x)$ are the complete elliptic integral of first and second kind, respectively [114]. These expressions allow to get the LLs expression as a function of the quantum number n and B. When $\Delta < 0$, the LLs energy is written as $\epsilon_n \propto \mathrm{sgn}(n)\sqrt{|n|B}$ with $n = 0, \pm1, \pm2, \ldots$, valid for low energy and magnetic fields. For high energies, more terms are needed to include other effects like trigonal warping. Returning to the Fig. 1.16, the blue dashed line indicates the energy value in the saddle point. Here, the two-fold degeneracy is

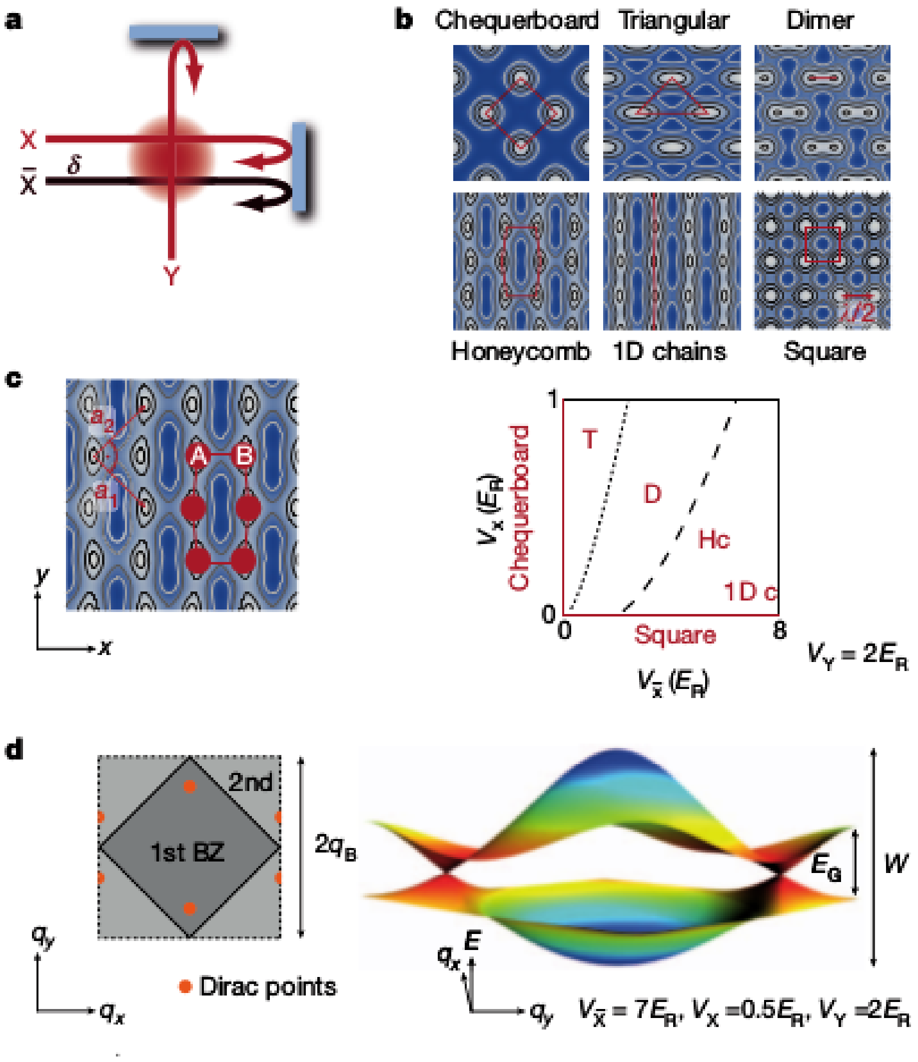

Figure 1.18: Sequences of the experimental setup from [33]. (a) Ultracold Fermi gas of ^{40}K was confined using three retro-reflected laser beams. (b) Tuning the amplitudes and frequencies of the lasers is possible to induce topological transition phase at following two-dimensional optical lattices: chequerboard, triangular, dimer, honeycomb, 1D chain and square. (c) A deformed honeycomb lattice where triangular sublattices A and B are identifyed, and (d) laser superpositions create a band structure similar to strained graphene with Dirac points and cones.

lifted due to the valley communication between Dirac cones. When $\Delta = 0$, the LLs change its dependency with the magnetic field to $\epsilon_n \propto \mathrm{sgn}(n)[(|n| + 1/2)]^{2/3}$ [115]. For $\Delta > 0$, the energy of LLs has the same expression of an insulator $\epsilon_n \propto \mathrm{sgn}(n)(|n| + 1/2)B$.

Experimental confirmation of the merging Dirac points. The merging of Dirac points was confirmed experimentally using a tunable and two-dimensional optical lattice with an ultra-cold Fermi gas of ^{40}K atoms [33]. The confinement was performed with three retro-reflected laser beams, two of them mutually perpendicular, in the way that varying the frequencies and amplittudes, the square, triangular, dimer and honeycomb structures can be created, as they are shown in Fig. 1.18. With specific values of the wavelength, intensity and phase, for the simulation of a hexagonal lattice. The superposition of the lasers potential lead to a energy-like landscape given by

$$V(x,y) = -V_{\overline{X}}\cos^2(kx+\theta/2) - V_X\cos^2(kx) - V_Y\cos^2(kx) - 2\alpha\sqrt{V_XV_Y}\cos(kx)\cos(ky)\cos(\phi) \tag{1.19}$$

where $V_{\overline{X}}, V_X$ and V_Y are the laser beam amplitudes, α is the visibility of the interference pattern and k the wave vector. These parameters produce a band structure similar to an anisotropic Dirac material with its respective formation of Dirac points, which can be moved controlling the phase θ having the same role that the universal parameter Δ of the model described above. The atomic cloud presents Bloch oscillations along q_x direction in the squared first Brillouin zone caused by the magnetic field of the lasers. A fraction of this cloud had a q_y that matched with the Dirac point, observing a transference to the second energy band. The maximun transfered fraction of the atomic cloud was obtained when the Dirac points were driven towards the corners of the first Brilluoin zone, where a merging was reached, as shown in Fig. 1.19. Therefore, this experiment confirmed the TPT for an ultra-cold Fermi gas in an optical lattice, which can be theoretically explained through the approach proposed by Montambaux [13, 109].

1.3.3 Effective models from the Dirac points

Several authors have studied the electronic-ground properties of strained graphene from different assumptions but with a same point of view, the derivation of an effective hamiltonian that explains and describes the anisotropic dynamics of the massless Dirac fermions caused by strain, within low energy regime around the Dirac points. Throughout this subsection, the proposals of each author with their respective predictions will be show some of these without experimental confirmation yet. In contrast to QFTCS, these effective models for uniform strain do not use

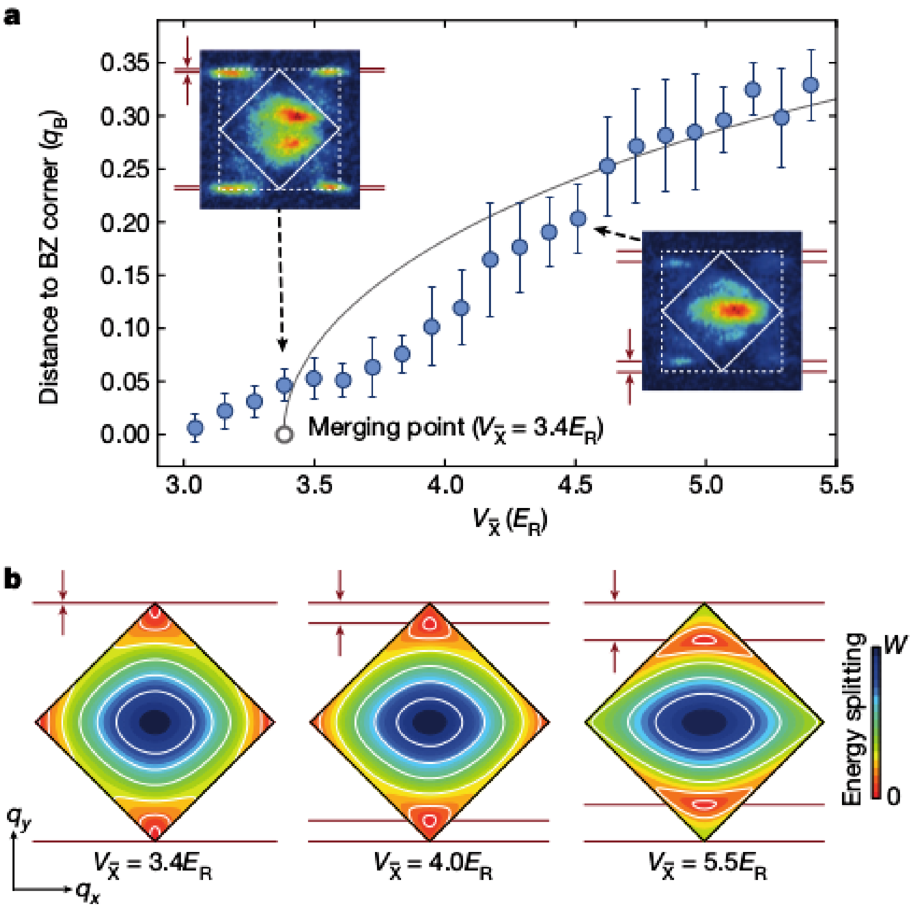

Figure 1.19: Movement and merging of Dirac points in honeycomb optical lattice. (a) Dirac points are moved modulating $V_{\overline{X}}$ amplitude, the insets show the atomic cloud in the reciprocal lattice, a little part of the cloud is transferred to the second band with $V_{\overline{X}} = 4.5$. At merging $V_{\overline{X}} = 3.4$, the maximum tranference is reached producing the TPT. (b) Energy contours in the first Brillouin zone where the movement and merging of Dirac points can be observed. Figure took from ref. [33].

the scalar and pseudo vector potential, reducing the number of involved terms. This allow to evidence the effect of distortion of the Dirac cone on the Fermi velocity, neglected by the most of works using the QFTCS.

Generalized Weyl hamiltonian. Goerbig *et al.* proposed a model for two spinor fermions restricted to a 2D space, with a reduced Weyl hamiltonian that reads as [68]

$$H = \vec{w}_0 \cdot \vec{q}\sigma^0 + w_x q_x \sigma^x + w_y q_y \sigma^y \tag{1.20}$$

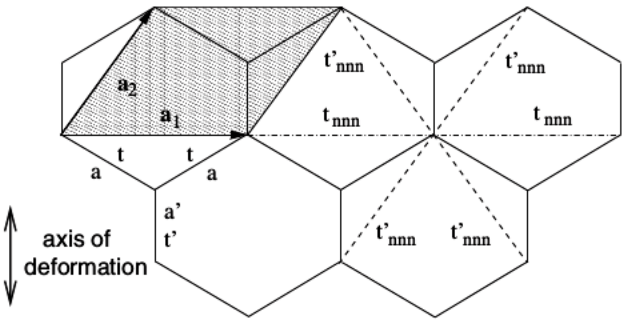

Figure 1.20: Quinoid-type deformation of the honeycomb lattice. Due to the symmetry, two hopping parameters to nearest neighbors are equals and one is different, which are denoted by t and t'. Dashed lines indicate the six next nearest neighboring sites, also presenting only the two different hopping parameters t_{nnn} and t'_{nnn}. This figure was taken from ref. [68].

where q_x and q_y are the components of the linear momentum around the Dirac points. This approach consists of four independent parameters given by the components of the vectors $\vec{w} = (w_x, w_y)$ and $\vec{w}_0 = (w_{0x}, w_{0y})$ which are the 2D anisotropic and tilt velocities, respectively. These parameters can be related with the hopping parameters in a TB approach to next nearest neighbors for hexagonal lattices with quinoid-type deformations, where two hopping t and t' to nearest neighbors and two hopping parameters t_{nnn} and t'_{nnn} to next nearest neighbors are involved, as seen in Fig. 1.20. Such conditions are perfectly satisfied in systems as graphene uniaxially strained along ZZ and AC direction, and 2D organic compounds as α-BEDTIFI$_2$ [11, 26, 68, 116]. Diagonalizing the Weyl hamiltonian (1.20) yields the dispersion relation

$$\epsilon_\lambda(\vec{q}) = \vec{w}_0 \cdot \vec{q} + \lambda\sqrt{w_x^2 q_x^2 + w_y^2 q_y^2} \tag{1.21}$$

where λ denotes the conduction band with $\lambda = +1$ and the valence band with $\lambda = -1$. Equation (1.21) represents a tilted Dirac cone with the semi-major and semi-minor axes of the elliptical transversal section parallel to the q_x and q_y axes. The wavefunctions are $|\Phi\rangle = \frac{1}{\sqrt{2}}(1, \lambda e^{i\phi_q})$ with $\tan\phi_q = w_y q_y / w_x q_x$. Since the chirality operator defined as $\hat{C} = (w_x q_x + w_y q_y)/\sqrt{w_x^2 q_x^2 + w_y^2 q_y^2}$, conmmutes with the hamiltonian (1.20), there is a two-fold valley degeneracy. Thus, -H describes the dynamics of the Dirac fermions at the other valley.

LLs spectra was derived doing the Peierls substitution in the free-field hamiltonian (1.20), through a second quantization treatment using the annihilation and creation operators, obtaining

$$\epsilon_n = \mathrm{sgn}(n)\sqrt{2|n|}\frac{v_F^*}{l_B}, \tag{1.22}$$

with $n = 0, \pm 1, \pm 2, \ldots$, v_F^* is the effective Fermi velocity which is related with the general Weyl hamiltonian parameters as $v_F^* = \sqrt{w_x w_y}[1-(w_{0x}/w_x)^2-(w_{0y}/w_y)^2]^{3/4}$, and l_B is the magnetic length [24]. Clearly, the LLs spacing is affected when v_F^* changes with strain. Under this model, the same authors studied the Fermi velocity modulation for quinoid-type deformed in graphene [24, 68]. It was used a TB calculation to find $\vec{w}$ and $\vec{w}_0$ as a function of the tensile parameter ϵ. The parameters t and t' as well as t_{nnn} and t'_{nnn} were related with tensile strain, using the Harrison scaling rule [117], expanded to first order in ϵ. Since the effective velocities were found in terms of the hopping parameters and deformed lattice vector to be $w_x = \sqrt{3}ta\sin\theta$, $w_y = \frac{3}{2}t'a(1+2\epsilon/3)$, $w_{0x} = 2\sqrt{3}(t_{nnn}a\sin 2\theta + t'_{nnn}a\sin\theta)$ and $w_{0y} = 0$, a direct and linear expression of the effective Fermi velocity, neglecting the tilt effect with strain, was obtained

$$v_F^* \approx v_F(1-\epsilon/3), \tag{1.23}$$

which is expected to have an experimentally observable appreciation for a strain up to 10% [68].

Combination of an electric field E and uniaxial strain on graphene have been explored from this point of view [80, 118]. In pristine graphene, Lukose *et al.* shown that LLs spacing also can be modified by an in-plane electric field, because of the competition between the confinement produced by the magnetic field and the tendency to open the trajectories of the particles due to the inclusion of the electric field [119, 120]. Such effect was observed with the collapse of the LLs spectra through gated graphene structures [121]. For systems with quinoid type deformation and an appreciable tilting of Dirac cone [118], the presence of an electric field induces a lifting of the two-fold valley degeneracy, and the LLs spacing become valley dependent. Therefore, some authors have proposed a possible verification of the effects of the tilt through magnetorresistance measurements [116] and quantum transport [89], since the Dirac cone anisotropy does not affect the Fano factor, but the tilting has its contribution in that quantity. Recently, the possible experimental observation of a magnetophonon resonance by the tilting of the Dirac cone has been predicted, producing a double peak structure due to the lifting of the valley degeneracy [80, 81].

Effective hamiltonian for uniaxially strained graphene. From TB approach to nearest neighbors for uniaxially strained graphene, Pellegrino *et al.* developed a model for low energy regime in order to study the transport properties of charge carriers crossing regions with different levels of strain [98], the linear response correlation functions [122], and the effect of uniaxial on plasmon excitacions [123]. In the TB approach, it was taken into account the observations performed by Pereira *et al.* [11], about all information of uniaxial strain entries in the hopping parameters, without consider the angular distortion of the deformed lattice vectors via direction cosines in the Bloch wavefunctions. Following the same idea to get an effective hamiltonian directly related with the strain tensor components as in QFTCS, the Papaconstantopoulus' scaling rule is expanded to first order on the rotated uniaxial strain tensor. Thus, expanding TB hamiltonian around the Dirac points and conserving to first order the linear momentum terms, the effective hamiltonian of this model is written as [98]

$$H = \hbar v_F U^{\dagger}(\theta)[\sigma_x(1-\lambda_x\epsilon)q_x + \sigma_y(1-\lambda_y\epsilon)q_y]U(\theta), \tag{1.24}$$

where ϵ and θ are the uniaxial strain tensor parameters, $\lambda_x = 2\kappa_0 - 1$ with $\kappa_0 \approx 1.6$ as the value of the logarithmic derivate of the nearest neighbor hopping in pristine graphene, $\lambda_y = -\lambda_x\nu$ being ν the Poisson's ratio with a value estimated of 0.165 in graphite [124], and $U(\theta)$ is the rotation operator in the sublattice AB space

$$U(\theta) = \begin{pmatrix} 1 & 0 \\ 0 & \mathrm{e}^{-i\theta} \end{pmatrix}. \tag{1.25}$$

The system described in Fig. 1.12 was studied by Pereira and Castro Neto using the QFTCS [69], but also was analyzed by Pellegrino *et al.* under the current model [98]. They probed that including the anisotropy of the Dirac cone on the tunneling transmission calculations, an important difference in the prediction of resonance peaks can be evidenced when the energy is increased. Comparing with the obtained in previous work [69] for uniaxial strain along ZZ ($\theta = 0$) and AC ($\theta = \frac{\pi}{2}$) shown in Fig. 1.21, there is an evident difference of the tunneling transmission for uniaxial strain along ZZ and AC direction. The explanation given by Pellegrino *et al.* about the asymmetric transmission for AC direction, was attributed to the absence of the other Dirac cone. Thus, the global symmetry would be restored upon inclusion of the second Dirac cone. This observation is true for an arbitrary strain direction distinct to ZZ and AC

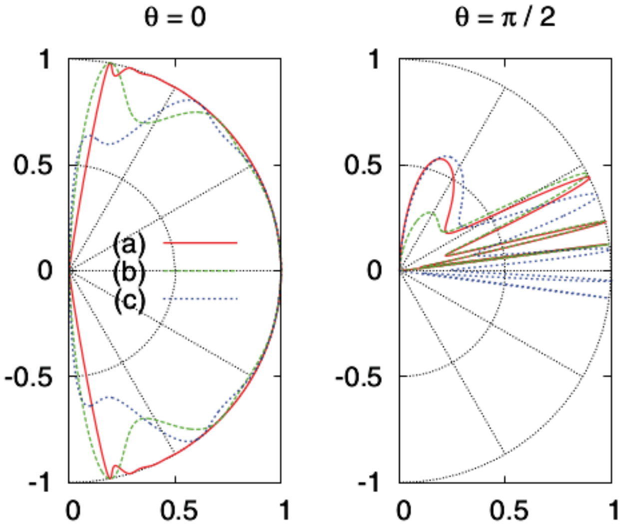

Figure 1.21: Electron transmission probability as a function of the incidence angle for uniaxial strain in graphene along the ZZ ($\theta = 0$) and AC ($\theta = \pi/2$) directions using the energy $E = 80$ meV and a tensile strain $\epsilon = 0.03$. The red (dash-green) curves are the transmission probability calculated from QFTCS (current model) with a potential barrier of $U_g = -20$ meV. Dotted blue curve was obtained from the current approach with $U_g = 0$ meV. Figure took from ref. [98].

but, due to the traslational symmetry of the system on y direction when graphene is uniaxially strained along AC, the tunneling transmission must be the same when the ϕ phase is changed by $-\phi$. The aparent asymmetric transmission in AC is due to an error in the calculation of the Dirac point position [98], which was not considered by Cao *et al.* in their study on the effect Goos-Hänchen for the same system [125].

In the sake of future comparisons, is instructive to extract the expression of the effective Fermi velocity in the hamiltonian (1.24)

$$v_F^* = v_F[1 - \frac{1}{2}(1-\nu)\lambda_x\epsilon]. \tag{1.26}$$

Anisotropic Fermi velocity was studied by Rostami and Asgari considering the current approach and including the electron-electron interaction from Hartree-Fock approximation [72]. They showed how the Fermi velocity is reduced through strain and doping, as well as how the modulation of the Fermi velocity affects the bulk compressibility when the charge density changes, having a good agreement with experimental observations [75].

Effective model for uniform and non-uniform strain in graphene. Recently, Oliva-Leyva and Naumis derived an effective model from TB approach to nearest neighbors for unifom strain in graphene [38]. The difference with the development by Pellegrino *et al.*, is that they considered the deformed lattice vectors on direction cosines in the Bloch expansion. Likewise, TB hamiltonian was expanded to first order around the Dirac points in the linear momentum. The relation of this novel hamiltonian with the uniform strain tensor was established through the expansion of Papaconstantopoulus' scaling rule to first order in the uniform strain tensor, obtaining

$$H = v_F \vec{\sigma} \cdot (\overline{I} + \overline{\epsilon} - \beta\overline{\epsilon}) \cdot \vec{q}, \tag{1.27}$$

where $\overline{I}$ is the 2×2 identity matrix, $\overline{\epsilon}$ is the uniform strain tensor and β is the Grüneisen parameter with a value of 3.37 [126]. The effective Fermi velocity can be directly extracted obtaining

$$v_F^* = v_F(1 + \epsilon - \beta\epsilon), \tag{1.28}$$

where ϵ is the tensile strain. Several effects were studied from hamiltonian (1.27) like AC conductivity [78], generalizing previous results obtained with other approaches [37, 77]. Also, was studied a tunable dichroism and optical absorption in graphene with uniform strain [127], where the transparency, magnitude and direction of a uniform strained graphene sheet can be determined using linearly polarized light under normal incidence. Other authors have studied the Casimir interactions in strained graphene using this approach [128]. Later, this model was extended for non-uniform strain and dislocations, leading an emergent gravitational like-field [129, 130, 131, 132].

Chapter 2

Methodology

We use the elasticity theory and TB method for the study of electronic properties modulations of graphene subjected to loads. The band structure modified by strain was calculated with the TB method, revealing a distortion and a shift of the Dirac cones. The study of the strain effects on the electronic band structure of graphene, lead us to the construction of a novel model called Geometrical Approach, which only considers the geometrical changes of the Dirac cone, showing a direct way to relate physical properties with Dirac cone parameters. Thus, the Geometrical Approach provides a versatile way for the study of other materials presenting distorted Dirac cones.

In the present chapter, we expose the involved concepts of elasticity theory and TB method applied to graphene, which are useful in the development of the main results in the present thesis. Also, we underline the frequent route followed for the study of the strained graphene and related systems. We start from the deformed bond lengths obtained with elasticity theory, which are used in the hopping scaling rule relation necessary in a TB calculation. Later, TB hamiltonian is expanded around special points proving that electrons are similar to massless Dirac fermions.

2.1 Small-strain elasticity theory in two-dimensional structures

The importance of the study of elastic behavior in materials subjected to loads arises because a load can be applied with the goal of design a nanodevice for a specific function. Also, a load can be accidentally applied with the manipulation of the sample when it is synthesized. These motivations had led to the development of concepts and models for the physical understanding of the elastic response in such systems to external forces. In particular the case of two-dimensional structures as graphene is interesting, since offers the opportunity of tailor quantum transport by strain-engineering.

With respect to the response of a material subject to a load, two fundamental concepts are involved: the first of them, related with the loads, is mathematically described by the *stress*. The second concept is the *strain*, which quantifies the deformation of the material caused by the loads. Materials show a wide variety of behaviors under loads, and depending of its response can be clasified as *elastics*, if its original state is fully restored upon unloading or *elastic-plastic*, when its original state is not completely restored. Thus, the specific elastic behavior of the material is determined for a stress-strain relationship, established trough a constitutive equation. Such relation allows to make a clasification of the problem to treat from four regimes [107], which are resulted of the combination of two aspects; one is refered to the geometrical deformation of material that can be either small or large, while the other aspect, corresponds to the linear (Hookean) or nonlinear elastic response. The most known regime occurs for problems with small deformations and Hookean elastic response, subject studied by the classical elasticity theory of isotropic and homogeneous materials. This fundamental stress-strain relationship is characterized by a linear constitutive equation. Herein, the main interest is adressed to materials with nonlinear behavior to small deformations, since several two-dimensional structures as graphene fall within this regime, where a nonlinear stress-strain constitutive equation is needed [108]. Further regimes and related situations with linear or nonlinear behavior and large deformations require an explicit formulation of finite elasticity within a Lagrangian description [133, 134].

2.1.1 The strain tensor

Under applied forces, the material exhibites some change in the shape or (and) volume. Choosing a coordinates system in some particular point, the vector $\vec{r}$ denotes the position of a point in a body without load. Under the action of the forces, the new position of each point is located at $\vec{r}\,'$. Thus, all points present a displacement respect to their original position, being quantified by $\vec{u} = \vec{r}\,' - \vec{r}$, where $\vec{u}$ is the *displacement vector*. Knowing $\vec{u}$ as a function of $\vec{r}$, the deformation of the whole material is determined and therefore, the infinitesimal distance dl' between two points in the deformed material can be calculated using the displacement vector. Since $d\vec{r}\,' = d\vec{r} + d\vec{u}$ with $d\vec{u} = \vec{\nabla}\vec{u} \cdot d\vec{r} = \left\{\frac{1}{2}\left[\vec{\nabla}\vec{u} + (\vec{\nabla}\vec{u})^T\right] + \frac{1}{2}\left[\vec{\nabla}\vec{u} - (\vec{\nabla}\vec{u})^T\right]\right\} \cdot d\vec{r}$, the first term in the brackets is defined as the *small-strain tensor* and denoted in components by

$$u_{ij} = \frac{1}{2}\left(\frac{\partial u_i}{\partial x_j} + \frac{\partial u_j}{\partial x_i}\right), \tag{2.1}$$

while the second term is the *local rotation tensor* defined as

$$\omega_{ij} = \frac{1}{2}\left(\frac{\partial u_i}{\partial x_j} - \frac{\partial u_j}{\partial x_i}\right). \tag{2.2}$$

Hence, the infinitesimal distance for deformed body is $dl' = dl^2 + 2d\vec{r} \cdot \mathbf{u} \cdot d\vec{r}$ where dl is the infinitesimal distance for undeformed system. Within the regimes of small deformations linear and nonlinear elastic behavior, the quadratic term $d\vec{r} \cdot (\mathbf{u} + \omega)^T(\mathbf{u} + \omega) \cdot d\vec{r}$ is always neglected because it is expected that $\mathrm{Tr}(\mathbf{u}) << 1$ for these regimes. Notice that dl' does not depend of the local rotation tensor ω, since represents only a rotation without a relative change of the distance among the points of the system. Therefore, the relevant information about deformation falls on the strain tensor $\mathbf{u}$, having three important properties: the first, the small strain tensor is symmetric thus, the diagonalization is always possible at any given point. Second, its eigenvectors determine the directions of the principal axes and the eigenvalues indicate the value of the extension or the compression for each corresponding axis. Finally, a vector $\vec{v}_0$, defined from the reference, can be expressed in the current configuration as $\vec{v} = (\mathbf{1} + \mathbf{u})\vec{v}_0$. From these properties, some useful geometrical quantities can be derived using the global relations as the variation of volume $\Delta V = \int_V \mathrm{Tr}(\mathbf{u})dV$, the variation of area $\Delta S = \int_S(\mathrm{Tr}(\mathbf{u}) - \hat{n} \cdot \mathbf{u})\hat{n}$, where $\hat{n}$ is a unitary vector perpendicular to the surface, and the variation of length $\Delta L = \int_l \hat{t} \cdot \mathbf{u}\hat{t}$, being $\hat{t}$ the unitary vector tangent to the line l.

2.1.2 The stress tensor

Deformation is the result of the application of forces on the material, appearing internal forces that tend to balance the system. Such internal stress has a molecular origin with a shortened range action among small neighbor portions. These internal stresses are considered in continuum elasticity as near action, whereas the exerted forces by the surroundings have a large range effect, and they act only on the contact surface [107, 135].

In order to calculate the net force $\vec{F}$, the force-density $\vec{f}$ is integrated through a portion of volume V, which can be expressed as $\vec{f} = \vec{\nabla} \cdot \sigma$ where σ is the stress tensor. In this way, a surface integral is obtained using the divergence theorem

$$\vec{F} = \int \vec{\nabla} \cdot \sigma dV = \int \sigma \cdot d\vec{S}. \tag{2.3}$$

The stress tensor components σ_{ij} are the tangential force per unit area on the plane defined by $i \neq j$, while σ_{ii} is the force per unit area along i direction. $d\vec{S}$ is the area element vector perpendicular to the surface.

2.1.3 Balance equations

General elastic properties of bodies under external forces can be obtained when the mechanical equilibrium is guaranteed. Since the net force in a body is zero in the equilibrium, a continuity equation is obtained

$$\vec{P} + \vec{\nabla} \cdot \sigma = 0, \tag{2.4}$$

where $\vec{P}$ is the external force on unit area acting on the body. Equation (2.4) is solved using the boundary condition $\vec{P_s} = \sigma \cdot \hat{n}$ where $\vec{P_s}$ is the force per unit area on the surface and $\hat{n}$ is a unit vector along the outward normal direction. This boundary condition must be satisfied on the whole surface of the body. The second equation that complete the equilibrium description of the system is given by the rotational moment of the forces $\vec{\tau}$

$$\begin{aligned} \vec{\tau} &= \int \vec{r} \times \vec{\nabla} \cdot \sigma dV && (2.5) \\ &= \int \vec{\nabla} \cdot (\vec{r} \times \sigma) dV - \int (\sigma - \sigma^T) \cdot \mathbb{I} dV && (2.6) \\ &= \oint \vec{r} \times \sigma \cdot d\vec{S} = 0. && (2.7) \end{aligned}$$

Then, using the divergence theorem in (2.7), the important result that the stress tensor is symmetrical $\sigma_{ij} = \sigma_{ji}$ was obtained.

2.1.4 Constitutive equation

Balance equations describe the mechanical equilibrium of the system without the elastic specifications of the material. Thus, a complete description of the elastic properties of a particular material is given by the constitutive equation, which can be interpreted as the fingerprint of the elastic behavior of a body. Constitutive equation establishes the relation between stress and strain. In condensed matters, the internal forces are conservatives then the stress-strain relationship can be derived from a potential energy U as

$$\sigma = \vec{\nabla}_{\mathbf{u}} U. \tag{2.8}$$

The last expression is the most important equation of the elasticity theory, indicating that any constitutive equation can be derived from the strain energy function, where U provides a complete information about the elastic response of the stressed material. In a nonlinear isotropic material is convenient to expand U in a power series with respect to u_{ij} [107]

$$U(\mathbf{u}) = \frac{1}{2}\lambda_{ijkl}u^{ij}u^{kl} + \frac{1}{6}\lambda_{ijklmn}u^{ij}u^{kl}u^{mn} + O(\mathbf{u}^4), \tag{2.9}$$

where λ_{ijkl} and λ_{ijklmn} are the elastic tensor modulus to second and third order, respectively. For a homogeneous material with linear elastic behaviour, the first term in (2.9) leads to the generalized Hooke's law [135], which can be written in a tensorial form as

$$\sigma_{ij} = \lambda_{ijkl}u^{kl}. \tag{2.10}$$

This expression has validity for any crystalline symmetry, where the elastic tensor modulus λ_{ijkl} has a total of 21 independent components as consequence of the strain and stress tensor properties. The number of independent tensor modulus components can be reduced according to the crystal symmetries and with a suitable choice of the coordinate system [135]. Thus, the triclinic crystal has 18 elastic independent modulus, whereas monoclinic has 12, orthorhombric

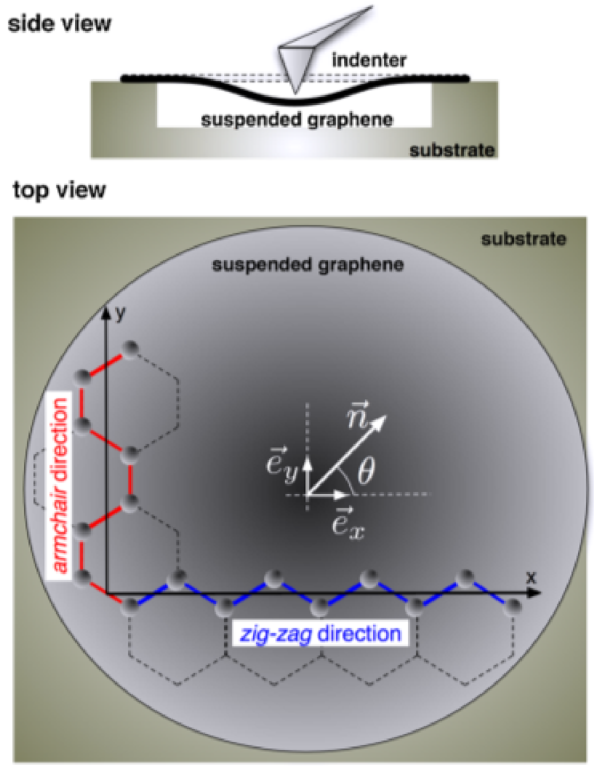

Figure 2.1: (Side view) Uniaxial strain is generated through indentation in suspended graphene, (top view) shows the reference system where ZZ and AC direction are specified. Figure took from ref. [108].

9, tetragonal 6, rhombohedral 6, hexagonal 5, and cubic 3. The most simple system is a linear and isotropic material with two elastic modulus, having a linear constitutive equation given by

$$\begin{aligned} \sigma &= \frac{Y}{1+\nu}\mathbf{u} + \frac{\nu Y}{(1+\nu)(1-2\nu)}\mathbb{I}\ \mathrm{Tr}(\mathbf{u}) \\ &= 2\mu\mathbf{u} + \lambda\mathbb{I}\ \mathrm{Tr}(\mathbf{u}), \end{aligned} \tag{2.11}$$

where Y and ν are Young modulus and Poisson's ratio, respectively. The Hooke's law (2.11) can be also expressed in terms of the Lamé coefficients μ and λ and they related with the Young modulus and Poisson ratio as $\mu = \frac{Y}{2(1+\nu)}$ and $\lambda = \frac{\nu Y}{(1+\nu)(1-2\nu)}$ for three-dimensional systems and $\mu = \frac{Y}{2(1+\nu)}$ and $\lambda = \frac{\nu Y}{(1-\nu^2)}$ for the two-dimensional case [135].

In the case of nonlinear anisotropic two-dimensional materials, such as graphene [9, 107, 108], a strain energy density to third order describes perfectly its nonlinear elastic behavior which

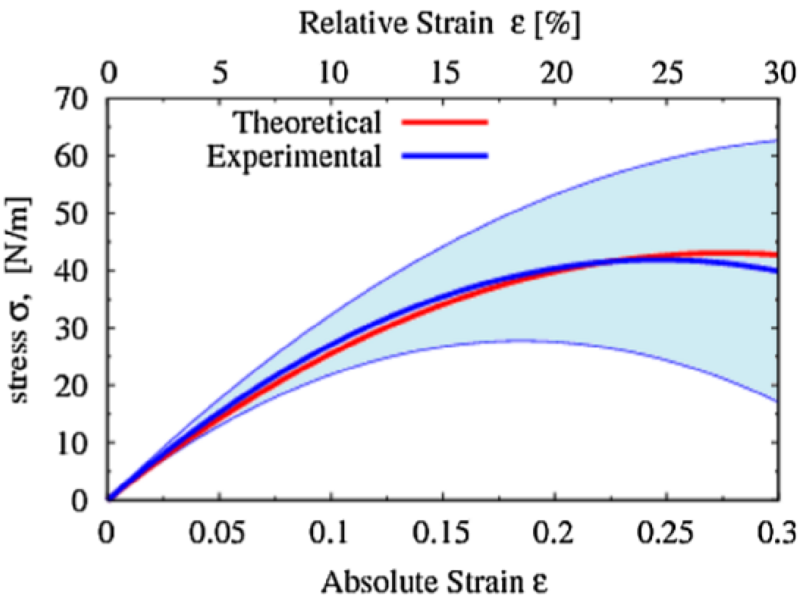

Figure 2.2: Theoretical and experimental comparison of the stress-strain curves of graphene. The blue region corresponds to experimental data error. This figure was taken from ref. [108].

can be written as [107]

$$U(\mathbf{u}) = \frac{\lambda}{2}\mathrm{Tr}(\mathbf{u})^2 + \mu\mathrm{Tr}(\mathbf{u^2}) + \Lambda_1(u_{xx}-u_{yy})[(u_{xx}-u_{yy})^2 - 12u_{xy}^2] \\ + \frac{1}{2}\Lambda_2\mathrm{Tr}(\mathbf{u})[2\mathrm{Tr}(\mathbf{u^2}) - \mathrm{Tr}(\mathbf{u})^2] + \frac{1}{2}\Lambda_3\mathrm{Tr}(\mathbf{u})^3, \quad (2.12)$$

where Λ_j with $j = 1, 2$ and 3 are nonlinear elastic modulus defined in [136]. Note that when the linear region is only considered ($\Lambda_1 = \Lambda_2 = \Lambda_3 = 0$), the strain energy function (2.12) describes isotropic systems with linear elastic modulus μ and λ or their equivalents Y and ν. In the nonlinear elastic regime, the system is fully isotropic when $\Lambda_1 = 0$ in (2.12). These linear and nonlinear elastic constants modulus have been calculated from DFT and TB calculations for uniaxially strained graphene with the values of $Y = 312$ Nm^{-1}, which has a good agreement with the experimental value [9]. The value of ν is estimated between 0.1-0.17 and the nonlinear modulus have the values $\Lambda_1 = -16.8$, $\Lambda_2 = -250.9$ and $\Lambda_3 = -278.6$ in units Nm^{-1} [137, 138, 139]. A direct comparison between theoretical predictions and experimental data was performed for graphene subjected to uniaxial tension along $\hat{n} = (\cos\theta, \sin\theta)$ using a nanoindentation mechanism, shown in Fig. 2.1. The stress-strain relationship in (2.12) is simplified to [108]

$$\sigma = Y\mathbf{u} + D(\theta)\mathbf{u}^2, \tag{2.13}$$

where $D(\theta)$ is the effective two-dimensional nonlinear modulus

$$D(\theta) = \frac{3}{2}(1-\nu)^3\Lambda_3 + \frac{3}{2}(1-\nu)(1+\nu)^2\Lambda_2 + 3(2\cos^2\theta - 1)(16\cos^4\theta - 16\cos^2\theta + 1)(1+\nu)^3\Lambda_1. \tag{2.14}$$

Theoretical and experimental stress-strain curves are shown in Fig. 2.2 [9, 108], finding a good agreement between them. The failure stress can be calculated from (2.13) obtaining the value of 42.4 Nm^{-1} very near to the experimental value 42 ± 4 Nm^{-1}. This represents the highest failure stress value registered so far of a material in the nature [9].

2.2 Tight-Binding method

Tight-Binding is a method frequently used in the study of electronic band structure of molecules and crystals whose electron energy is very near to the atomic orbital energy. This method is based in the linear combination of atomic orbitals and in the mean-field approximation. In crystals, the atomic orbital is expanded in according with the Bloch's theorem for each atom of the unitary cell. These wavefunctions are evaluated in the Schrödinger equation leading to a secular equation. Since the interaction potencial is usually unknown, the related integrals and the overlap terms are taken as adjustable parameters. They can be found with other numerical methods or from experimental data available [140]. The electronic band structure is obtained solving the secular equation. The following development shows the use of TB method in crystals and in particular for anisotropic graphene. In general, the wavefunction of a crystal using the Bloch theorem can be written as

$$\begin{aligned} |\Phi_k\rangle &= \sum_{m=1}^{n} a_m(\vec{k})|\Phi_k^{(m)}\rangle && (2.15)\\ &= \sum_{m=1}^{n}\sum_{\vec{R}_l}^{N} a_m(\vec{k})\mathrm{e}^{i\vec{k}\cdot\vec{R}_l}|m, \vec{r} + \vec{\delta}_m - \vec{R}_l\rangle, && (2.16) \end{aligned}$$

where $a_m(\vec{k})$ with $m = 1, \ldots, n$ are n complex functions of the $\vec{k}$ wavevector corresponding to the n atoms of the unitary cell. The second sumatory corresponds to the Bloch expansion of each atomic orbital $|\Phi_k^{(m)}\rangle = |m, \vec{r} + \vec{\delta}_m - \vec{R}_l\rangle$ with N unitary cells in the crystal. $\vec{R}_l$ indicates the sites at the Bravais lattice and $\vec{\delta}_m$ is the vector that connects the sites of the underlying Bravais lattice with the site of the m atoms, within the unitary cell.

Using the Schrödinger equation $H|\Phi_k\rangle = E_k|\Phi_k\rangle$, we arrive to the following secular equation

$$\det[\mathbf{H}_k - E_k^\lambda \mathbf{S}_k] = 0, \tag{2.17}$$

where $\mathbf{H}_k$ and $\mathbf{S}_k$ are the hamiltonian and overlap matrix whose entries are $H_k^{ij} = \langle\Phi_k^{(i)}|H|\Phi_k^{(j)}\rangle$ and $S_k^{ij} = \langle\Phi_k^{(i)}|\Phi_k^{(j)}\rangle$, respectively and $E^{(j)}$ is the orbital atomic energy. The λ label denotes the n-energy bands. The hamiltonian and overlap matrix elements can be evaluated taking into account that the hamiltonian is separated in two terms $H = H_o + U$, with H_o the atomic hamiltonian and U the perturbative electrostatic potential considering the mean-field approximation. Hence, with $H_o|j, \vec{r} + \vec{\delta}_j - \vec{R}_l\rangle = E^{(j)}|j, \vec{r} + \vec{\delta}_j - \vec{R}_l\rangle$, the hopping matrix has the elements

$$t_k^{ij} = \sum_{\vec{R}_l}^{N} \mathrm{e}^{i\vec{k}\cdot\vec{R}_l}\langle i, \vec{r}|U|j, \vec{r} + \vec{\delta}_{ij} - \vec{R}_l\rangle \tag{2.18}$$

and the reduced overlap matrix with the entries

$$s_k^{ij} = \frac{S_k^{ij}}{N} = \sum_{\vec{R}_l}^{N} \mathrm{e}^{i\vec{k}\cdot\vec{R}_l}\langle i, \vec{r}|j, \vec{r} + \vec{\delta}_{ij} - \vec{R}_l\rangle. \tag{2.19}$$

Using (2.18) and (2.19), a more simplified version of (2.17) with $\det[t_k^{ij} - (E_k^\lambda - E^{(j)})s_k^{ij}] = 0$ is obtained. In the case of identical atomic orbitals $E^{(j)} = E$, the E constant can be omitted since it only represents a shift of the energy bands. For two atomic orbitals in the unitary cell, the energy bands can be calculated directly

$$E^\lambda(\vec{k}) = \frac{f_1(\vec{k}) + \lambda\sqrt{f_1^2(\vec{k}) + f_2(\vec{k})f_3(\vec{k})}}{f_2(\vec{k})}, \tag{2.20}$$

where $\lambda = 1$ (-1) denotes the conduction (valence) band and the three functions $f_i(\vec{k})$ are defined as $f_1(\vec{k}) = s_{11}(\vec{k})t_{11}(\vec{k}) - \mathrm{Re}\{s_{12}(\vec{k})t_{12}^*(\vec{k})\}$, $f_2(\vec{k}) = s_{11}^2(\vec{k}) - |s_{12}(\vec{k})|^2$ and $f_3(\vec{k}) = |t_{12}(\vec{k})|^2 - t_{11}^2(\vec{k})$. The expressions (2.18), (2.19) and (2.20) are useful in the description of anisotropic graphene.

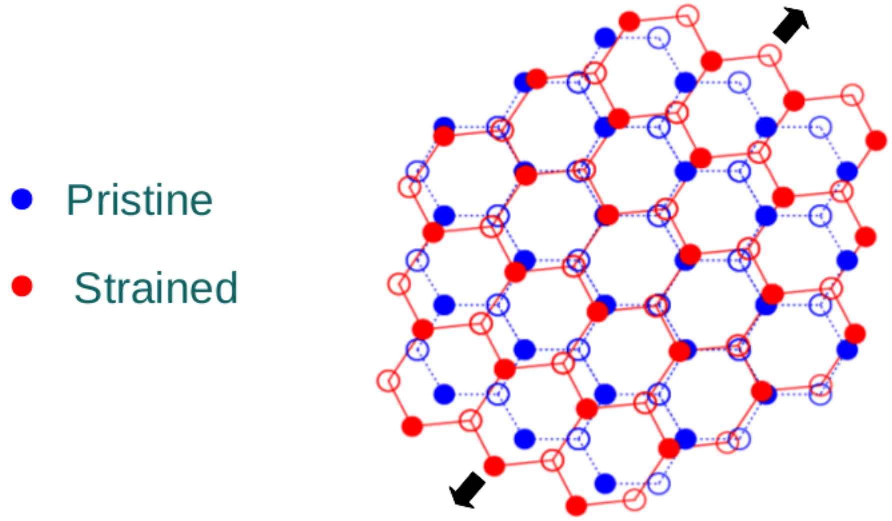

Figure 2.3: Pictorial representation of a deformed hexagonal lattice (red) with respect to one unstrained (blue). Open and closed circles denote the traingular sublattices A and B, respectively. Figure took from ref. [37].

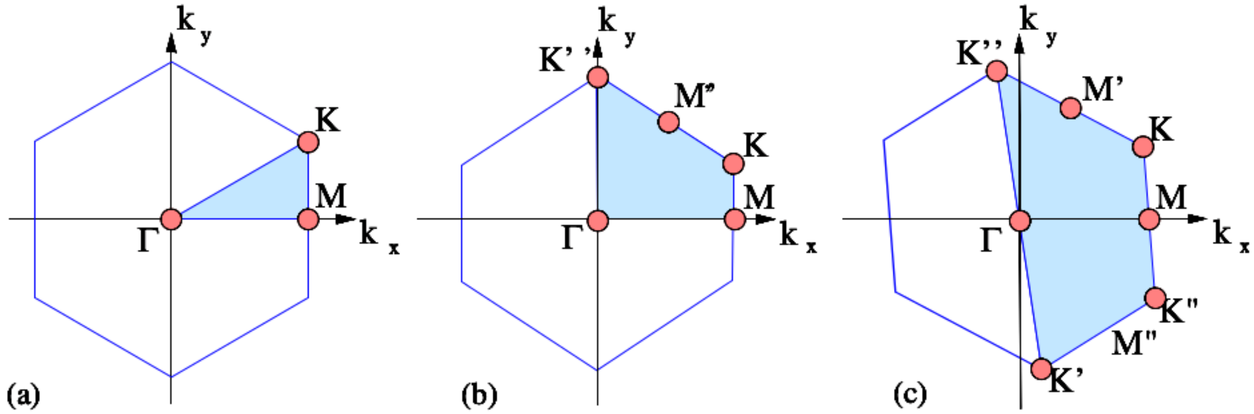

Figure 2.4: The first Brillouin zone for (a) hexagonal lattice, (b) deformed hexagonal lattice with rhombic symmetry and (c) deformed hexagonal lattice with monoclinic symmetry. The blue shadded areas represent the irreducible zones. Figure took from ref. [45].

2.2.1 Tight-Binding description of anisotropic graphene

The anisotropic graphene model consists in a two-dimensional graphene sheet presenting different bond lengths, hopping and overlapping parameters among nearest carbon atoms, which can be induced by mechanical strain. The crystal is conformed by two deformed triangular Bravais sublattices identified as A and B, as shown in Fig. 2.3 for the case of strained graphene. The unitary cell has two carbon atoms where a decoupling between p_z and σ orbitals can be considered due to the sp^2 hybridization. The lattice vectors $\vec{a}_1$ and $\vec{a}_2$ correspond the reciprocal lattice vectors $\vec{b}_1 = (2\pi/A_c)\vec{a}_2 \times \hat{z}$ and $\vec{b}_2 = (2\pi/A_c)\hat{z} \times \vec{a}_1$, where both lattices are geometrically deformed hexagonal meshes. Thus, the first Brillouin zone is a distorted hexagon with high symmetry points K and K', as shown in Fig. 2.4. In this TB of anisotropic graphene, the underlying sublattice is A and the positions of the nearest neighbors are given by $\vec{\delta}_1$, $\vec{\delta}_2$ and $\vec{\delta}_3$. The parameters $\{s_i^{(0)}, t_i^{(0)}\}$ and $\{s_i^{(1)}, t_i^{(1)}\}$ with $i = 1, 2$ and 3 are denoted for nearest and next nearest neighbors respectively. The quantities $s_i^{(0)} = \langle \phi_{p_z}(\vec{r}) | \phi_{p_z}(\vec{r} - \vec{\delta}_i) \rangle$ indicate the overlap value between the p_z orbital in the carbon atom of the sublattice A and its corresponding nearest neighbor of the sublattice B located at $\vec{\delta}_i$, and $t_i^{(0)} = \langle \phi_{p_z}(\vec{r}) | U | \phi_{p_z}(\vec{r} - \vec{\delta}_i) \rangle$ are the hopping values corresponding to the probability amplitudes that an electron passes to one of the three nearest atoms. In this way, $s_i^{(1)}$ and $t_i^{(1)}$ have similar meaning and expression for next nearest neighbors. Therefore, the sumatories t_k^{ij} and s_k^{ij} given by (2.18) and (2.19) are truncated until next nearest neighbors. One obtains for the $f_k^{(j)}$ with $j = 1, 2$ and 3 of the equation (2.20) the following expresions

$$\begin{aligned} f_1(\vec{k}) &= (1 + h_p(\vec{k}))h_q(\vec{k}) - g_p(\vec{k}) \\ f_2(\vec{k}) &= (1 + h_p(\vec{k}))^2 - g_r(\vec{k}) \\ f_3(\vec{k}) &= g_q(\vec{k}) - h_q^2(\vec{k}), \end{aligned}$$

where the following quantities are defined as $g_\eta(\vec{k}) = \sum_{i,j=1}^{3} \xi_\eta^{ij} \cos\theta_{ij}(\vec{k})$ with $\eta = p, q, r$ and $\theta_{ij}(\vec{k}) = \vec{k} \cdot (\vec{\delta}_i - \vec{\delta}_j)$ being $\xi_p^{ij} = s_i^{(0)} t_j^{(0)}$, $\xi_q^{ij} = t_i^{(0)} t_j^{(0)}$ and $\xi_r^{ij} = s_i^{(0)} s_j^{(0)}$. The $h_\eta(\vec{k})$ functions are expressed as $h_\eta(\vec{k}) = \xi_\eta^{(1)} \cos\theta_{12}(\vec{k}) + \xi_\eta^{(2)} \cos\theta_{13}(\vec{k}) + \xi_\eta^{(3)} \cos\theta_{23}(\vec{k})$ with $\xi_p^{(i)} = s_i^{(1)}$ and $\xi_q^{(i)} = t_i^{(1)}$. Generally, the overlap terms are always neglected because the electronic density of the p_z orbital decays quickly with the distance in graphene. For a separation among atoms that are of the order of 1 Å roughly, the overlap is expected to be vanished. Therefore, the initial twelve parameters in the TB calculation are reduced to six hopping parameters: three to nearest neighbors and other three to next nearest neighbors. Hence, the dispersion relation

(2.20) can be written as

$$E^{\lambda}(\vec{k}) = h_q(\vec{k}) + \lambda\sqrt{g_q(\vec{k})}, \tag{2.21}$$

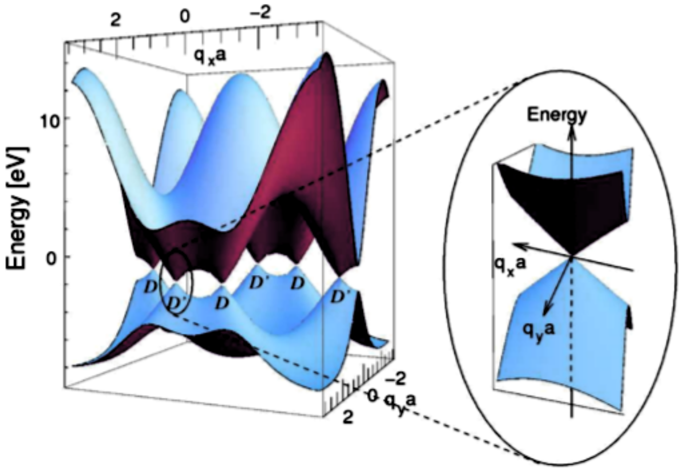

Figure 2.5: Energy band structure of anisotropy graphene that can be obtained from equation (2.21). Zoom shows a Dirac cone for low energy regime. This plot was obtained for graphene with quinoid-type deformation, in ref. [24].

the plot of this dispersion relation is shown in Fig. 2.5 for quinoid-type deformed honeycomb lattice [24] using specific values of $t_i^{(0)}$ and $t_i^{(1)}$, that throughout the text, will be denoted as t_i and t_i', respectively. Each carbon atom contributes with one electron of the p_z orbital, therefore the valence band ($\lambda = -1$) is completely filled while the conduction band ($\lambda = +1$) is completely empty. Both bands are symmetrical in absence of the overlap terms and hopping parameters to next nearest neighbors. It is also noted that there are contact points between them, which are called Dirac points. Such points appear in pairs due to the time reversal symmetry $E^{\lambda}(-\vec{k}) = E^{\lambda}(\vec{k})$. The Dirac points are located at the $\vec{K}$ points and they are obtained when $\sum_{j=1}^{3} t_j \mathrm{e}^{i\vec{K}\cdot\vec{\delta}_j} = 0$. The solutions for this expression are given by

$$\cos[\vec{K}.(\vec{\delta}_i - \vec{\delta}_j)] = \frac{t_l^2 - t_i^2 - t_j^2}{2t_i t_j}, \tag{2.22}$$

with $i \neq j \neq l$ and having validity in the region defined by the triangle inequality

$$|t_i - t_j| \leq t_l \leq t_i + t_j, \tag{2.23}$$

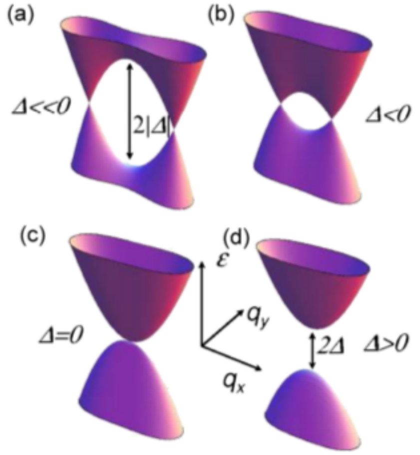

Figure 2.6: Topological phase transition illustrated through the low energy band structure. Figure took from ref. [24].

which is obtained straightforwardly from Dirac points equation $\sum_{j=1}^{3} t_j \mathrm{e}^{i\vec{K}\cdot\vec{\delta}_j} = 0$. The inequality (2.6) establishes a topological region where there are Dirac points. Tuning the hopping parameters is possible to annihilate a pair of opposite Dirac points, and in consequence, a gap opening in graphene emerges due to the merging of Dirac points. The evolution of the energy bands of this Topological Phase Transition (TPT) are shown in Fig. 2.6. Such TPT could be obtained, modulating the hopping parameters with the modification of the bond lengths among atoms under strain. Indeed, the bridge that connects the hopping parameters with the bond lengths is through a scaling rule. The Papaconstantopoulus' scaling rule [76] is the most frequently used in graphene, which relates the hopping parameter t_i with the δ_i bond lengths through a exponential decay

$$t_i = t_o \mathrm{e}^{-\beta(\delta_i/a-1)}, \tag{2.24}$$

where $t_o = 2.71$ eV is the value of the hopping parameter and $a = 1.42$ Å is the bond length for pristine graphene [126]. The constant β known as the Grüneisen parameter has the value of $\beta = 3.37$ [126]. Other relations between hopping parameters and bond lengths have been proposed, such as the Harrison's scaling rule [117] establishing that the hopping is inversely proportional to the squared of the bond length, ie $t_i = t_o(a/\delta_i)^2$. Although the value of the hopping parameter is dependent of the bond length, its relation with strain can be established using the deformed bond length calculated from the elasticity theory of two-dimensional structures.

Chapter 3

Geometrical Approach for Anisotropic Dirac Materials

In previous chapters, we showed the most common routes for the study of strained graphene properties which can be also applied in the study of other anisotropic Dirac materials [141]. Using TB approach and elasticity theory, the electronic band structure shows interesting aspects that were embodied in several effective models from different assumptions [13, 15, 24, 38, 98, 130]. Whereas other authors prefered to study the electronic properties using DFT calculations [45, 46, 60, 62, 66, 67], corroborating a qualitative physical description given by TB predictions. However, it was also noted that there is a non-negligible quantitative difference between these two methodologies [67], being attributable to the serie of approximations carried out in the proposed models, reducing their validity range [15, 38, 68, 98, 130].

All mentioned effective models overlooked the nonlinear elastic behavior of graphene, which has been evidenced both theoretical and experimentally [9, 38, 108]. Further, the indefiniteness of the group velocity at Dirac point remains unsolved. Furthermore, the effect of deformation on the atomic distances is only taken into account through the scaling of the hopping parameters in the TB approach [11, 15, 47, 83, 98], with some exceptions [24, 38, 68]. Such a hopping renormalization is commonly modeled with an exponential decay [76] or using the Harrison's scaling rule $V_{pp\pi} \propto 1/l^2$ [117]. Nevertheless, these renormalizations could fail beyond the linear elastic regime, since the Poisson ratio changes for uniaxial strain. Indeed, they could have a different dependence for each strain-type considered, as was probed in a comparative work on

TB approach and DFT calculations for uniaxially strained graphene [60]. Other point that has been overlooked is the relaxation of atomic positions, which should be present in a more realistic calculation. Therefore, an accurate and precise way to obtain the hopping parameters in strained graphene is to fit energy bands of a TB approach with the ones obtained from DFT calculations or from experimental data [60].

To include the above observations imply to add a huge amount of terms in the QFTCS in addition to the fourteen existing terms mentioned by Ramezani *et al.*. Since the hamiltonian of the QFTCS was expanded around the high symmetry point, the linear dispersion relation is not guaranteed, being necessary the inclusion of high order terms in the linear momentum. Therefore, the QFTCS would have a hamiltonian constructed by too many terms, becoming impractical. Thus, a better alternative is to develop a continuum model with an effective hamiltonian expanded around the Dirac points.

On this line, some authors have proposed a generalized Weyl hamiltonian [68], whose parameters are the effective tilt and anisotropic velocities, where the velocities can be expressed in terms of the hopping parameters. This proposal allows to describe the effect of tilt and anisotropy of the Dirac cone on the physical properties of graphene in the low energy regime. Nevertheless, the absence of an intrisic rotation of the Dirac cone makes that the model becomes only applicable to graphene and Dirac-like systems with quinoid-type deformation, such as uniaxially strained graphene along AC and ZZ directions, where two hopping parameters are equals and one is different. Such model is frequently applied in other systems having similar features that graphene, but with a more notable Dirac cone tilt, as some organic compounds [26], VO_2/TiO_2 heterostructures [112] and cold atoms in optical lattices [16, 33, 111]. On the other hand, some authors enhanced and generalized previous effective models used for uniaxial strain in graphene around the Dirac points [11, 72, 98]. They included the effect of the angular distortion of the lattice vectors, caused by uniform strain on the Bloch expansion in the TB method [38, 130, 131, 132]. These works fall into the comments about the lack of nonlinear elasticity [9, 60, 108], relaxation of atomic positions effects, and the indefiniteness of group velocity at the Dirac point. Then, the proposition of a more general and versatile approach in order to study other anisotropic Dirac materials is needed.

Instead of a hopping scaling rule frequently used in effective models around the Dirac point, an alternative way is proposed in the present thesis. We propose a continuum approach for the study of massless Dirac fermions (MDF) dynamics and physical properties of Dirac materials which are subjected to an anisotropy induction mechanism (AIM). This allows to generalize the strain-engineering ideas to two general concepts: anisotropy and inhomogeneity. Anisotropy can be caused by loads upon the material [107], chemical manipulation [32], periodic potentials [142] or a rearrangement at system configuration [33]. Inhomogeneity arises when the AIM is position dependent. Initially, we consider the homogeneous anisotropy in the present continuum model applying a canonical transformation on the linear momentum. In this way, the indeterminacy of the group velocity at Dirac point is solved and allows to define the concept of effective Fermi velocity. Further, the transformation matrix elements can be calculated from a TB approach, fitting the energy bands obtained from DFT or through experimental data available. Since these matrix elements are related with the geometrical parameters of the Dirac cone, the proposed model is called Geometrical Approach (GA), which provides a direct way to link physical properties with Dirac cone parameters. Later, a position dependent transformation on the linear momentum is proposed demanding the hermiticity and the symplectic condition. Thus, complex gauge fields and effective Fermi velocity as a function of transformation matrix elements were found. This model was used for study the effective Fermi velocity, the expansion and contraction of the LLs, and the electron quantum optics in homogeneously strained graphene. In the present chapter, we show general results of effective Fermi velocity, physical properties and electron optics for anisotropic Dirac materials.

3.1 Anisotropy and inhomogeneity in massless Dirac fermions

Theoretically, a homogeneous anisotropy description can be given from a 2 × 2 Fermi velocity tensor v_{ij}, which replaces the Dirac hamiltonian $H = v_F \vec{\sigma} \cdot \vec{p}$ by a 2D generalized Weyl-like hamiltonian $H_W = v_{ij}\sigma_i p_j$ [24], where v_F is the Fermi velocity at initial configuration system, and $\vec{\sigma}$ are the Pauli matrices acting on the pseudospin space. We propose a linear transformation on the linear momentum which maps the Dirac hamiltonian to a 2D Weyl hamiltonian

$$\vec{p}\,' = A\vec{p}, \tag{3.1}$$

where A is a 2×2 anisotropy matrix with real entries a_{ij}. We note that the Fermi velocity tensor is restored in terms of the elements matrix $v_{ij} = v_F a_{ij}$. Therefore, the Weyl-like hamiltonian H_W and the mapped hamiltonian $H(\vec{p}\,') = v_F\vec{\sigma}\cdot\vec{p}\,'$ by the transformation (3.1) are the same, as shown in appendix A1. Nevertheless, it is known that the dispersion relation of H_W has an elliptical shape in the momentum space as shown in Fig. 3.1 (a), and a group velocity calculation at the Dirac point results undefined. Such problem is solved with a suitable change of the linear momentum $\vec{p}\,'$, building a transformation for $\vec{p}$ which satisfies the symmplectic (anti symplectic) group condition. In general, the transformation (3.1) does not necessarily satisfy the symplectic $M^TJM = J$ or anti symplectic $M^TJM = -J$ condition, where M is the Jacobian matrix, M^T its transpose and J a 2×2 matrix having elements defined as $j_{11} = j_{22} = 0$ and $j_{12} = -j_{21} = 1$. However, we can convert any anisotropy transformation A (except the one-dimensional case, $\det A = 0$), in a symplectic ($\det A > 0$) or anti symplectic ($\det A < 0$) transformation defining $S = \xi^{-1}A$, with $\xi = \sqrt{|\det A|}$, (see appendix A2). Thereby, the anisotropic $\vec{p}\,'$ and the original $\vec{p}$ are related with the new linear momentum

$$\vec{p}_c = S\vec{p} = \xi^{-1}\vec{p}\,', \tag{3.2}$$

where $\vec{p}_c$ has the same role that the conjugated linear momentum for symplectic transformations, because the commutation relations $[x_i, p_j]$ with $i, j = x, y$, do not change whether we transform the position operator as $\vec{r}_c = (S^{-1})^T\vec{r}$, where $\vec{r}$ is the position operator for the initial configuration and $\vec{r}_c$ is the new conjugated position vector, as shown in appendix A3. Thus, when we express the mapped hamiltonian $H(\vec{p}\,')$ in terms of $\vec{p}_c$ using (3.2), an effective Dirac-like hamiltonian for anisotropic systems is restored

$$H(\vec{p}_c) = v_F'\vec{\sigma}\cdot\vec{p}_c. \tag{3.3}$$

In this point, we emphasize that the introduction of the canonical linear momentum $\vec{p}_c$, instead of $\vec{p}$, does not imply other succesive transformation in the mapped hamiltonian $H(\vec{p}\,')$, since we only have performed the substitution $\vec{p}\,' = \xi\vec{p}_c$. Hence, the hamiltonian (3.3) describes the same anisotropic dynamics system than $H(\vec{p}\,')$ or H_W with a constant effective Fermi velocity v_F', which is extracted directly from the anisotropy matrix

$$v_F' = v_F\sqrt{|\mathrm{det}A|}, \tag{3.4}$$

whose value is the same for all energy surface points in the scaled p_c-momentum space. Therefore, the indefiniteness of the group velocity calculation at Dirac point is solved, being v_F' its value. Further, the expressions (3.3) and (3.4) provide a considerable reduction in the description of the anisotropic system. We observe that there is one parameter v_F' instead of four parameters given by the Fermi velocity tensor v_{ij}. Since most of the Dirac material properties is encoded on the Fermi velocity, its modulation produces changes in all the v_F-dependent physical quantities. Thereby, the information about the tuning of the electronic, vibrational and transport properties of the system under an AIM are obtained through the anisotropy matrix determinant.

Several physical properties have been studied in anisotropic Dirac materials using the 2D Weyl hamiltonian, whose dependency with the effective Fermi velocity is identified. For instance, Landau levels in pristine graphene have a linear dependency with v_F [3, 55], being $E_N = \mathrm{sgn}(N)v_F\sqrt{2|N|}/l_B$ where $N = 0, \pm1, \pm2, \ldots$ are the Landau level indexes and l_B the magnetic length. Strained graphene, as a particular case of an anisotropic MDF, has a Landau level spectrum written as $E_N' = \mathrm{sgn}(N)v_F'\sqrt{2|N|}/l_B$ [24, 67], which can be directly obtained with the simple substitution $v_F \to v_F'$. The substitution is fully justified by the exposed arguments about the effective Dirac hamiltonian (3.3). Accordingly, the Landau levels spectra is tuned linearly by the AIM through the effective Fermi velocity. Charge compressibility in pristine [75] and strained graphene [72] was given by $\kappa = 2/(n\hbar v_F\sqrt{n\pi})$ and $\kappa' = 2/(n\hbar v_F'\sqrt{n\pi})$ having an inverse proportional dependency with v_F', where n is the electron density. Paramagnetic spin susceptibility and Coulomb interaction ratio also depend of v_F^{-1} [50, 143], whereas the heat capacity and diagmagnetic spin susceptibility are v_F^{-2} dependent [50]. These physical observables are shown in Fig. 3.1 (b) as a function of v_F'/v_F. Nevertheless, we must consider that the AIM could also affect other different quantities to v_F', such as lengths and areas of the system, showing an extra modulation in some physical observables. For example, density of states (DOS) has the form $\rho(E) = 4a_cE/(\pi\hbar v_F^2)$, where a_c is the unit cell area for the initial configuration. Now,

(a) Anisotropy transformation

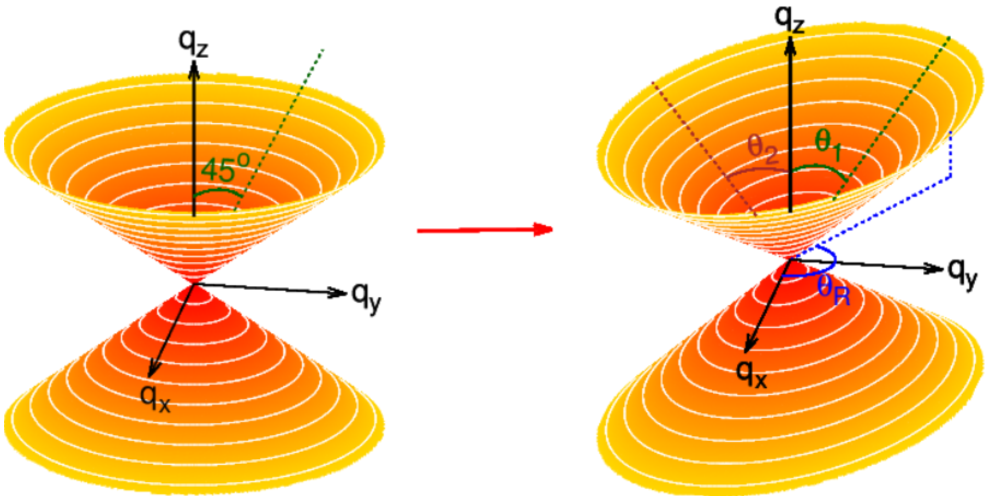

(b) Physical observables (c) Fermi velocity

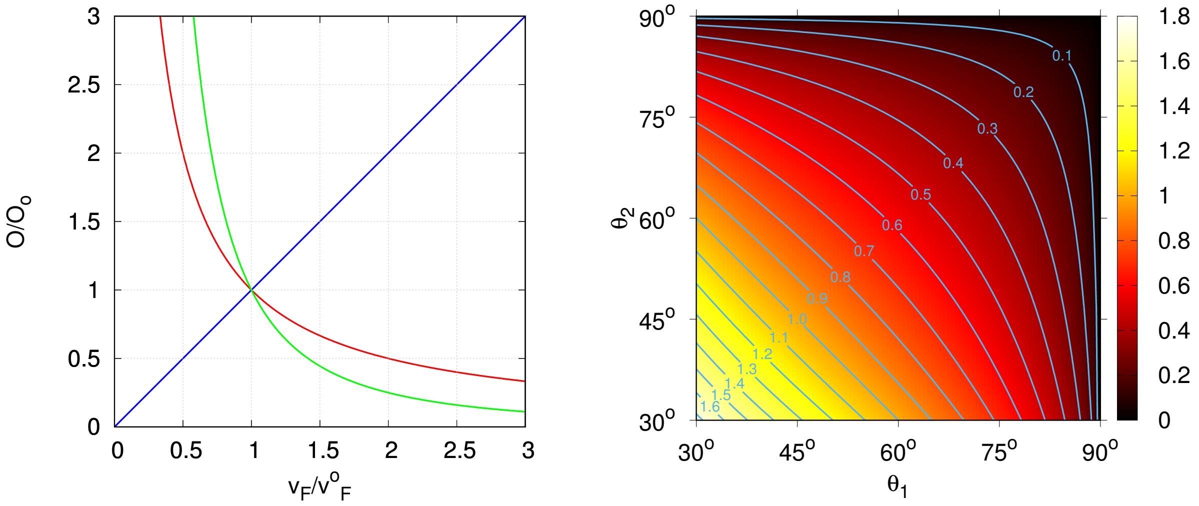

Figure 3.1: Geometrical relation of physical quantities through the Fermi velocity. (a) Illustration of the anisotropy transformation (3.1), which maps a circular Dirac cone to one elliptical. (b) With the GA can be proved that the physical observables directly depends of the effective Fermi velocity. Thus, observables as the LLs change linearly with v_F (blue), while charge compressibility and heat capacity vary according to v_F^{-1} (red) and v_F^{-2} (green), respectively. (c) Effective Fermi velocity as a function of the extremal elliptical cone angles θ_1 and θ_2.

if the AIM modifies the unit cell area, the DOS becomes $\rho'(E) = 4a'_c E/(\pi\hbar v'^2_F)$ with a'_c the unit cell for the anisotropic Dirac system. Then, a correct experimental estimation of v'_F from DOS measurements must consider both changes; in the effective Fermi velocity and in the unit cell area.

So far, the anisotropy matrix elements a_{ij} are seen as lacking of a direct physical and geometrical meaning. However, these elements have an illuminating relation with geometrical and physical quantities. It is possible to show that the anisotropy matrix A can be decomposed in three succesive linear transformations, (see appendix A4)

$$A = R(-\alpha)D(\lambda_1, \lambda_2)R(\theta_R), \tag{3.5}$$

where $R(\theta_R)$ is the 2×2 rotation matrix acting on the p-momentum space with a rotation angle θ_R around the perpendicular axis to the plane (p_x, p_y). $D(\lambda_1, \lambda_2)$ is a diagonal matrix which scales the rotated axes by the amounts λ_1 and λ_2. $R(-\alpha)$ is an extra rotation matrix which results of the rotation of $\vec{\sigma}$ by an angle α around the z-axis from the unitary transformation $\vec{\sigma} = U^\dagger(\alpha)\vec{\sigma}_0 U(\alpha)$, with $U(\alpha)$ the rotation operator. This anisotropy matrix decomposition reveals a direct dependence of the effective Fermi velocity with the scaling parameters λ_1 and λ_2 to be

$$v'_F = v_F\sqrt{|\lambda_1||\lambda_2|} = \sqrt{|\cot\theta_1 \cot\theta_2|}. \tag{3.6}$$

Therefore, a homogeneous spatial distortion of the system caused by the AIM, modifies the effective Fermi velocity regardless the involved rotations. Further, when we use the decomposition (3.5) in the calculation of p', we obtain

$$p' = p\sqrt{\lambda_1^2\cos^2(\theta - \theta_R) + \lambda_2^2\sin^2(\theta - \theta_R)}, \tag{3.7}$$

where p_x and p_y were expressed in terms of polar coordinates: $p_x = p\cos\theta$ and $p_y = p\sin\theta$. Thus, θ_R is also recognized as the rotation angle of the elliptical Dirac cone, where the dispersion relation is written as $E = sv_F p'$ with $s = 1$ (-1) denoting the conduction (valence) band. The scale factors λ_1 and λ_2 are related with the extremal elliptical cone angles θ_1 and θ_2 as $\lambda_1 = \cot\theta_1$ and $\lambda_2 = \cot\theta_2$. Hence, a link between the anisotropic Dirac material properties with the Dirac cone geometry through the effective Fermi velocity $v'_F = v_F\sqrt{|\cot\theta_1||\cot\theta_2|}$ is established. This velocity can be increased (decreased) when θ_1 or θ_2 decrease (increase), as shown in Fig. 3.1 (c). On the other hand, the geometrical parameters also can be related with the hopping parameters of a Tight-Binding approach, fitting the energy bands obtained from DFT calculations or through experimental data available.

We observe that the role of spin rotation $R(-\alpha)$ does not modify the dispersion relation neither the effective Fermi velocity. However, the influence of the pseudospin rotation is evidenced in the eigenstates $|\Psi(\vec{p})\rangle = \frac{1}{\sqrt{2}}(1, s e^{i\phi})$ of the Weyl-like hamiltonian, where $\phi = \arctan(p'_y/p'_x)$ is the pseudospin angle. Thereby, when we set the anisotropic transformations (3.1) with the values of $\alpha = -\pi/2$, $\lambda_1 = \lambda_2 = 1$ and $\theta_R = 0$, the isotropic Dirac hamiltonian $H(\vec{p})$ is mapped to a Rashba hamiltonian $H_R = v_F(\vec{\sigma} \times \vec{p}) \cdot \hat{z}$ where the spinor has a chiral angle $\phi = \arctan(-p_x/p_y)$. This hamiltonian is frequently found in the description of electron dynamics in the surface of a 3D topological insulator and $d-$wave superconductors [21]. Therefore, the anisotropic Dirac hamiltonian (3.3) also describes the MDF dynamics in those systems.

In order to extend the MDF dynamics for inhomogeneous and anistropic Dirac materials, we generalize the anisotropy transformation (3.1) to be spatially dependent. Such transformation must convert a Dirac hamiltonian $H(\vec{p})$ to one of the form $H(\vec{r}, \vec{p}\,')$, preserving its hermiticity. A proposal satisfying these requirements is written as

$$\vec{p}\,' = \frac{1}{2}\Lambda(\vec{r})\vec{p} + \frac{1}{2}(\Lambda(\vec{r})\vec{p})^{\dagger} \tag{3.8}$$

where $\Lambda(\vec{r})$ is a 2×2 matrix with complex elements $\lambda_{ij}(\vec{r})$ having an explicit spatial dependency. Clearly, $\vec{p}\,' = \vec{p}\,'^{\dagger}$ sastisfies the hermiticity condition. Likewise, applying the transformation (3.8) over the isotropic and homogeneous hamiltonian $H(\vec{p})$, the mapped hamiltonian $H(\vec{p}\,')$ is also hermitian, (see appendix A5). More importantly, if the matrix elements $\lambda_{ij}(\vec{r})$ are constants we recover the anisotropy homogeneous transformation (3.1) where $A = \Lambda_R = \text{Re}\{\Lambda\}$, (see appendix A5). Thus, $\Lambda(\vec{r})$ is a natural generalization of the anisotropy matrix A for inhomogeneous cases. Moreover, the transformation (3.8) has a suggestive physical meaning when we use the commutator $[\lambda_{ij}(\vec{r}), p_k] = i\hbar\partial_k\lambda_{ij}(\vec{r})$ obtaining the expression

$$\vec{p}\,' = \Lambda_R(\vec{r})(\vec{p} + \vec{A}). \tag{3.9}$$

This relation resembles the minimal substitution in the electromagnetic theory with a complex pseudo vector potential $\vec{A} = \vec{A}_R + i\vec{A}_I = \Lambda_R^{-1}\vec{\omega}$, where $\vec{A}_R$ and $\vec{A}_I$ are the real and imaginary gauge fields, respectively (see apppendix A6). The components of $\vec{\omega}$ are given by $\omega_j = -\frac{i\hbar}{2}\partial_k\lambda^*_{jk}$ where the habitual notation indicates sum over repeated indices. We note that, decomposing $\Lambda(\vec{r})$ in its real $\Lambda_R(\vec{r})$ and imaginary $\Lambda_I(\vec{r})$ contributions in the expression of ω_j, the gauge fields $\vec{A}_R$ and $\vec{A}_I$ are mainly determined by $\Lambda_I(\vec{r})$ and $\Lambda_R(\vec{r})$, respectively. Thereby, the generation of a pseudomagnetic field can be linked to $\Lambda_I(\vec{r})$ and the pseudospin precession to $\Lambda_R(\vec{r})$. These embodied effects of the $\Lambda(\vec{r})$ transformation are the consequence of the spatial inhomogeneity in the system, the hermitian invariance and the noncommutativity of the position and the linear momentum, regardless of the used hamiltonian. In particular, we exemplify the transformation (3.9) on the Dirac-like hamiltonian H, and we found that the mapped hamiltonian is

$$H = v_F\vec{\sigma}\cdot\vec{p}\,' = v_F\vec{\sigma}\cdot\Lambda_R(\vec{r})(\vec{p}+\vec{A}) \tag{3.10}$$

having the same form that the hamiltonian proposed by other approaches [15, 78, 130], if we write the Fermi velocity tensor as $v_{ij} = v_F\lambda^R_{ij}$, the Dirac point shift $\vec{K}_D = -\vec{A}_R$, and the pseudospin precession term $\hbar v_F\vec{\sigma}\cdot\vec{\Gamma} = -iv_F\vec{\sigma}\cdot\Lambda_R(\vec{r})\vec{A}_I$, with an imaginary gauge field $\vec{\Gamma}$ given by the expression $\Gamma_j = \frac{i}{2v_F}\partial_k v_{jk} = \frac{i}{2}\partial_k\lambda^R_{jk}$, (see appendix A6). On the other hand, if we set the $\Lambda(\vec{r})$ transformation with $\lambda_{11}(\vec{r}) = a(\vec{r})$, $\lambda_{12}(\vec{r}) = -ib(\vec{r})$, $\lambda_{21}(\vec{r}) = ia(\vec{r})$ and $\lambda_{22}(\vec{r}) = b(\vec{r})$ as shown in appendix A7, the proposed hamiltonian and the motion equations in [67] are obtained, being $a(\vec{r})$ and $b(\vec{r})$ the dimensionless functions which scales the linear momentum. In the approaches [15, 78, 130], the appareance of a pseudo gauge field is attributed to the spatial dependency of the Dirac point shift, where the imaginary gauge field Γ guarantees the hermiticity of the hamiltonian. In the present work, we show that $\Lambda_I(\vec{r})$ directly leads to the emergence of a pseudo-vector potential $\vec{A}_R$, which preserves the hermiticity of the hamiltonian as much as the gauge field $\vec{A}_I$.

Likewise that for the homogeneous case, the group velocity in terms of $\vec{p}$ remains undefined at Dirac point. This problem is solved with the proposal of a canonical-like linear momentum $\vec{p}_c$, from a symplectic ($\det\Lambda_R > 0$) or anti symplectic ($\det\Lambda_R < 0$) transformation. The removal of the group velocity indeterminacy at Dirac point, leads to the generalization of a spatially dependent effective Fermi velocity. Without altering the hermiticity, the canonical-like linear momentum $\vec{p}_c$ is expressed as

$$\vec{p}_c = \frac{1}{2}\xi^{-1}(\vec{r})\Lambda(\vec{r})\vec{p} + \frac{1}{2}\left(\xi^{-1}(\vec{r})\Lambda(\vec{r})\vec{p}\right)^{\dagger}, \tag{3.11}$$

where the anisotropic and inhomogeneous linear momentum $\vec{p}\,'$ in (3.8) is related with $\vec{p_c}$ as $\vec{p}\,' = \xi(\vec{p_c} + \vec{\rho})$, being $\xi(\vec{r}) = \sqrt{|\det\Lambda_R(\vec{r})|}$ and $\vec{\rho}(\vec{r}) = \frac{i\hbar}{2}\Lambda^*\vec{\nabla}\xi^{-1}$ with $\Lambda^*(\vec{r})$ the conjugated of $\Lambda(\vec{r})$, (see appendix A8). Under this relation, the hamiltonian (3.10) has the form of an effective Dirac hamiltonian

$$H = v_F'(\vec{r})\vec{\sigma}\cdot(\vec{p_c} + \vec{\rho}), \tag{3.12}$$

and the effective Fermi velocity appears depending of the position as $v_F'(\vec{r}) = v_F\sqrt{|\det\Lambda_R(\vec{r})|}$, with a complex gauge field in terms of $v_F(\vec{r})$ given by $\vec{\rho}(\vec{r}) = \frac{v_F}{2}i\hbar\Lambda^*\vec{\nabla}v_F^{-1}(\vec{r})$, which makes hermitian the hamiltonian. Again, we have reduced the number of parameters in the anisotropy and inhomogeneity description of MDF dynamics, with an effective Fermi velocity spatially-dependent, instead of the Fermi velocity tensor usually found in several approaches [15, 78, 130]. The hamiltonian (3.12) describes the same dynamics that the hamiltonian (3.10) in systems presenting inhomogeneity and anisotropy, using the generalized concept of effective Fermi velocity $v_F(\vec{r})$, and the complex gauge field $\rho(\vec{r})$.

Finally, we pointed out that using the particular case of an inhomogeneous and isotropic transformation $\Lambda(\vec{r}) = a(\vec{r})\mathbb{I}$, where $a(\vec{r})$ is a real function and $\mathbb{I}$ is the 2×2 identity matrix, the Dirac hamiltonian with a position dependent Fermi velocity position is obtained, (see appendix A9)

$$H_D = -i\hbar\sqrt{v_F'(\vec{r})}\vec{\sigma}\cdot\vec{\nabla}[\sqrt{v_F'(\vec{r})}]. \tag{3.13}$$

Where we have used the expressions $v_F'(\vec{r}) = v_F a(\vec{r})$, $\vec{p_c} = \vec{p} = -i\hbar\vec{\nabla}$ and $\vec{\rho}(\vec{r}) = \frac{i\hbar}{2}v_F'(\vec{r})\vec{\nabla}v_F'^{-1}$ in (3.12). In this way, we show that the used hamiltonian for the study of the velocity-modulation in graphene superlattices [144, 145], can be derived from a $\Lambda(\vec{r})$ transformation satisfying the symplectic group condition.

In the next chapters, we show how the anisotropy matrix is connected with DFT calculations for uniaxial strain along the ZZ and AC direction in graphene, and its relation with the hopping parameters from a TB approach to nearest neighbors in homogeneously strained graphene. This model leads to the Fermi velocity modulation, the expansion and contraction of the LLs spectra, and the development of the electron quantum optics allowing the emergence of novel devices.

3.2 Motion equations for inhomogeneous anisotropy and magnetic field

We derive the motion equations for the particular $\Lambda(\vec{r})$ transformation described in appendix A7. Thus, applying $\Lambda(\vec{r})$ in the Dirac-like hamiltonian at K valley, we obtained

$$H = v_F \begin{pmatrix} 0 & p_x a(x,y) - i p_y b(x,y) \\ a(x,y) p_x + i b(x,y) p_y & 0 \end{pmatrix}, \tag{3.14}$$

with a wavefunction $\vec{\Psi}(x,y) = (f_A^{(+)}, g_B^{(+)})$, describing the pseudospin ($\{f_A, g_B\}$). For a nonuniform magnetic or pseudomagnetic field B_z perpendicular to the anisotropic Dirac material [87, 103, 104], we do the minimal substitution $\vec{p} \rightarrow \vec{\pi}^{\pm} = \vec{p} + e\vec{A}^{\pm}$ in the free-field hamiltonian (3.14), where $\vec{A}(x,y)$ is a potential vector that can depend of the inhomogeneous strain and acts different in each valley [87, 103, 104]. We focus in the K valley and, decoupling the 2×2 equation system obtained from the Dirac equation $H\vec{\Psi} = E\vec{\Psi}$, we get

$$\begin{aligned} \Big\{(a\pi_x^+)^2 + (b\pi_y^+)^2 - \lambda_1(a\pi_x^+ + ib\pi_y^+) + i[a\pi_x^+, b\pi_y^+]\Big\} f_A^{(+)}(x,y) &= \frac{E^2}{v_F^2} f_A^{(+)}(x,y), \\ \Big\{(a\pi_x^+)^2 + (b\pi_y^+)^2 - \lambda_1(a\pi_x^+ + ib\pi_y^+) - i[a\pi_x^+, b\pi_y^+] + \lambda_2\Big\} g_B^{(+)}(x,y) &= \frac{E^2}{v_F^2} g_B^{(+)}(x,y), \end{aligned} \tag{3.15}$$

where $(a\pi_x^+)^2 = (ap_x)^2 + 2ea^2 A_x^{+2} p_x + e^2 a^2 A_x^{+2} - ie\hbar a \frac{\partial}{\partial x}(aA_x^+)$. A similar expression is obtained for $(b\pi_y^+)^2$ doing the changes $x \rightarrow y$ and $a \rightarrow b$. The commutator is given by $[a\pi_x^+, b\pi_y^+] = -i\hbar(a\frac{\partial b}{\partial x})(p_y + eA_y^+) + i\hbar(b\frac{\partial a}{\partial y})(p_x + eA_x^+) - i\hbar eabB_z^+$ with $B_z^+(x,y)$ the magnetic field generated by $\vec{A}^+$, the $\lambda_1(x,y) = i\hbar\frac{\partial a}{\partial x} + \hbar\frac{\partial b}{\partial y}$ and $\lambda_2(x,y) = \hbar^2\{-a\frac{\partial^2 a}{\partial x^2} - b\frac{\partial^2 b}{\partial y^2} + i(a\frac{\partial^2 b}{\partial x \partial y} - b\frac{\partial^2 a}{\partial x \partial y})\}$. For the K' valley, the same decoupled equation system is obtained with $g_B^{(-)}(x,y)$ and $f_A^{(-)}(x,y)$ instead of $f_A^{(+)}(x,y)$ and $g_B^{(+)}(x,y)$ respectively, with superscripts $(-)$ in the $\hat{\pi}$ operators and $\vec{A}$ vector potential. The 2×2 partial differential equation system (3.15) is an alternative way to describe the electron dynamics with deformed Dirac cones, in the presence of a nonuniform magnetic field where the anisotropic parameters have a spatial dependence. If we know the exact form of $a(x,y)$ and $b(x,y)$ from the dispersion relation or the Fermi velocity, it is possible to obtain the LLs solving the equation system (3.15). When the system shows an inhomogeneous unidirectional anisotropic profile, these functions must depend only on x (y) due to the translational symmetry on y (x). Assuming x dependence for the anisotropy parameters and using the Landau gauge

$\vec{A} = xB\hat{y}$, the p_y component of the linear momentum is conserved. Thus, the equation system in (3.15) is reduced to

$$
\begin{aligned}
-\frac{d}{dx}\left[a^2(x)\frac{d}{dx}f_A^{(+)}(x)\right] + \Bigg\{ \left(\frac{eBx}{\hbar}+k_y\right)^2 b^2(x)& \\
+\frac{d}{dx}\left[a(x)b(x)\left(\frac{eBx}{\hbar}+k_y\right)\right]\Bigg\}&f_A^{(+)}(x) = \frac{E^2}{\hbar^2 v_F^2}f_A^{(+)}(x),
\end{aligned}
$$

$$
\begin{aligned}
-\frac{d}{dx}\left[a^2(x)\frac{d}{dx}g_B^{(+)}(x)\right] + \Bigg\{ \left(\frac{eBx}{\hbar}+k_y\right)^2 b^2(x)& \\
-\frac{d}{dx}\left[a(x)b(x)\left(\frac{eBx}{\hbar}+k_y\right)\right] + R(x)\Bigg\}&g_B^{(+)}(x) = \frac{E^2}{\hbar^2 v_F^2}g_B^{(+)}(x).
\end{aligned}
\tag{3.16}
$$

where $R(x) = 2b(x)\left(\frac{eBx}{\hbar}+k_y\right)\frac{da}{dx} - a(x)\frac{d^2a}{dx^2}$. The equations (3.16) are a general differential equations for the electron's wavefunction in nonuniform unidirectional anisotropy, which can be solved using the Sturm-Liouville theory [146] with eigenvalues $\lambda_n = E_n^2/\hbar^2 v_F^2$.

3.3 Optics with anisotropic massless Dirac fermions

Electron quantum optics arises from the analogy between photons and electrons. The similarities of both physical entities reside in the dual nature between corpuscle and wave. This duality has been well used in technological applications, being the electron microscope an example. Nowadays, condensed matter and optics are ever more entangled with the rise of new Dirac materials, which represent an important platform for the development of novel electron quantum optics devices, allowing the feedback between both physics areas. In this aspect, graphene *pn*-junction has been the most famous example for the implementation of the KT [4, 55]. Further, it was found that electron beam incident on *pn* junction is negatively refracted, such as a metamaterial. Thus, a version of the Veselago lens was proposed and experimentally corroborated in graphene [57, 147, 148, 149]. Furthermore, collimation and valley beam splitter was proposed in a doped *n* region beyond of the linear dispersion relation, where trigonal warping distortion was pointed as the key ingredient in their tentative experimental implementation [56]. This interesting proposal has the disadvantage that, the charge carriers with a shortened de Broglie's wavelength, experience a greater dispersion caused by the atomistic detail.

However, systems based in strained graphene allow the development of a valley splitting and Goos-Hänchen effect in graphene without the trigonal warping [91]. Other systems offer the possibility of supercollimate electron beams through graphene superlattices [150]. Recently, the Hong-Ou-Mandel type interference for massless Dirac fermions in graphene and 3D topological insulators was theoretically studied [151]. Specular and ballistic transport effects were probed on line defects structure, local adsorption and weak potential barriers [152, 153, 154, 155]. These optics-like devices and effects are possible because the main commmon feature between photons and electrons in graphene is their linear dispersion relation.

Strain-engineering promises the develop of a wide variety of nanodevices through the control of the valley degree of freedom as information carry. From QFTCS, the design of valley and spin beam splitters [91, 92, 156, 157], electron confinement [69, 158], collimation [69, 150, 159], and generation of valley-polarized currents has been proposed [160, 161, 162]. In all those works, the shifted Dirac points are the main contribution caused by strain, which is embodied through the pseudo-vector potential, neglecting the anisotropy and tilting of the Dirac cone. In this section, we show how our effective model incorporates the shifted Dirac points and the anisotropy of Dirac cone in the study of electron quantum optics. The homogeneous anisotropy can be induced through other mechanisms different to strain in the Dirac material. We derive a unconventional electron Snell law in anisotropic Dirac materials, that describes the charge carrier beam flowing through the optics-like devices: collimators, reflectors, Veselago lenses, valley beam splitters and filters. In particular, an implementation of electron quantum optics for two homogeneously strained graphene media is proposed.

3.3.1 Generalization of reflection and Snell's law in anisotropic Dirac materials

We study the transmission of Anisotropic Massless Dirac Fermions (AMDFs) in a valley electron quantum optics device, which can be conformed by two different anisotropic Dirac materials, as shown in Fig. 3.2 (a). In graphene and in topological insulators for instance, the regions I and II can be doped using two external gates V_1 and V_2. Whereas in artificial systems as photonic crystals, the simulation of an external gate is obtained from the frequency shift of

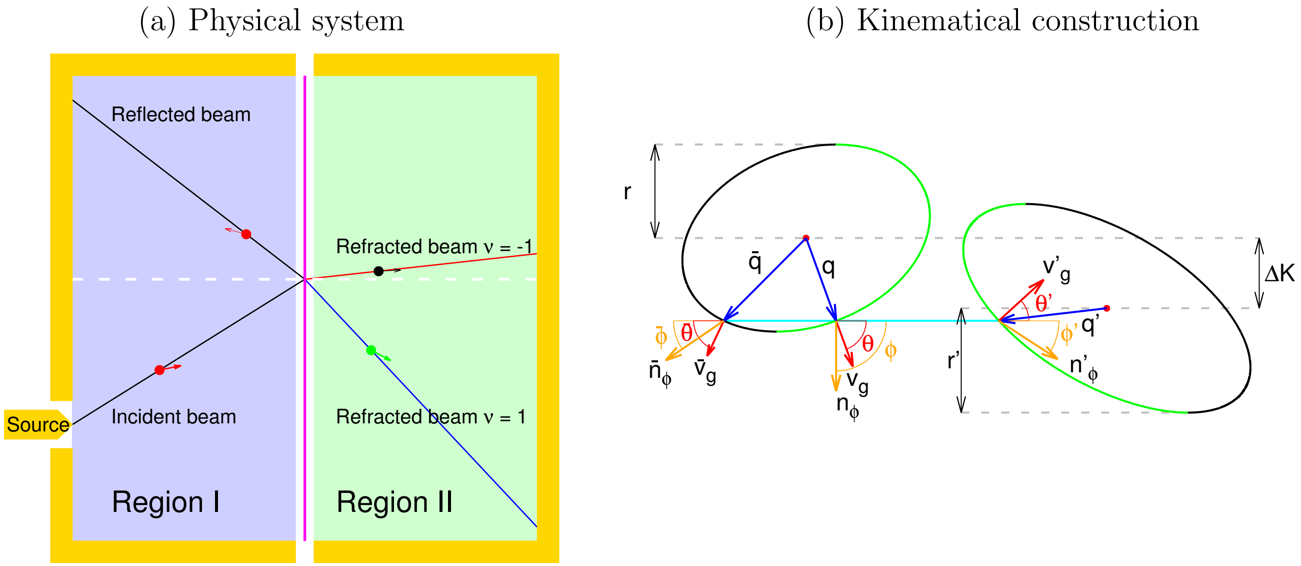
(a) Physical system

(b) Kinematical construction

Figure 3.2: Scheme of massless Dirac fermions refraction and kinematical construction in two anisotropic Dirac materials. Controlling the anisotropy of both materials is possible to induce transitions in the optical-like device operation. Thus, (a) unpolarized charge carrier beam from the region I arriving to the interface can be reflected, transmitted or doubly refracted due to the lifting of the two-fold valley degeneracy. A kinematical construction in (b), illustrates how the shifted Dirac points and elliptical transversal section of the Dirac cone affects the device operation. In the left (right), ellipse corresponds to the transversal section of Dirac cone for the K valley in the region I (II). Red arrows denote the group velocity direction defining the true incidence and refraction angles θ and θ', respectively. Turquoise line represents the q_y conservation, establishing the relation between both angles through the unconventional electron Snell's law (3.18) derived from GA.

electromagnetic waves when the distance among dielectrics is shrunken [159]. The separation between gates can be neglected if the condition $k_F d < 1$ is satisfied, being k_F the Fermi wave vector and d the split-gate length. Thus, the potential profile $V(x)$ can be approximated to a sharp potential step due to the abrupt change at interface. Such assumption is considered for avoiding the angular filter of electron beams beyond the normal incidence [163, 164, 165]. Moreover, the coherence length and the mean free path are expected to be larger than the device's dimensions, allowing that the system is within the ballistic transport regime. These considerations, which are necessary for performing electron quantum optics, have been achieved experimentally in graphene [55, 148, 149]. In this way, controlling the anisotropy through an inductor mechanism and the doping with external gates, the electron optics device operates according to the particular purpose of design. Thus, when a point source injects the electronic waves with a wide angular distribution, the device changes the direction of the electron beams of a specific way, and an extended drain collects the output electron beams.

When incoming AMDFs arrive at interface, there is a R probability for the reflected beams, where R is the reflection coefficient. In order to obtain R, the performation of matching conditions for the wavefunctions is required. From a general point of view, the hamiltonian for pseudospin 1/2 particles, which considers nonlinear terms and homogeneous anisotropy transformation on $\vec{p}$, is written as $H = v_F^0(\sigma_x g_x(\vec{p}\,'))+\sigma_y g_y(\vec{p}\,'))+V$, where $\vec{p}\,'$ is the transformed linear momentum in (3.1), $g_x(\vec{p}\,')$ and $g_y(\vec{p}\,')$ are general functions of $\vec{p}\,'$. The eigenstates of this hamiltonian are given by the spinors $|\Psi\rangle = \frac{1}{\sqrt{2}}(1, s\mathrm{e}^{i\phi})\mathrm{e}^{i\vec{k}\cdot\vec{r}}$, being $\phi = \arctan(g_y(\vec{p}\,')/g_x(\vec{p}\,'))$ the pseudospin angle and $s = \mathrm{sgn}(E - V)$ the band index. Thus, the wavefunctions $|\Psi_I\rangle = |\Psi\rangle_i + r|\Psi\rangle_r$ and $|\Psi_{II}\rangle = t|\Psi\rangle_t$ for the region I and II respectively, are matched at the interface, with r (t) the reflection (transmission) amplittude. Then, the R coefficient for propagation modes is obtained

$$R = |r|^2 = \frac{(s\cos\phi - s'\cos\phi')^2 + (s\sin\phi - s'\sin\phi')^2}{(s\cos\phi + s'\cos\phi')^2 + (s\sin\phi - s'\sin\phi')^2}, \tag{3.17}$$

where the denoted quantities with prime, excepting $\vec{p}\,'$, correspond to the region II. Transmission coefficient T is obtained in terms of R from the conservation of the probabiltiy current density, $T = 1 - R$. We note that the expression of R in (3.17) is the result of consider pseudospin 1/2 particles and the use of the boundary condition $\Psi_I(\vec{r})|_{x=0^-} = \Psi_{II}(\vec{r})|_{x=0^+}$, regardless the specific form of $g_j(\vec{p}\ ')$ with $j = x, y$. Notwithstanding, the relation of ϕ and ϕ' must be established knowing the particular expressions of $g_j(\vec{p}\ ')$, as well as through the conservation of E, p_y, and probability current density j_x. A nontrivial relation between ϕ and ϕ' can be obtained considering nonlinear terms of $\vec{p}_a$ in the hamiltonian. However, the requirement $\lambda_F > d$ is better satisfied due to the increment of λ_F when the hamiltonian depends linearly of $\vec{p}\ '$. With longer wavelengths, the scattering caused by the atomic details can be neglected. Further, the resemblance between AMDFs and photons is more clear making $g_j(\vec{p}\ ') = p\,'_j$, and a dispersion relation in shape of an elliptical cone is obtained.

In most of the Dirac materials, the electronic band structure shows two inequivalent Dirac cones due to the invariance of time reversal symmetry. We focus only in the K valley, since a similar description is performed doing the change $\vec{K} \to -\vec{K}$. Thus, the conservation laws of E, p_y and j_x can be illustrated from a kinematical construction, as shown in Fig. 3.2.(b). The ellipses are the Dirac cone transversal section for the regions I and II satisfying the E conservation. The size of the ellipses are tuned through the external gates V and V', whereas the extremal angles θ_1 and θ_2, Dirac point position $\vec{K}$ and rotation angle θ_R for each ellipse can be modified using the AIM. We define the height difference between ellipses $\Delta K = |K'_y - K_y|$ and the vertical half-width as r and r'. With geometrical arguments, r is expressed in terms of Dirac cone paremeters as $r = \frac{|E-V|w}{\hbar v_F \lambda_1 \lambda_2}$, where $\lambda_i = \cot\theta_i$ with $i = 1, 2$ and $w = \sqrt{\lambda_1^2 \cos^2\theta_R + \lambda_2^2 \sin^2\theta_R}$. A horizontal line indicates the p_y conservation. When the line intersects both transversal sections, the incoming AMDFs are transmitted to the other region through propagation modes. Otherwise, the transmission by evanescent modes could occur for some values of p_y, whether a horizontal line does not intersect the ellipse in the region II. Since the current density $\vec{j}$ is directed outward (inward) of the ellipse for $s = 1$ ($s = -1$), the AMDF beams are refracted in different way for intra and interband transmission. This explain how AMDFs from the conduction band are negatively refracted crossing the valence band in an np-junction.

Since each electron quantum optics device has a different kinematical construction, we establish a geometrical criterion of operation which allows to classify the possible devices when r, r' and ΔK are tuned through the external gates and the AIM. For $r << r'$ and $|\Delta K| < r' - r$, the propagation modes is guaranteed in the whole of incidence range $-r \leq p_y \leq r$. Then, the kinematical construction shows an ellipse with a vertical half-width in the region I smaller than in the region II. Hence, the refraction range is very narrow compared with the incidence range. Indeed, this corresponds to the operation principle of a collimator, since a wide angular distribution of incoming AMDF beams are converted by the device to an aligned outcoming beams, as seen in Fig. 3.3 (b) and (c). Such device also acts as a valley beam splitter for $\Delta K \neq 0$, because AMDFs from K^+ valley are collimated to a different direction than these from K^- valley, as seen in Fig. 3.3 (e) and (f). Increasing r, collimation effect disappears. However, valley beam splitter continues operating as long as $r < r'$, as shown in Fig. 3.4 (b) and (d). Tuning ΔK such as $r' - r < |\Delta K| < r' + r$, the incidence range for propagation modes is reduced as long as ΔK tends to $r' + r$. Thus, valley filtering effect begins to emerge. This effect consists of a total internal reflection for AMDFs from K^+ (K^-) valley and refraction for AMDFs from K^- (K^+) valley, where both incoming particles have the same direction of incidence. When $r' - r < \Delta K < r'$, valley beam splitter and filter are mixed and the full transition to a complete valley filter is reached if $r' < \Delta K < r' + r$, as shown in Fig. 3.5 (b) and (d). The full absence of propagated modes is obtained for $\Delta K > r + r'$ and the device works as a reflector, which is important for switching purposes due to the creation of a tunable transmission gap. On the other hand, an extended collection of unconventional Veselago lenses are achieved with the focusing condition $r = r'$, $s = -s'$ and $\Delta K = 0$ (see Fig. 3.6 (b) and (e)) which is the generalization of the well-known condition $E = V'/2$, $V = 0$ and $s = -s'$ for Veselago lens in graphene. Further, obtaining the geometrical criterion $r = r'$, $s = s'$ and $\Delta K = 0$ is possible the implementation of a novel device that we have called super divergent lens, (see Fig. 3.7).

In order to characterize these devices, we derive the reflection and Snell's law as well as the reflection and transmission coefficient, establishing a complete analogy with the light optics. We use the Heisenberg equation for obtaining the velocity operator $\hat{\vec{v}} = -\frac{i}{\hbar}[\vec{r}, H] = v_F^0 A^T \vec{\sigma}$. The group velocity of incoming and outcoming AMDFs is calculated from the expected value of $\hat{\vec{v}}$, which is written as $\vec{v} = \langle \Psi | \hat{\vec{v}} | \Psi \rangle = s v_F^0 A^T \hat{n}(\phi)$, where $\hat{n}(\phi) = (\cos\phi, \sin\phi)$ is the unitary vector, indicating the pseudospin direction. From the definition of the pseudospin angle ϕ, the linear momentum $\vec{p}$ can be expressed in terms of $\hat{n}(\phi)$ as $\vec{p} = p' A^{-1} \hat{n}(\phi)$. We note that the velocity, linear momentum and pseudospin are not always paralells in elliptical Dirac cones. Hence, ϕ and ϕ' can not be interpreted as the angle of incidence and refraction respectively, as is usually assumed for circular Dirac cones in pristine and strained graphene. The genuine angles of incidence θ and refraction θ' are defined by the components of group velocity in the region I as $\vec{v} = v(\theta)\hat{n}(\theta)$, where $\hat{n}(\theta) = (\cos\theta, \sin\theta)$. In the region II, the group velocity has the same form and its parameters are denoted with primes. Thus, using $\vec{p}$ in terms of θ with $\vec{p} = s\frac{p' v(\theta)}{v_F}(A^T A)^{-1}\hat{n}(\theta)$, the anisotropy matrix decomposition (3.5), and the p_y conservation written as $p_y + \hbar K_y = p'_y + \hbar K'_y$, we can establish the following AMDFs Snell's law

$$\frac{s|E-V|}{\hbar v_F \lambda_1 \lambda_2}(\lambda_2 \sin\theta_R \cos\chi + \lambda_1 \cos\theta_R \sin\chi) + K_y = \frac{s'|E-V'|}{\hbar v_F \lambda'_1 \lambda'_2}(\lambda'_2 \sin\theta'_R \cos\chi' + \lambda'_1 \cos\theta'_R \sin\chi') + K'_y. \tag{3.18}$$

Where χ is an auxiliar quantity related with the Dirac cone parameters and the angle of incidence through

$$\hat{n}(\chi) = (\cos\chi, \sin\chi) = \tfrac{v(\theta)}{v_F}(\lambda_1^{-1}\cos(\theta-\theta_R), \lambda_2^{-1}\sin(\theta-\theta_R)) \tag{3.19}$$

being $v(\theta) = v_F\lambda_1\lambda_2[\lambda_2^2\cos^2(\theta-\theta_R) + \lambda_1^2\sin^2(\theta-\theta_R)]^{-1/2}$. This Snell's law can be reduced to the known law of massless Dirac fermions in isotropic systems such as pristine graphene and 3D topological insulators, using $\lambda_1 = \lambda_2$ that corresponds to circular Dirac cones. We note that in Dirac materials with two nonequivalent Dirac cones, AMDFs from K^- valley obey an similar Snell's law doing the substitution $K_y \to -K_y$ and $K'_y \to -K'_y$. Therefore, AMDFs from K^+ valley are transmitted with an angle of refraction different to AMDFs from K^- valley as long as, the designed device satisfies the condition $K_y \neq K'_y$. When $\Delta K = 0$, the optics of AMDFs is valley-independent and the refraction is expected to be different in comparison with the conventional electron optics for isotropic systems. Further, if $V = V'$ the angle of refraction is independent of E and a dispersionless optics is obtained.

In contrast to the traditional optics, AMDFs obey a more general reflection law. We can see in Fig. 3.2 (b) that, although p_y is conserved, the group velocity components along y for incident and reflected particles result to be different. In this way, a relation between the reflection $\overline{\theta}$ and incidence θ angles can be derived using the p_y conservation and the group velocity components, establishing the following AMDFs reflection law

$$\tan\overline{\theta} = \tan\theta - \frac{(\lambda_1^2-\lambda_2^2)\sin 2\theta_R}{w^2}, \tag{3.20}$$

which is independent of E, V and V' as well as the band indexes s and s'. This reflection law suggests that for $\theta = \arctan\left[(\lambda_1^2-\lambda_2^2)\sin 2\theta_R/2w^2\right]$ there is retroreflection when $R \neq 0$. The expression (3.20) indicates that all the virtual beams are met in the spot $(\overline{x}, \overline{y}) = (x_0, -x_0(\lambda_1^2 - \lambda_2^2)\sin 2\theta_R/2w^2)$, where $(-x_0, 0)$ is the location of the point source. Further, the virtual image in the region II of an object in the region I is deformed and rotated. We note that for $\theta_R = 0$, the habitual reflection law $\theta = \overline{\theta}$ is restored.

Using the AMDFs Snell's law, we found an analytical expresssion of the reflection coefficient. The relation between ϕ and θ is given by $\hat{n}(\phi) = sR(-\alpha)\hat{n}(\chi) = s\hat{n}(\alpha+\chi)$. Then, the coefficient R in (3.17) is written as

$$R = \frac{\sin^2\left[\frac{1}{2}(\alpha-\alpha'+\chi-\chi')\right]}{\cos^2\left[\frac{1}{2}(\alpha+\alpha'+\chi+\chi')\right]}, \tag{3.21}$$

which is a function of θ using the definition of χ and solving (3.18) for χ'. An important remark must be performed regarding the KT in the system shown in Fig. 3.2 (a). We have noted that using $\Delta K = 0$ in (3.21), transmission probability of AMDFs could be less than unity under normal incidence. This fact contrasts with the KT in pristine graphene, where electrons tunnel perfectly along that direction. There are two fundamental reasons for the emergence of KT: the first, electrons have a linear dispersion, and the second is due to the conservation of pseudospin σ_x along the normal direction [4, 55]. While in the current system, the condition for the KT of AMDFs depends of the conservation of $(a_{11}\sigma_x + a_{21}\sigma_y)/w = (a'_{11}\sigma_x + a'_{21}\sigma_y)/w'$ when $p_y = p'_y = 0$ and which guarantees the alignment of pseudospins, namely $\alpha + \chi = \alpha' + \chi'$ doing $R = 0$ in (3.21). For this reason, the KT of AMDFs has a prefered direction, and it does not necessary occur under normal incidence, due to that the group velocity and pseudospin are not always paralells. Hence, incoming AMDFs with KT can be also refracted. The explanation of this atypical behavior of the KT is better understood analyzing the velocity components of incoming and outcoming AMDFs, as shown in Fig. 3.6 (b), (c) and (d). In general, $v_y \neq 0$ for $p_y = 0$ and the angle of incidence can be obtained as $\theta = \arctan(v_y/v_x) = \arctan((\lambda_1^2 - \lambda_2^2)\sin 2\theta_R/2w^2)$. In the region II, the conservation of pseudospin makes posible the KT, but in this case $v'_y \neq v_y$ and $v'_x \neq v_x$ change the direction of the KT, having the angle of refraction $\theta' = \arctan(v'_y/v'_x) = \arctan((\lambda_1'^2 - \lambda_2'^2)\sin 2\theta'_R/2w'^2)$. We note that when $\theta_R = \theta'_R = 0$, the habitual KT is recovered.

We can characterize the collimator device using the results (3.18) and (3.21). Collimator can be designed setting the Dirac cone parameters to have $\theta_R = 0$ and $\lambda_1 >> \lambda_2$. In the region II, the Dirac cones have $\theta'_R = 0$ and $\lambda'_2 >> \lambda'_1$. Thus, the geometrical criterion for collimation is satisfied. Even more, if we consider the dispersionless optics condition $\Delta K = 0$ and $V = V' = 0$ the effect is independent of the energy E. Under these requirements, we plot θ' and T as a function of θ evidencing the collimation of AMDFs, in Fig. 3.3. Removing the dispersionless optics condition with $V = 0$ and $V' = V_0 > 0$, collimation depends of the doping level. However, an improvement is observed for $E < V_0/2$ due to the increment of r'. This can be quantified calculating the angular spread $\Delta\theta \approx 2\frac{\lambda_2'^2|E|}{\lambda'_1\lambda_2|E-V_0|}$ which goes to zero for a high step potential $E << V_0$. Further, effective angular spread results to be smaller than $\Delta\theta$, since the transmission probability of grazing incidence rays is considerably decreased, as shown in Fig. 3.3

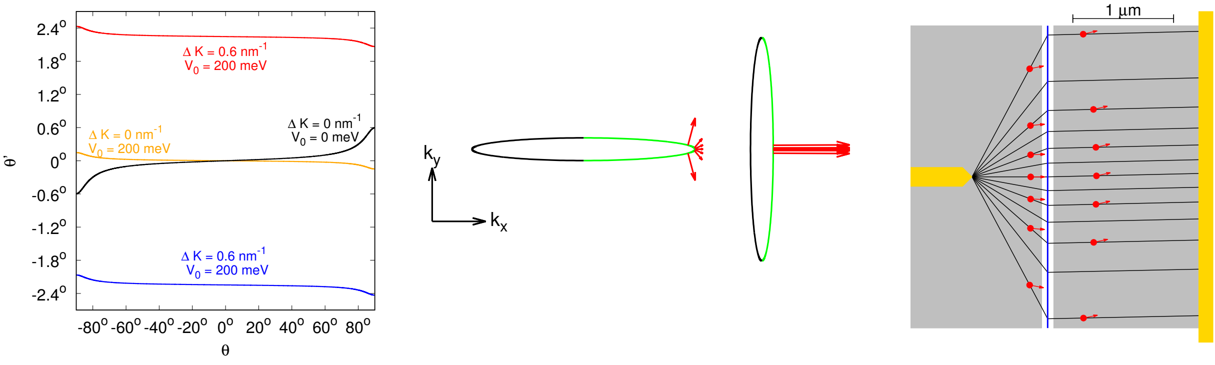

(a) Snell's law (b) Kinematical construction (c) Physical system

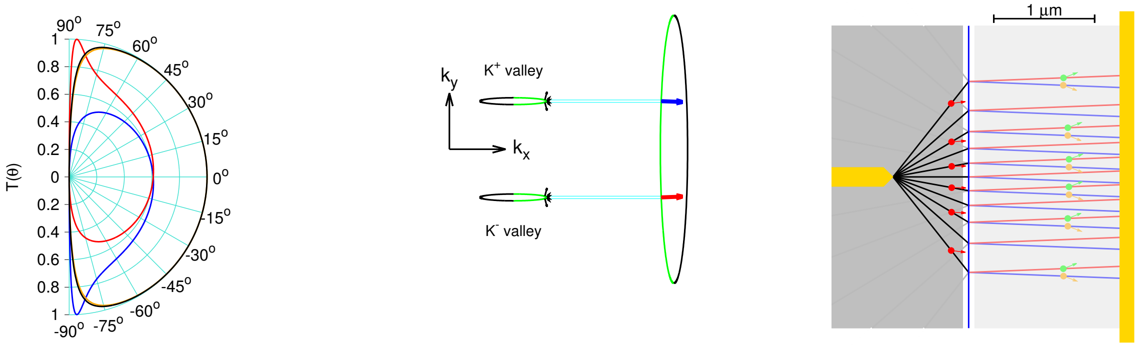

(d) Transmission (e) Kinematical construction (f) Physical system

Figure 3.3: Collimation of incoming AMDF beams using two media, setting the Dirac cone parameters in the region I as $\theta_1 = 80^\mathrm{o}$, $\theta_2 = 30^\mathrm{o}$, $\theta_R = 0^\mathrm{o}$, $\alpha = 0^\mathrm{o}$ and in the region II, $\theta'_1 = 30^\mathrm{o}$, $\theta'_2 = 80^\mathrm{o}$, $\theta'_R = 0^\mathrm{o}$, $\alpha' = 0^\mathrm{o}$. In (a) θ' is shown as a function of θ for $\Delta K = 0$ nm^{-1} and $V' = 0$ meV (black), $V' = 200$ meV (orange), $\Delta K = 0.6$ nm^{-1} and $V' = 200$ meV in K^+ (blue) and K^- (red) valleys. In all examples the Fermi energy is the same, $E = 40$ meV. (b) Kinematical construction for the case $\Delta K = 0$ nm^{-1} and $V' = 0$ meV in (a), green sides indicate the intra band transmission. The size and direction of the red arrows show the group velocities for incident and refracted AMDFs, which are based in analytical calculations. A collimator device is shown in (c) corresponding to the kinematical construction in (b). From a semiclassical point of view, an electrode injects an angular distribution of AMDFs. Each particle is represented by a red ball and an arrow denoting its pseudospin orientation. The changes in the pseudospin orientation, the path line and the direction after crossing the interface (blue line), correspond to the calculated values of θ', ϕ' and $v'_g(\theta)$. (d) Transmission coefficient as a function of θ for the considered cases in (a). (e) Kinematical construction when $\Delta K = 0.6$ nm^{-1} and $V' = 200$ meV. (f) Collimator and valley beam splitter device: AMDFs have different θ' for K^+ and K^- valley, being approximated independent of θ. The refracted AMDFs of K^+ and K^- valley are represented by green and orange balls. The intensity on the lines vary according to the transmission probability. Thus, the black path is considered to have 50 % of both valleys. Hence, the half of intensity for the red and blue lines are shown.

(d). Therefore, the most of the incoming rays have a negligible reflection probability because the restriction $\lambda_1 >> \lambda_2$ makes that $p_y \approx 0$. Thus, the KT condition is approximated guaranteed for a wide angular distribution of incoming AMDFs which pass completely collimated to the region II. The high efficiency of transmission can be quantified from the average of $T(\theta)$, as $\langle T\rangle \approx 1 - 4\lambda_1/3\pi\lambda_2$ which is near to one. For an idealized collimator ($r = 0$) with isotropic media, the expected efficiency of transmission is approximated to $\langle T\rangle \approx 0.73$ evidencing the importance of fabricate devices inducing anisotropy in both regions.

Introducing the valley dependency $\Delta K \neq 0$ and remaining $r << r'$, collimation persists for AMDFs from the same valley, as shown in Fig. 3.3 (a), (d), (e) and (f). In this way, the collimator also operates as beam splitter, because AMDFs from K^+ valley have a different angle of refraction than these from K^- valley, as seen in Fig. 3.3 (e) and (f). However, KT is removed decreasing the efficiency of transmission. Furthermore, a singular feature in the transmission of AMDFs for valley beam splitter and valley filter is observed, in Figs. 3.4 (c) and 3.5 (c). It has always been thought that the complete global symmetry of $T(\theta)$ is restored by the time reversal symmetry, when the transmission of K^+ and K^- electrons of strained graphene is shown [37, 91]. Such affirmation is analyzed more carefully for valley-dependent devices designed with anisotropy. Indeed for $\theta_R = \theta'_R = 0$, we can see that the mirror symmetric transmission of K^+ and K^- AMDFs is preserved due to $T^+(\theta) = T^-(-\theta)$. Nevertheless, rotating Dirac cone $\theta_R = 30^{\circ}$ in the region I the mirror symmetric transmission breaks. Therefore, asymmetric global transmission is observed because under the time reversal symmetry operation $p_y \to -p_y$, the x component of velocity is given by $v_x(p_y) = v_x(-p_y)$ but the y component is $v_y(p_y) \neq -v_y(-p_y)$, making that $T^+(\theta) \neq T^-(-\theta)$. Such fact is confirmed calculating the critical angles of the valley filter

$$\theta_c^{\nu} = \arctan\left[\frac{s\nu\lambda_1\lambda_2(\Delta K - r')}{w^2\sqrt{r^2 - (\Delta K - r')}} + \frac{(\lambda_1^2 - \lambda_2^2)\sin(2\theta_R)}{2w^2}\right], \tag{3.22}$$

where ν indicates the pseudospin valley, with $\nu = 1$ ($\nu = -1$) the expression for K^+ (K^-) valley is obtained. In general, the incidence ranges of K^+ and K^- AMDFs are different but they have the same length when $\theta_R = 0$ in (3.22). Thus, mirror symmetric transmission remains for $\theta_R = \theta'_R = 0$.

A device of interest in electron optics is the focusing of an electron flow through a Veselago lens. In the optics of AMDFs, Veselago lens appears even when some AMDFs are positively

(a) Snell's law (b) Kinematical construction

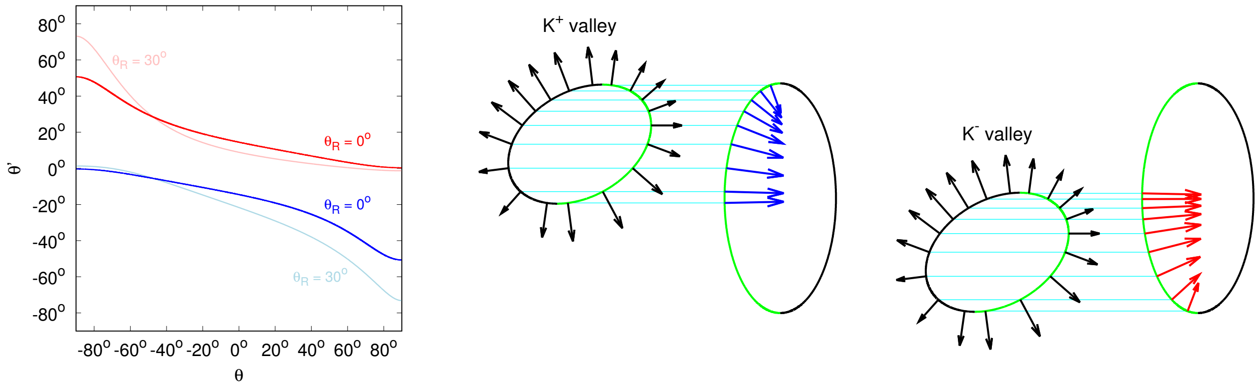

(c) Transmission (d) Physical system

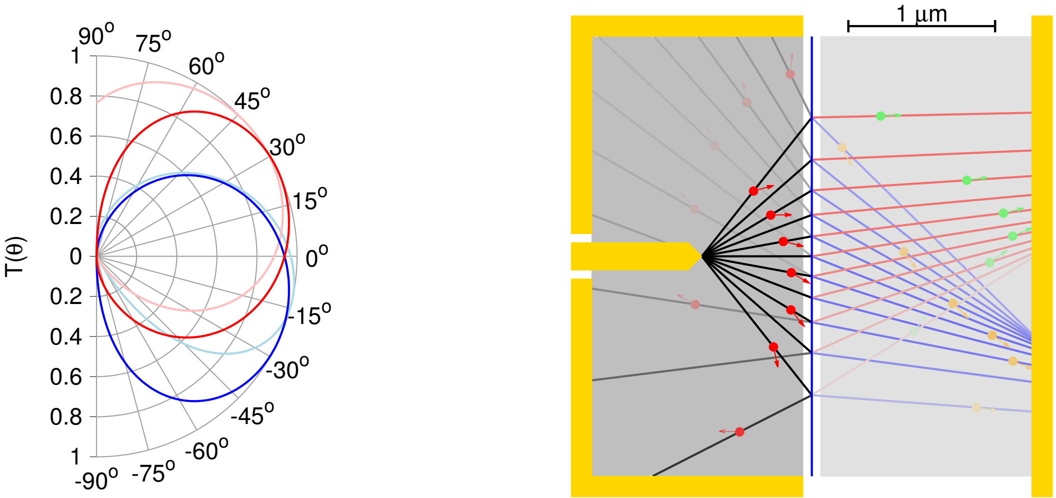

Figure 3.4: Characterization of a valley beam splitter with two media, setting the Dirac cone parameters in the region I as $\theta_1 = 60^o$, $\theta_2 = 50^o$, $\theta_R = 30^o$, $\alpha = 0^o$ and in the region II, $\theta_1' = 40^o$, $\theta_2' = 60^o$, $\theta_R' = 0^o$, $\alpha' = 0^o$. (a) Comparison of θ' as a function of θ when $\theta_R = 30^o$ and $\theta_R = 0^o$ being $\Delta K = 0.09$ nm^{-1}, $V = 0$ meV and $V' = 100$ meV. (b) Kinematical construction of the valley beam splitter: black arrows indicate the group velocity for incident AMDFs in green side, and reflected AMDFs in black side, showing an atypical reflection behavior. The blue and red arrows in the region II have different directions which yield the split between valleys. (c) Global symmetry (asymmetry) along $\theta = 0^o$ is observed for the transmission probability when $\theta_R = 0^o$ ($\theta_R = 30^o$). (d) Valley beam splitter device: the pseudospin orientation, angles of refraction and group velocities are based in analytical calculations. The path intensities indicate the probability in transmission and reflection.

refracted. The last is clarified finding a geometrical relation between θ and θ' of a convergent lens with asymmetric spot, (see Fig. 3.6 (a)-(c)). Thus, a divergent flow emitted at $(-x_0, 0)$ on the region I (see Fig. 3.6 (c)) is converted to a convergent flow by the device and met again in

(a) Snell's law (b) Kinematical construction

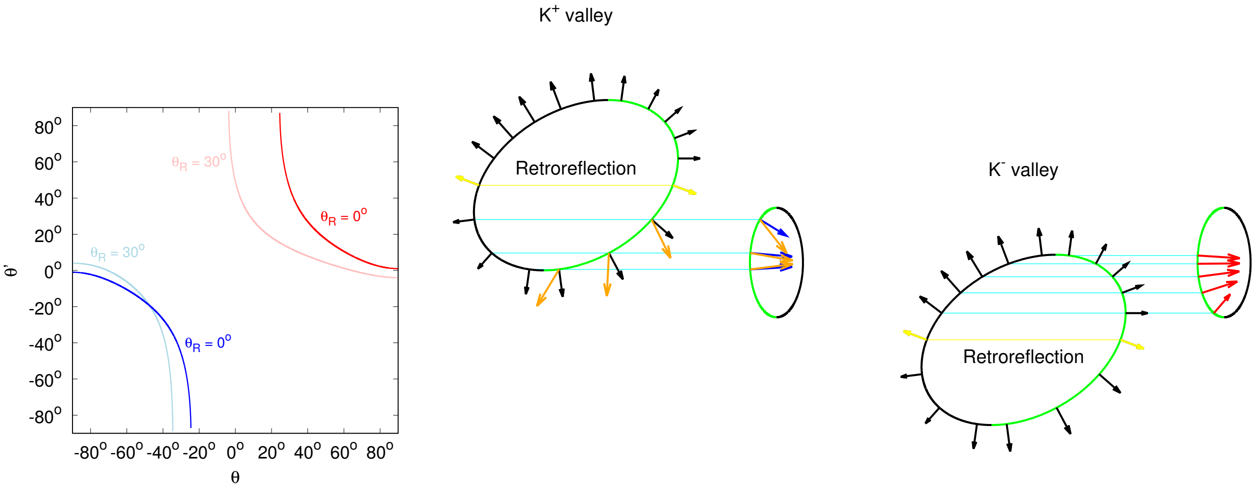

(d) Transmission (e) Physical system

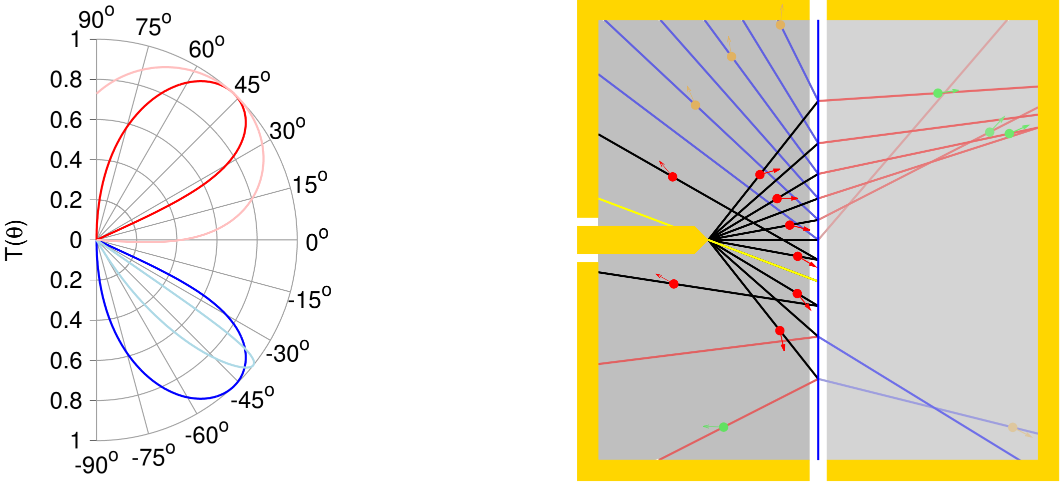

Figure 3.5: Characterization of a valley filter with two media, having the same set of Dirac cone parameters than the valley beam splitter in Fig. 3.4, where only $V' = 60$ meV is modified. (a) Comparison of θ' as a function of θ when $\theta_R = 30^o$ and $\theta_R = 0^o$. (b) Kinematical construction of the valley filter: black arrows indicate the group velocity for incident AMDFs in green side and reflected AMDFs in black side. Yellow arrows represent the group velocity with opposite direction giving rise to the retroreflection in both valleys. There are incidence ranges where total internal reflection is observed for one of the valleys. (c) As in the valley beam splitter device, global symmetry (asymmetry) along $\theta = 0^o$ is observed for the transmission probability when $\theta_R = 0^o$ ($\theta_R = 30^o$). (d) Physical system shows the filtering effect, two colectors detect the reflected and refracted AMDFs in both sides of the device. Yellow line is the path where the retroreflection occurs.

(a) Snell's law (b) Kinematical construction (c) Physical system

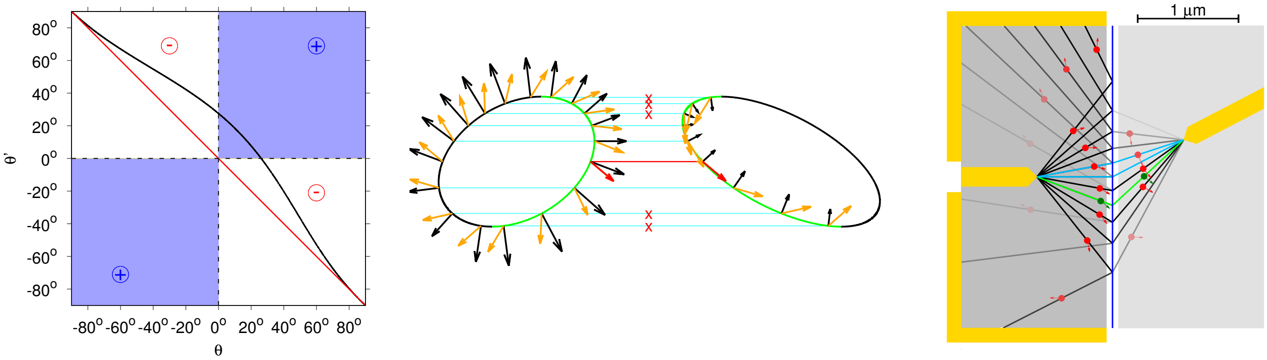

(d) Transmission (e) Kinematical construction (f) Physical system

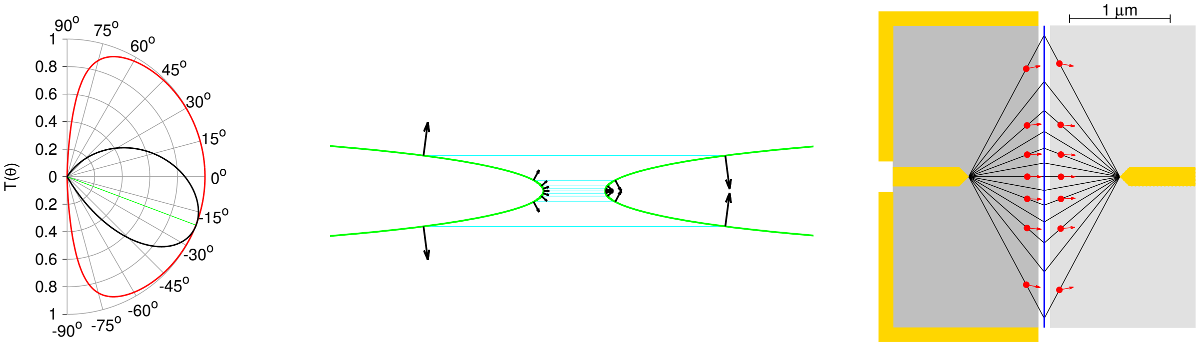

Figure 3.6: Characterization of symmetric and asymmetric Veselago lens. The set of Dirac cone parameters for the asymmetric Veselago lens in the region I are: $\theta_1 = 40^o$, $\theta_2 = 30^o$, $\theta_R = 30^o$, $\alpha = 0^o$ and region II, $\theta_1' = 50^o$, $\theta_2' = 70^o$, $\theta_R' = 62.6^o$, $\alpha' = 0^o$. For the symmetric Veselago lens, the set of values in the region I and II are: $\theta_1 = \theta_1' = 80^o$, $\theta_2 = \theta_2' = 30^o$, $\theta_R = \theta_R' = 0^o$, and $\alpha = \alpha' = 0^o$. (a) With the Fermi energies $E = 50$ meV and $E = 71.6$ meV for the symmetric and asymmetric Veselago lens respectively, being $V = 0$ meV and $V' = 100$ meV, the flux convergence is reached. (b) Kinematical construction of the asymmetric Veselago lens: orange and black arrows indicate the pseudospin direction and group velocity, respectively. Red line and arrows show the pseudospin conservation and how the KT is deflected due to the change of direction in the group velocity. The x red marks point out the forbidden states which do not conserve the current density, then total internal reflection emerges. (c) Unconventional Veselago lens, the emitted AMDFs flux by the electrode source is met again in an asymmetric spot. Green lines show the path of AMDFs with KT when $\theta = -20.7^o$. Some particles have positive refraction doing possible the convergence of beams. (d) Transmission probability as a function of θ: the red, black and blue curves correspond to the symmetric and asymmetric Veselago lenses, using the same set of values that in (a). Green line indicates the direction of KT. (e) Zoom of the kinematical construction for the symmetric Veselago lens. (f) Proposal of a symmetric Veselago lens using materials with elliptical Dirac cones.

the asymmetric spot at (x_0', y_0'). The geometrical relation between θ and θ' is given by $\tan\theta' = -\frac{x_0}{x_0'}\tan\theta + \frac{y_0'}{x_0}$. Then, part of the incoming flow at incidence range $0 \leq |\theta| \leq |\arctan(y_0'/x_0)|$ has positive refraction, as shown in Fig. 3.6 (a) and (c). Such lens can be obtained with the general focusing condition $\Delta K = 0$, $r = r'$ and $s = -s'$. With that criterion is possible to show that for $E = V_0(1 + \lambda_1'\lambda_2' w/\lambda_1\lambda_2 w')^{-1}$, AMDFs Snell's law satisfies the geometrical relation between θ' and θ of an asymmetric Veselago lens, having a tunable spot as a function of Dirac cone parameters. Satisfying the KT requirements, convergence of the outcoming beam towards the spot is not destroyed since the KT path deflects. In a particular case, where the region I and II have the same anisotropy further that $\theta_R = \theta_R' = 0$, the conventional Veselago lens with symmetric spot is recovered, (see Fig. 3.6 (a) and (d)-(e)). Once more, the efficiency of transmission $\langle T\rangle = \lambda_2/(\lambda_1 + \lambda_2)$ is enhanced and in the limit $\lambda_1 << \lambda_2$, $\langle T\rangle$ tends to one, which contrasts with the value of $\langle T\rangle = 0.5$ for circular Dirac cones.

We have found a novel device whose operation is the counterpart of a Veselago lens, called super divergent lens. This device converts a diverging AMDF flow, emitted by a point source at $(-x_0, 0)$, to an outcoming divergent flow with a virtual spot located at $(-x_0', y_0')$, as seen in Fig. 3.7. The geometrical relation between θ and θ' is written as $\tan\theta' = \frac{x_0}{x_0'}\tan\theta + \frac{y_0'}{x_0}$. Thus, one part of the incoming AMDFs have a negative refraction within incidence range $0 \leq |\theta| \leq |\arctan(y_0'/x_0)|$, (see Fig. 3.7 (a) and (c)). This device arises when the diverging condition $\Delta K = 0$, $r = r'$ and $s = s'$ is satisfied. Then, Fermi energy is given by $E = V_0(1 - \lambda_1'\lambda_2' w/\lambda_1\lambda_2 w')^{-1}$ and AMDFs Snell's law has the same expression that the geometrical relation between θ and θ' for the outcoming divergent flow. The KT requirement encompasses the whole of incidence range in a super divergent lens. Then, the transmission coefficient is always one due to the conservation of pseudospin for any θ, as shown in Fig. 3.7 (b), (d) and (e). Such effect known as super KT has been predicted for pseudospin one massless particles [159, 166, 167]. Nevertheless, the physical explanation given here for the super KT of AMDFs, differs substantially to the reported in pseudospin one systems.

The design of each electron optics device requires the modulation of the GA parameters, and one way is to use two media conformed by Homogeneously strained graphene. In the next chapter, we show how the strain-engineering can be used in the implementation of electron quantum optics.

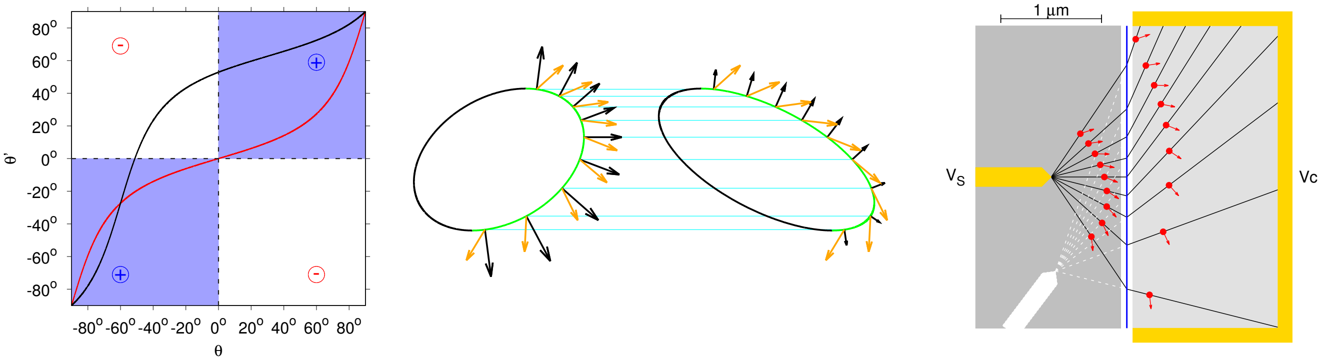

(a) Snell's law (b) Kinematical construction (c) Physical system

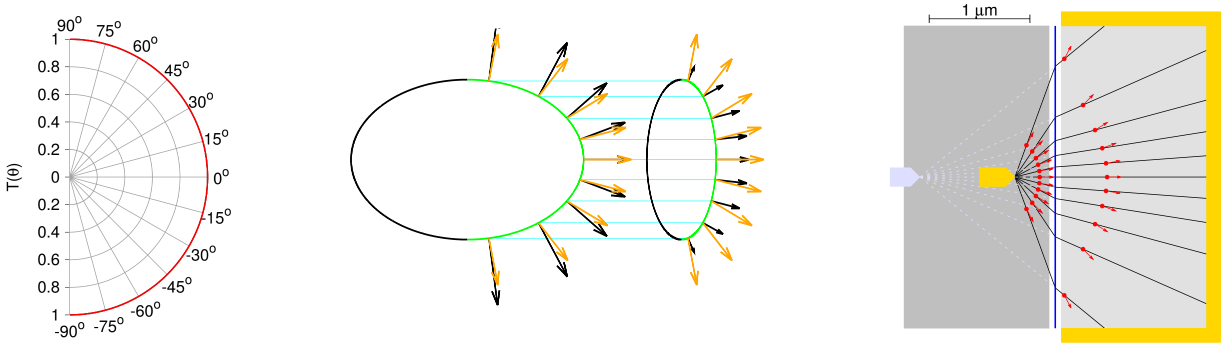

(d) Transmission (e) Kinematical construction (f) Physical system

Figure 3.7: Characterization of the symmetric and asymmetric super divergent lens. The set of Dirac cone parameters for the asymmetric super divergent lens are the same that in the asymmetric Veselago lens, where only the Fermi energy is changed to $E = 165.7$ meV. For the symmetric super divergent lens, the set of values in the region I are: $\theta_1 = 40^{\mathrm{o}}$, $\theta_2 = 30^{\mathrm{o}}$, $\theta_R = 0^{\mathrm{o}}$, $\alpha = 0^{\mathrm{o}}$ and the region II are: $\theta'_1 = 50^{\mathrm{o}}$, $\theta'_2 = 70^{\mathrm{o}}$, $\theta'_R = 0^{\mathrm{o}}$, and $\alpha' = 0^{\mathrm{o}}$, where the Fermi energy is $E = 126.6$ meV. (a) With $V = 0$ meV and $V' = 100$ meV in both super divergent lenses, θ' as a function of θ are shown. (b) Kinematical construction of the asymmetric super divergent lens: the pseudospins (orange arrows) are conserved for the whole incidence range giving rise to the emergence of a super KT. The group velocities (black arrows) change the direction and magnitude forming a divergent flux. (c) Asymmetric super divergent lens, the emitted divergent flux by the electrode source is diverged again at interface causing the effect of virtual source (white fictitious electrode). Some particles have negative refraction doing possible the divergence of beams. (d) All AMDFs have a transmission probability of one in any incident direction. (e) Kinematical construction for the symmetric super divergent lens, the pseudospins do not change their direction. (f) In a symmetric super divergent lens, the virtual source is found along the same axis that the real one.

Chapter 4

Applications of the Geometrical Approach to strained graphene

In recent years, many works have been devoted to find practical methods to control graphene's properties. A possible way is to perform a deformation on the graphene sample [11, 37, 45, 46, 48, 60, 63, 66, 71, 83, 103, 108, 168, 169, 170] or bilayer graphene [171], opening a wide range of possibilities to control the graphene extraordinary electronic and mechanical properties. Actual studies identify three main effects of uniaxial strain on low-energy band structure in graphene [11, 37, 66, 68, 170]. First, a slipping of the Dirac points out of the high symmetry points K and K'. Second, a distortion in the transversal section of the Dirac cones, breaking the isotropy of the Fermi velocity; and third, a small vertical axis tilting of Dirac cones, which could be negligible in most of the situations.

These effects have been totally or partially embodied in several effective models describing the dynamics of Dirac fermions [15, 38, 68, 89, 98]. As said in the overview chapter, two type of models for the study of the electronic-ground properties of strained graphene and related systems are frequently found in the literature [15, 39, 67, 68, 89, 98, 130]. On the one hand, the most popular approach known as QFTCS considers a hamiltonian developed around the high symmetry points of the first Brillouin zone [15]. Exceptional goals of this theory is the generation of pseudo-magnetic fields caused by the shifting of the Dirac points, described by a pseudo vector potential. On the other hand, there are approaches that included an effective hamiltonian developed around the Dirac points and for uniform strain, the pseudo vector potential is absent

[38, 68, 98]. Therefore, a more simple description of the Dirac fermions dynamics was obtained, where the explicity inclusion of the anisotropy of Dirac cones played an important role on the modulation of the electronic, vibrational and transport properties [38, 68, 98], which have been frequently neglected in many earlier contributions about valleytronics [69, 91, 156, 160].

Some theoretical works use an anisotropic mass model to find the LLs in graphene through topological considerations [172]. Another authors frequently analyze the properties of strained graphene using the Tight-Binding (TB) approximation, including the effect of deformation on the atomic distances through the scaling of the hopping parameters [11, 13, 15, 39, 68, 98]. In this chapter, we start studying the LLs in uniaxially strained graphene along the ZZ and AC directions, since under these directions the anisotropy matrix is diagonal. Thus, the coefficients of the linear momentum are related with the geometrical parameters of the distorted Dirac cone, and can be calculated from a fitting to the energy bands obtained with a DFT calculation. Then, we apply a minimal substitution in the free-field effective Dirac-like hamiltonian to get the LLs spectra. In particular, for uniaxial strain we found that the LLs spectra is contracted as a function of the deformation along the ZZ and AC directions. This contraction of the LLs spectra is due to the renormalization of the Fermi velocity with the strain, which is reduced by the stretching along these directions. In addition, we have evaluated the contribution of the tilting of Dirac cone axis to the contraction of the LLs in uniaxially deformed graphene.

On the other hand, we present how the geometrical approach can be related with the hopping parameters, showing the versatility of our model. We set the TB approach to nearest neighbors with three different hopping parameters, considering deformed lattice vectors on the Bloch expansion. Anisotropic exponential scaling rule has been used with a different Grüneisen constant in each hopping parameter, avoiding the usual expansion to first order in the strain tensor [38]. The TB hamiltonian is expanded around the Dirac point, where the relation between anisotropy matrix with the hopping parameters is found. Thus, effective Fermi velocity is expressed in terms of hopping parameters from the anisotropy matrix determinant in (3.4). We show that the obtained effective Fermi velocity from GA with TB method and DFT calculations, is identical to the one extracted from LLs in uniaxially strained graphene. However, our findings about the Fermi velocity differs with other approaches [15, 38, 68, 98]. Therefore, the prediction of the expansion and contraction of the LLs spectra could be the turning point of the discrepancy among models.

4.1 Landau levels in uniaxially strained graphene

To clarify our methodology, we show how to obtain the LLs in unstrained pristine graphene from an effective Dirac-like hamiltonian in a low energy and magnetic field regime. We treat the dynamics of an electron moving in a graphene sheet under a uniform magnetic field $\vec{B} = B\hat{z}$ perpendicular to the direction of propagation. We consider the electrons in graphene as massless Dirac fermions, having a linear dispersion relation ($E \propto k$) [3]. With $\vec{B} = 0$, the hamiltonian H only depends on the linear momentum $\vec{p}$ and can be represented by a 4 × 4 block diagonal matrix [24, 173]

$$H = v_F \begin{pmatrix} \vec{\sigma} \cdot \vec{p} & 0 \\ 0 & -\vec{\sigma} \cdot \vec{p} \end{pmatrix}, \tag{4.1}$$

where v_F is the Fermi velocity and $\vec{\sigma}$ are the Pauli matrices acting on the pseudo-spin space, which discriminate between the contribution of the two triangular sublattices present in graphene. Each block in the hamiltonian (4.1) represents the K and K' valleys, coinciding with the high symmetry points in absence of strain. For $B \neq 0$, we do the minimal substitution $\vec{p} \to \vec{p} + e\vec{A}$ in the free-field hamiltonian (4.1) with the Landau gauge $\vec{A} = xB\hat{y}$ [174, 175]. Due to the p_y conservation, the electron's wavefunction in graphene can be expressed using variables separation, having the form

$$\vec{\Psi}(x, y) = \mathrm{e}^{ik_y y}\vec{v}(x), \tag{4.2}$$

where $\vec{\Psi}(x, y)$ and $\vec{v}(x) = (\vec{\phi}^{(+)}(x), \vec{\phi}^{(-)}(x))$ are four-component vector functions with $\vec{\phi}^{(+)}(x) = (f_A^{(+)}(x), g_B^{(+)}(x))$ and $\vec{\phi}^{(-)}(x) = (g_B^{(-)}(x), f_A^{(-)}(x))$, describing the pseudospin ($\{f_A(x), g_B(x)\}$) and the valley (K or K') states ($\{\pm\}$).

We focus in the K valley, substituting (4.1) and (4.2) in the Dirac equation $H\vec{\Psi}(x, y) = E\vec{\Psi}(x, y)$, we obtain

$$\begin{aligned} v_F \left\{p_{ox} - ip_{oy}(k_y)\right\} g_B^{(+)}(x) &= Ef_A^{(+)}(x), \\ v_F \left\{p_{ox} + ip_{oy}(k_y)\right\} f_A^{(+)}(x) &= Eg_B^{(+)}(x), \end{aligned} \tag{4.3}$$

with $p_{ox} = p_x$ and $p_{oy}(k_y) = \hbar k_y + exB$. Decoupling the equation system (4.3) and using the commutator $[p_x, p_{oy}(k_y)] = -i\hbar eB$, we get

$$v_F^2\{p_x^2 + (\hbar k_y + exB)^2\}f_A^{(+)}(x) = \{E^2 - v_F^2\hbar eB\}f_A^{(+)}(x), \tag{4.4}$$

being similar to the quantum harmonic oscillator equation. Therefore, for Dirac electrons in the presence of a uniform perpendicular magnetic field, the LLs spectra is given by [175, 176]

$$E_n = \mathrm{sgn}(n)\hbar\omega^D\sqrt{|n|}, \quad \omega^D = v_F\sqrt{\frac{2eB}{\hbar}}, \tag{4.5}$$

with $n = 0, \pm1, \pm2, \ldots$ and degeneracy of $4SB/(h/e)$, where S is the sample area and (h/e) is the magnetic flux quantum. The four-fold degeneracy of LLs in graphene ($n \neq 0$) is due to a two-fold pseudospin and a two-fold valley degeneracy. While for $n = 0$, there is a two-fold degeneracy because the valley index is the same as the sublattice index. This result is different from the LLs spectra for conventional conductors $E_n = \hbar\omega(n + \frac{1}{2})$, where each level has a constant separation, while in graphene the LLs separation (4.5) decreases as $|n|$ increases. This behaviour has been confirmed experimentally [3, 54, 176]. It is important to mention that fitting the expression (4.5) to the experimental spectrum, the value of v_F can be obtained [176].

Landau levels in strained graphene

In previous studies on uniaxially strained graphene [11, 37, 68, 69, 72, 77, 98], it was shown that the Dirac cones have an elliptical cross section for low energy regime $|E| < 1$ eV. For elliptical cross section, the functions $a(x)$ and $b(x)$ are constants and they are related to the geometrical parameters of the ellipse, such as the semi-major axis ($A = E/a\hbar v_F$ for ZZ and $A = E/b\hbar v_F$ for AC direction) and semi-minor axis ($C = E/b\hbar v_F$ for ZZ and $C = E/a\hbar v_F$ for AC direction), or equivalently, scaling the energy axis with $q = E/\hbar v_F$, then $a = \cot\alpha = q/k_x$ and $b = \cot\beta = q/k_y$, where α and β are the extremal elliptical cone angles. Then, for pristine graphene we have the values $\alpha = \beta = \pi/4$. With a and b independent of x, the equation (3.16) is reduced to the quantum harmonic oscillator equation. In the present case we obtain that the LLs spectra is given by

$$E_n = \mathrm{sgn}(n)\sqrt{ab}\hbar\omega^D\sqrt{|n|}, \quad \omega^D = v_F\sqrt{\frac{2eB}{\hbar}}, \tag{4.6}$$

with $n = 0, \pm1, \pm2, \ldots$ and degeneracy of $4S'B/(h/e)$, where S' is the deformed sample area. From equation (4.6), we can see that the strained graphene LLs depend on the geometrical

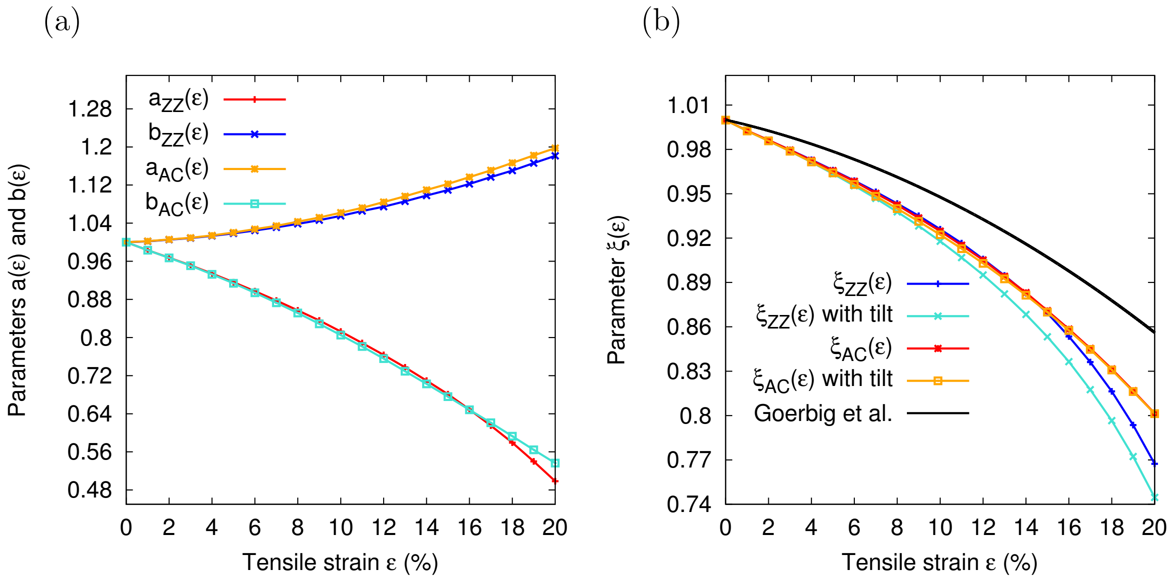

Figure 4.1: (a) Geometrical parameters a and b of the Dirac cone as a function of tensile strain (ϵ) along the AC and ZZ directions. (b) Evolution of the ξ parameter for strained graphene as a function of tensile strain (ϵ) along the AC (red line) and ZZ (blue line) directions with and without tilting of the Dirac cone axis. The black curve correspond to the renormalized Fermi velocity obtained from a TB approximation considering interactions up to second nearest neighbors in deformed graphene by Goerbig *et al.* [68].

parameters of the deformed Dirac cone, the respective cyclotron frequency ω^D and the quantum number n. Since the expressions (4.5) and (4.6) are similar, we have defined $\xi \equiv \sqrt{ab}$ as a parameter to measure the contraction ($\xi < 1$) or expansion ($\xi > 1$) of the LLs spectra under the same magnetic field. It should be noted that in others works, the concept of renormalized Fermi velocity v_F^* is commonly used [68], and which is related with our parameter by $v_F^* = \xi v_F$. It is important to mention that when the cross section of the Dirac cone does not have an exact elliptical form, it is necessary to solve the differential equation (3.16) to obtain the spectrum of LLs. In our best knowledge, there are not experimental reports on the effect of strain on the LLs spectra of graphene.

4.1.1 Discussion

We found that for both strain directions (AC and ZZ), in the whole range of studied deformations, the LLs spectra is contracted ($\xi < 1$) with respect to the pristine case ($\xi = 1$) under the same magnetic field. It is interesting to note that the value of ξ, and hence the distance between LLs, decrease as the uniaxial deformation is increased. This behaviour can be explained in terms of the cyclotron orbit motion change induced by strain. Thus, if graphene is stretched, the cyclotron orbit motion has a mean-radius bigger than the equilibrium case, then the value of total energy decreases. From this perspective, the expansion case in the LLs spectra may occur when graphene sample is contracted.

In Fig. 4.1, we show the plots of a, b and ξ for different values of deformation (ϵ) along the AC and ZZ directions. From Fig. 4.1 (a) we observe that for parameters $\epsilon < 10\%$, a (b) in ZZ (AC) has approximately the same values than b (a) in AC (ZZ). Thus, for a fixed value of deformation, the fitted cones for AC and ZZ are practically the same but one rotated with respect to the other by 90°. Therefore, the effect of AC and ZZ uniaxial strains on LLs is expected to be practically the same for strain up to 10%, as seen in Fig. 4.1 (b). This point can be explained if we consider that the parameter ξ represents the ratio between the renormalized Fermi velocity and the Fermi velocity in pristine graphene. The renormalized Fermi velocity can be seen as an effective velocity of the anisotropic Fermi velocity in the cyclotron motion. Considering that the cones have identical shape for AC and ZZ directions up to 10%, we expect similar values of the renormalized Fermi and similar contractions in the LLs spectra for both directions. Also, we observe that ξ has a nearly linear behaviour in this range of deformations, with $\xi \approx 1 - 0.7\epsilon$. This result suggests that the degree of deformation (ϵ) in a graphene sample can be estimated by extracting the value of ξ from the LLs spectra.

To evaluate the contribution of Dirac cone tilt on the contraction of LLs in uniaxially deformed graphene, we have fitted the conduction band using the dispersion relation of the form $E/\hbar v_F = a_o k_x + b_o k_y + \sqrt{a^2 k_x^2 + b^2 k_y^2}$, which is obtained diagonalizing the Weyl hamiltonian [24], where a_o and b_o are Dirac cone tilt parameters. With an appropriate rotation of our system, we can use the expression $\xi = \sqrt{ab}(1 - a_o^2/a^2 - b_o^2/b^2)^{3/4}$ [68], instead of $\xi = \sqrt{ab}$. In all cases we obtain $b_o \approx 0$, having a tilting only in the k_x-axis, in agreement with others authors [68]. The tilt can be neglected for strains up to 15% as seen in Fig. 4.1 (b), where the calculations of ξ with and without tilting are shown. For strains along the ZZ direction, the tilt could have observable effects on the LLs spectra for deformations larger than 15%. In order to compare the present results for ξ with previous calculations reported in the literature, in Fig. 4.1 (b) we include the result obtained from a TB effective model reported in [68], where a Harrison's scaling rule for the hopping parameters was used. We can see that the TB approximation predicts a descreasing behaviour of the renormalized Fermi velocity as a function of strain, in qualitative agreement with the DFT calculations. Nevertheless, there is an important quantitative difference, which can be attributed to the relaxation of carbon positions, and the Poisson ratio changes beyond of the elastic regime included in the DFT calculations. The contraction of LLs spectra as a function of the tensile strain is shown in Fig. 4.2, for both strain directions (AC and ZZ). As we can see, the contraction of LLs spectra for the ZZ deformation is larger than for the AC deformation. The LLs spectra does not present lifting of the two-fold valley degeneracy since our prediction is based in the low energy and low magnetic field regime [110, 115].

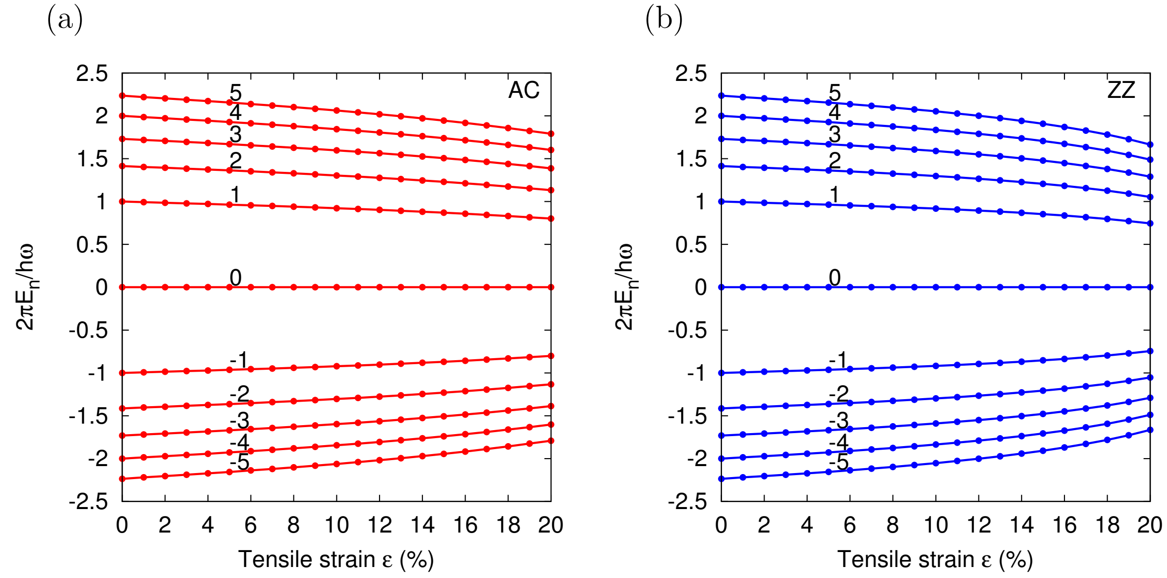

Figure 4.2: Evolution of the LLs spectra as a function of tensile strain along the (a) AC (red) and (b) ZZ direction (blue). The label in each curve corresponds to the Landau level (n).

In order to show the effect of strain on the LLs Density of State (DOS) under a uniform magnetic field, we have calculated the DOS for both strain directions with a deformation of 20%, and comparing them with the corresponding to pristine graphene under the same magnetic field. The DOS for strained graphene along the AC and ZZ directions are shown in Figs. 4.3 (a) and

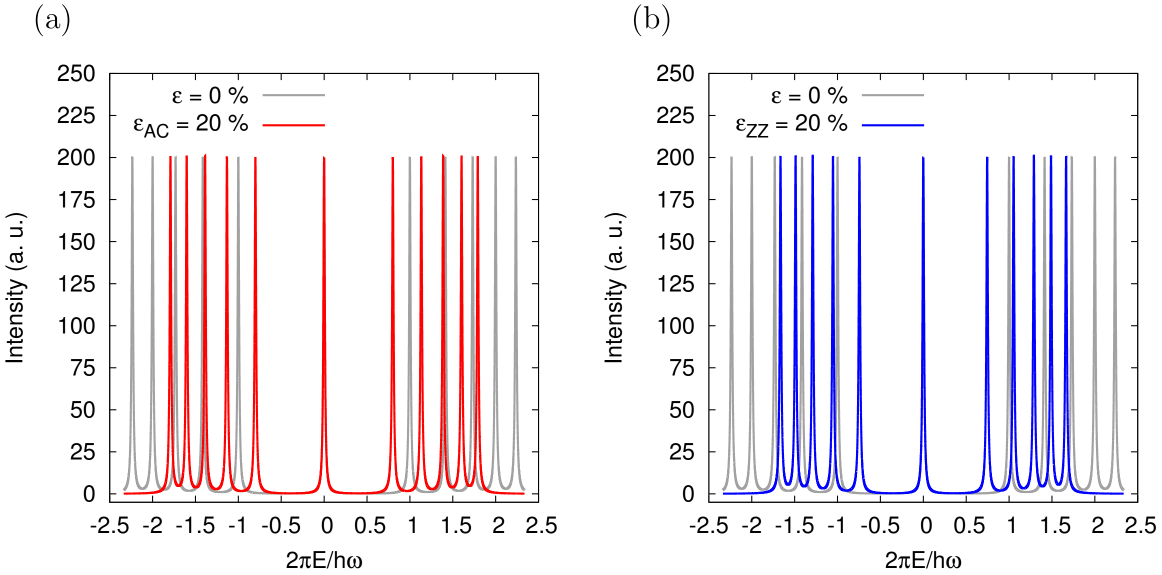

Figure 4.3: Calculated DOS of LLs for (a) pristine graphene (gray) and uniaxially strained along the AC direction (red) for deformation of 20% ($\xi_{AC} = 0.801$) and (b) pristine graphene (gray) and uniaxially strained along the ZZ direction (blue) for deformation of 20% ($\xi_{ZZ} = 0.745$).

4.3 (b), respectively. In these plots, we observe that the contraction of the LLs spectrum is larger along the ZZ than for AC direction, because $\xi_{ZZ} = 0.745$ and $\xi_{AC} = 0.801$ for $\epsilon = 20\%$. The DOS contraction with respect to equilibrium spectrum is a result of the LLs spacing reduction due to the Fermi velocity modulation by strain. Thus, the present results show clearly that the LLs spectra in graphene can be modulated via uniaxial strain.

4.2 Anisotropic massless Dirac fermions in homogeneously strained graphene

Most of the ground-electronic properties in anisotropic Dirac materials depend somehow with v_F: DOS is inversely proportional to the square of v_F, bulk compressibility is inversely dependent and LLs spectra depends linearly of it, as shown in Fig. 3.1 (b). Thus, the changes produced by the anisotropy on the Fermi velocity also are tailoring these physical quantities. Herein, we show how the strain, as anisotropy inductor mechanism, lead to a robust Fermi velocity behavior in graphene.

4.2.1 Geometrical Approach related with TB method

The TB description of anisotropic graphene-like system consists in a deformed hexagonal lattice with different bond lengths, hopping and overlapping parameters among nearest atoms. The anisotropy could have been induced through chemical manipulation or by loads upon the material. The lattice is conformed by two deformed triangular sublattices of Bravais identified as A and B. Thus, homogeneously strained graphene as an example of anisotropic graphene-like system, possesses a unit cell with two carbon atoms with decoupled p_z and σ orbitals. The lattice vectors are denoted by $\vec{a}_1$ and $\vec{a}_2$ and the reciprocal lattice vectors are given by $\vec{b}_1 = (2\pi/A_c)\vec{a}_2 \times \hat{z}$ and $\vec{b}_2 = (2\pi/A_c)\hat{z} \times \vec{a}_1$. The first Brillouin zone is a deformed hexagon having the symmetry points K and K'. In a TB calculation, $\vec{\delta_1}$, $\vec{\delta_2}$ and $\vec{\delta_3}$ indicate the positions of nearest neighbors on the underlying sublattice A. The set of t_j TB parameters with $j = 1, 2$ and 3 for nearest neighbors correspond to the probability amplitude that an electron hops to one of the three nearest atoms. Since the overlap terms and the next nearest neighbors hopping have a negligible contribution, TB hamiltonian is reduced to

$$H = \begin{bmatrix} 0 & g^*(\vec{k}) \\ g(\vec{k}) & 0 \end{bmatrix}, \tag{4.7}$$

where $g(\vec{k}) = t_1 \mathrm{e}^{-i\vec{k}\cdot\vec{\delta}_1} + t_2 \mathrm{e}^{-i\vec{k}\cdot\vec{\delta}_2} + t_3 \mathrm{e}^{-i\vec{k}\cdot\vec{\delta}_3}$. Solving the secular equation, we obtain the following eigenvalues of the hamiltonian (4.7):

$$E_\pm = \pm\sqrt{t_1^2 + t_2^2 + t_3^2 + 2t_1t_2\cos\theta_{12} + 2t_1t_3\cos\theta_13 + 2t_2t_3\cos\theta_{23}} \tag{4.8}$$

where $\theta_{ij} = \vec{k} \cdot (\vec{\delta}_i - \vec{\delta}_j)$. The eigenstates of (4.7) are $|\Psi(\vec{k})\rangle = \frac{1}{\sqrt{2}}(1, \pm\mathrm{e}^{\phi(\vec{k})})$ with $\phi = \arctan(\mathrm{Im}\{g(\vec{k})\}/\mathrm{Re}\{g(\vec{k}\}))$. Since the hamiltonian (4.7) has time-reversal symmetry, the Dirac points occur in pairs. Thus, the graphene band structure has Dirac points when the hopping parameters satisfy $|t_1 - t_2| \leq |t_3| \leq |t_1 + t_2|$. Otherwise, band gap is opened [14, 16, 11]. Solving $g(\vec{K}) = 0$, Dirac points are located at

$$K_x = \frac{a_{1y}\Lambda_1 - a_{3y}\Lambda_2}{|\vec{a}_1 \times \vec{a}_2|} \tag{4.9}$$

$$K_y = \frac{-a_{1x}\Lambda_1 + a_{3x}\Lambda_2}{|\vec{a}_1 \times \vec{a}_2|} \tag{4.10}$$

where $\vec{a}_3$ is defined as $\vec{a}_3 = \vec{a}_1 - \vec{a}_2$, Λ_1 and Λ_2 are functions of the hopping parameters

$$\begin{aligned}\Lambda_1 &= 2\arccos\left(-\sqrt{\frac{t_2^2-(t_1-t_3)^2}{4t_1t_3}}\right) && (4.11)\\ \Lambda_2 &= \arccos\left(\frac{t_1^2-t_2^2-t_3^2}{2t_2t_3}\right). && (4.12)\end{aligned}$$

The expressions (4.9) and (4.10) are a more general version that in [11, 16], where the deformation in lattice vectors have been explicitly included. In the low energy regime ($E << t = 2.7$ eV), we perform an expansion of $g(\vec{q}+\vec{K})$ around the Dirac point located at $\vec{K}$, preserving linear terms in $\vec{q}$:

$$g(\vec{q}) \approx \hbar v_F \vec{w}\cdot\vec{q}, \tag{4.13}$$

where the complex dimensionless vector $\vec{w}$ is expressed as

$$\vec{w} = (w_x, w_y) = \frac{2}{3t} i \sum_{j=1}^{3} \frac{\vec{\delta}_j}{a} t_j \mathrm{e}^{-i\vec{K}\cdot\vec{\delta}_j} \tag{4.14}$$

and a is the equilibrium C-C distance with a value of 1.42 Å in pristine graphene [22]. Equation (4.14) establishes the bridge between effective three-hopping TB model with GA, since the expansion (4.13) leads to

$$H = v_F \begin{bmatrix} 0 & w_x^* p_x + w_y^* p_y \\ w_x p_x + w_y p_y & 0 \end{bmatrix}, \tag{4.15}$$

where $\vec{p} = \hbar\vec{q}$ and $v_F = \frac{3at}{2\hbar}$ is the Fermi velocity in pristine graphene. The effective TB hamiltonian (4.15) is identical to the mapped hamiltonian by the transformation (3.1), when the complex coefficients w_x and w_y are written as $w_x = a_{11} + ia_{21}$ and $w_y = a_{12} + ia_{22}$. The present hamiltonian (4.15), useful for the study of homogeneously strained graphene properties with arbitrary strain directions, is a generalization of the Weyl-hamiltonian used in [24], which was developed using TB approach with two different hopping parameters to nearest neighbors. That Weyl hamiltonian is applicable for systems with quinoid-type deformation [24]. In order to complete the relation between the effective three-hopping TB model and the GA, the anisotropy matrix is obtained using (4.14)

$$A = \frac{2}{3ta}\sum_{j=1}^{3} t_j \begin{pmatrix} \delta_{jx}\sin(\vec{K}\cdot\vec{\delta}_j) & \delta_{jy}\sin(\vec{K}\cdot\vec{\delta}_j) \\ \delta_{jx}\cos(\vec{K}\cdot\vec{\delta}_j) & \delta_{jy}\cos(\vec{K}\cdot\vec{\delta}_j) \end{pmatrix}, \tag{4.16}$$

hence, the effective Fermi velocity is calculated from the anisotropy matrix (4.16) using (3.4), (4.9) and (4.10)

$$\begin{aligned}\xi &= \frac{v_F'}{v_F} = \frac{1}{3at}\sqrt{2|\vec{a}_1 \times \vec{a}_2|}\Big[(t_1+t_2+t_3)(-t_1+t_2+t_3) \\ &\quad (t_1-t_2+t_3)(t_1+t_2-t_3)\Big]^{1/4}, \end{aligned} \tag{4.17}$$

which is cyclic under index permutation. Thus, the changes in the physical properties of homogeneously strained graphene are governed by the two factors present in (4.17): the first is caused by the change of the unitary cell area $|\vec{a}_1 \times \vec{a}_2|$ when the lattice is strained. The second, is produced by the anisotropic hopping parameters. Both factors are function of the homogeneous strain tensor.

4.3 The bridge between hopping parameters and homogeneous strain

In previous chapters, we shown that the v_F-dependent physical properties can be tailored through Dirac cone parameters. In the above section, the relation of v_F' as a function of TB parameters was found. Thus, the completed relation between v_F-dependent physical observable and strain is given by the hopping scaling rule. We start studying the homogeneous deformations along an arbitrary direction θ with respect to a Cartesian system chosen with the x-axis along the ZZ direction. In elasticity theory [135], is always possible to separate the strain tensor in its isotropic and shear strain contribution

$$\mathbf{u} = \mathbb{I}\epsilon_i + \mathbf{S}\epsilon_s, \tag{4.18}$$

where $\epsilon_i = \frac{1}{2}(\epsilon_1 + \epsilon_2)$ and $\epsilon_s = \frac{1}{2}(\epsilon_1 - \epsilon_2)$ are the isotropic and shear strain contribution coefficients, being ϵ_1 and ϵ_2 the eigenvalues of the strain tensor. $\mathbb{I}$ is the 2×2 identity matrix and $\mathbf{S}$ is a matrix expressed as $\mathbf{S} = \sigma_z \cos 2\theta + \sigma_x \sin 2\theta$, with σ_x and σ_z the Pauli matrices. A vector $\vec{v}$ in the deformed lattice is expressed as $\vec{v} = (\mathbb{I} + \mathbf{u})\vec{v}^o$, with $\vec{v}^o$ a vector in the non-deformed lattice. In this way, the nearest neighbors position in the anisotropic hexagonal lattice, can be obtained from the initial configuration as $\vec{\delta}_j = (\mathbb{I} + \mathbf{u})\vec{\delta}_j^o$. The calculation of deformed bond lengths leads to

$$\frac{\delta_j}{a} = \sqrt{\left[1 + \epsilon_i + \epsilon_s \cos\left(2\theta + \tfrac{2j-1}{3}\pi\right)\right]^2 + \epsilon_s^2 \sin^2\left(2\theta + \tfrac{2j-1}{3}\pi\right)}. \tag{4.19}$$

Thus, the change in the bond lengths (4.19) modifies the hopping amplitudes among neighboring sites. Such variation is modeled as an exponential decay of t_j with the increase of δ_j [11, 76]

$$t_j = t\mathrm{e}^{-\beta_j\left(\frac{\delta_j}{a}-1\right)}, \tag{4.20}$$

where β_j are the Grüneisen parameters, which in principle might be different for each C-C bond and they dependent of the strain-type considered. In pristine graphene, β_j is the same for each bond and its value is $\beta = 3.37$ [126]. From ab-initio calculations was demonstrated that, for small uniaxial deformations along the AC and ZZ directions, the value of β remains approximately constant [60]. In the present work, we have assumed that for homogeneous strain $\beta_j \approx \beta$. The possible implications of considering $\beta_j \neq \beta$ will be discussed in the next section. Now, if we relate the expression $|\vec{a}_1 \times \vec{a}_2|$ with the homogeneous strain, we can complete the relation between ξ and $\mathbf{u}$. Then, trom the strain tensor trace, we have

$$|\vec{a}_1 \times \vec{a}_2| = 3\frac{\sqrt{3}}{2}a^2(1 + 2\epsilon_i). \tag{4.21}$$

Thus, substituting the expresions (4.20) and (4.21) in (4.17) the relation between the effective Fermi velocity and the homogeneous strain is found.

In order to study the renormalized effective Fermi velocity as a function of uniaxial, shear or strain combinations, we use the definitions for each considered strain. Since graphene has a linear elastic response for small deformations, ϵ_i and ϵ_s are proportional to the tensile strain parameter ϵ. Introducing p and q as the proportional constants for ϵ_i and ϵ_s respectively, we can define (p, q) as the label which identifies the strain. For instance, using the definitions of ϵ_i and ϵ_s in terms of strain tensor eigenvalues ϵ_1 and ϵ_2 in (4.18) for uniaxial strain, the label can be written as $(\frac{1}{2}(1-\nu), \frac{1}{2}(1+\nu))$. In a similar way, $(1, 0)$ and $(0, 1)$ denote the labels of pure isotropic and pure shear strain, respectively. In general, we have chosen p and q to be non-negatives. Hence, stretching and shrinking area is pointed out through the ϵ sign. We can see from (4.21) that for $\epsilon > 0$ the graphene sample is stretched. A negative value of ϵ indicates that the graphene sample has been shrunken. Nevertheless, the last interpretation

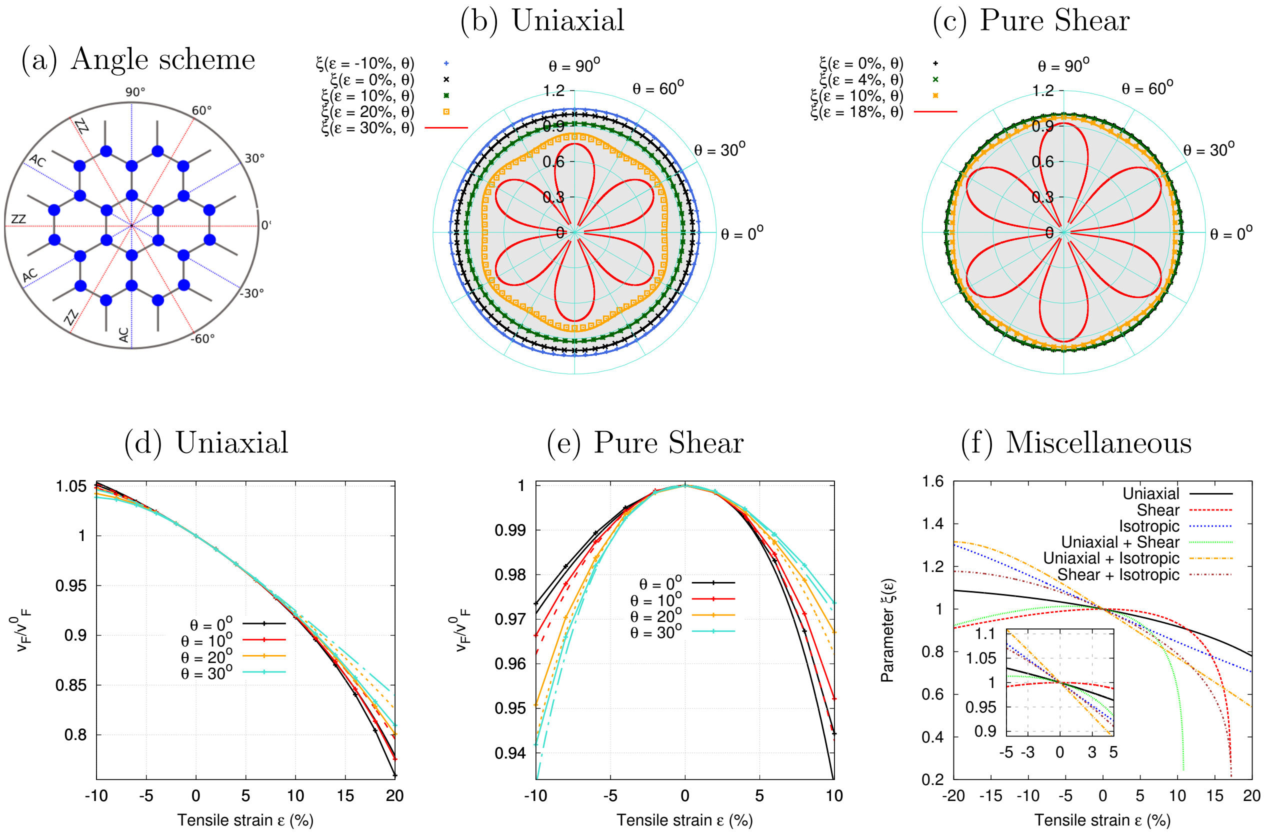
(a) Angle scheme
(b) Uniaxial
(c) Pure Shear
(d) Uniaxial
(e) Pure Shear
(f) Miscellaneous

Figure 4.4: Effective Fermi velocity as a function of ϵ and θ for uniaxial, shear, and combinations of strains. Solid lines with dots correspond to the calculated v'_F from the fitting of hopping parameters, whereas dash lines indicate the analytical calculation of v'_F using the hopping scaling rule. (a) Scheme of strain angles in graphene. (b) Uniaxial: ξ as a function of θ and for different values of tensile strain, $\epsilon = -12\%, -6\%, 0\%, 6\%, 12\%, 18\%$ and 25%. (c) Pure shear: v'_F as a function of θ and for different values of tensile strain, $\epsilon = 0\%, 7\%$ and 14%. (d) and (e), uniaxial and pure shear strain: v'_F as a function of ϵ and using the values $\theta = 0^o, 6^o, 12^o, 18^o, 24^o$ and 30^o. (f) Strain combinations for v'_F along the ZZ direction and in the inset the linear behavior of v'_F for small strain is shown.

has an exception for shear strain because the sample area do not change with ϵ. In that case, a positive (negative) ϵ must be interpreted as a stretching (shrinking) at length scale along the ZZ direction while in AC direction, the same quantity ϵ is shrunken (stretched).

4.3.1 Modulation of effective Fermi velocity with homogeneous strain

The application of specific (p, q) strains in graphene leads to different modulations of v_F. In order to confirm the effect of strain on v_F, two different methods were explored. On the one hand, the analytical function (4.17) is completely specified using the exponential scaling rule (4.20) and deformed bond lengths (4.19). Then, we evaluated for uniaxial, shear, isotropic and combinations in a tensile strain range $-10\% \leq \epsilon \leq 20\%$. On the other hand, the expression (4.17) was numerically evaluated avoiding the use of a scaling rule, using fitted hopping parameters from DFT calculations for uniaxial and shear strain.

Both methodologies are compared in Figs. 4.4 (b), (c), (d) and (e), where analytical (line) and numerical (dots) of effective Fermi velocity shown a good agreement. The maximum relative error is 2.4% for $\epsilon = 20\%$ with uniaxial strain along AC direction. For a better appreciation, Fig. 4.4 (a) shows the scheme of strain directions applied to a graphene sheet. This scheme is used for Figs. 4.4 (b) and (c), where the shaded and white areas are delimited with a circumference of unity radius indicating the decrease (shaded) or increase (white) of v_F. For uniaxial strain (see Fig. 4.4 (b)), we show a general behavior of v_F also valid for all homogeneous strain with $p \neq 0$, where v_F increases (decreases) if graphene is shrunken (stretched). While shear strain $(p = 0)$ in graphene makes that v_F always decreases, as shown in Fig. 4.4 (c). These effects of strain on v_F can be explained from geometrical arguments. A stretching (shrinking) of graphene causes that the extremal Dirac cone angle θ_1 increases (decreases) and for shear strain, it is only increased. Then, v_F behaves oppositely because $v_F \propto \tan^{-\frac{1}{2}} \theta_1$ from (3.6).

Isostrain curves with $\epsilon > 10\%$ evidence the periodicity and anisotropy of v_F. The period of $\frac{\pi}{3}$ corresponds to the hexagonal lattice symmetry. Thus, non repeated information is found at range $0 \leq \theta \leq \frac{\pi}{6}$. For $\epsilon \leq 10\%$, we found that v_F is isotropic, approximately. This indicates that v_F under strain has the same elastic behavior of graphene, since the qualitative description of v_F is analog to the stress-strain relationship [108]. This behavior is more evident plotting v_F as a function of ϵ in Figs. 4.4 (d) and (e). Thus, we can see that v_F changes between two limits given by v_F^- and v_F^+ which are the effective Fermi velocities along the ZZ and AC directions, respectively. For any (p, q) strain, simplified expressions of v_F^- and v_F^+ are obtained using the bond lengths (4.19), which are expanded to first order in ϵ along $\theta = 0$ (ZZ) and $\theta = \frac{\pi}{6}$ (AC):

$$v_F^{\pm} = v_F^0 \sqrt{1 + 2p\epsilon} \left(\frac{4}{3} \mathrm{e}^{\pm 3q\beta\epsilon} - \frac{1}{3} \right)^{1/4} \mathrm{e}^{-\beta(p \pm q)\epsilon}. \tag{4.22}$$

Hence, Figs. 4.4 (d) and (e) shown that the most efficient way to decrease (increase) v_F is stretching (shrinking) the ZZ bond which is given by v_F^- in (4.22). In constrast, the least efficient form occurs applying strain along the AC direction whose values are given by v_F^+.

In order to elucidate the role of p and q, we explore how v_F along the ZZ direction is affected combinating uniaxial, shear, and isotropic strain, as shown in Fig. 4.4 (f). Thus, higher values of q makes that v_F tends to zero for smaller tensile strains. There are two possibilities that $\xi(\epsilon, \theta) = 0$ in (4.17): whether the ideal transition from hexagonal lattice to one-dimensional atomic chain is achieved satisfying $|\vec{a}_1 \times \vec{a}_2| = 0$, or when the merging of Dirac points is reached. The last case is the reason of the zero of v_F in Fig. 4.4 (f). From (4.22) can be shown that this zero is given by $\epsilon_g^{min} = \frac{2 \ln 2}{3\beta q}$, where ϵ_g^{min} is also the minimum tensile strain for a gap threshold, being only tuned by the shear strain contribution q.

On the other hand, the effect of isotropic strain over the modulation of v_F is more evident for small strains, (see inset of Fig. 4.4 (f)). Thus, we expand the expression (4.16) to linear terms of ϵ, using the deformed bond lengths (4.19) and the scaling rule (4.20)

$$A = \begin{pmatrix} 1 + (1-\beta)(p + q\cos 2\theta)\epsilon & (1-\beta)q\epsilon \sin 2\theta \\ (1-\beta)q\epsilon \sin 2\theta & 1 + (1-\beta)(p - q\cos 2\theta)\epsilon \end{pmatrix}. \tag{4.23}$$

Calculating v_F from (3.4), we get

$$\frac{v_F'}{v_F} \approx 1 - (\overline{\beta} - 1)p\epsilon - \overline{\kappa}(\theta)q\epsilon, \tag{4.24}$$

where we define $\overline{\beta} = \frac{1}{3}\sum_j \beta_j$ and $\overline{\kappa}(\theta) = \frac{1}{3}\sum_j \beta_j \cos(2\theta + \frac{2j-1}{3}\pi)$. Since $\sum_j \cos(2\theta + \frac{2j-1}{3}\pi) = 0$, $\beta_j = \overline{\beta} + \Delta\beta_j$, and $\Delta\beta_j << 1$, the third term on the right side of (4.24) is negligible. The present result (4.24) is the consequence of use the anisotropic hopping scaling rule given by (4.20). Hence, v_F depends linearly of ϵ and the slope is given by $\overline{\beta}$ and p. We note that the decreasing (increasing) of v_F for $\epsilon > 0$ ($\epsilon < 0$) is more pronounced with higher values of p.

Accordingly, the modulation of all the v_F-dependent physical properties are enhanced using strain profiles with a strong isotropic strain contribution. A special emphasis is placed on the study of the strain effects on LLs spectra due to its linear dependency with v_F. Further, an experimental observation of v_F variation is factible through LLs measurements. Then, we show the evolution of LLs for uniaxial strained graphene along the ZZ direction and combinating uniaxial and isotropic strains in Fig. 4.5.

The expansion or contraction of LLs, which is an effect of the variation of v_F, can be explained from a physical and intuitive point of view. Strain induces the anisotropy in the hopping parameters causing a distortion of electron's orbits. Accordingly, the electron orbit average radius increases when graphene is stretched, reducing the separation between energy levels. Whereas the shrinking of graphene makes that the radius electron orbit increases and LLs spectra is expanded. An identical situation is found in the study of LLs in graphene under an in-plane electric field [118, 119, 120, 121]. In that system, the uniform electric field $E_{||}$ contracts the LLs spectrum. The separation between two underlaying levels decreases due to the competition between the electric (F_E) and magnetic (F_B) forces. Reaching the critical value $E_{||c}$, the LLs are collapsed and for $E_{||} > E_{||c}$ or equivalently $F_E > F_B$, the LLs quantization disappears by the opening of electron orbits. However, the LLs in homogeneously strained graphene do not have a collapse as the LLs in graphene in presence of an electric field. Although, in Fig. 4.4 (f) we see that Fermi velocity is vanished for some critical strains values, indicating an apparent collapse of LLs. This absence of collapse is due to the change of dependency of LLs with B in the merging of Dirac points [115]. Hence, a correct description of LLs near to the transition needs to involve the K and K' Dirac cones [13, 24, 109, 110].

Inspired by the experimental work performed for pristine graphene [3, 176], we propose how v_F could be indirectly measured through the DOS of LLs in homogeneously strained graphene. Since the stretching (shrinking) in graphene produces an expansion (contraction) on the LLs spectra, the variation of v_F could be evidenced from DOS experimental data. Figs. 4.5 (c) and (d) show the DOS of LLs spectra as a function of the tensile strain ϵ for the cases of uniaxial strain along the ZZ direction and the combination of uniaxial and isotropic strains. For $\epsilon = 5\%$, the combination of uniaxial and isotropic strain evidence a contraction of 23 % against to 8 % considering only uniaxial strain. Therefore, the value of v_F'/v_F can be more easily extracted from DOS measurements when the combination is considered. The experimental confirmation of linearly dependency of v_F for small strains could be used in the estimation of relevant constants

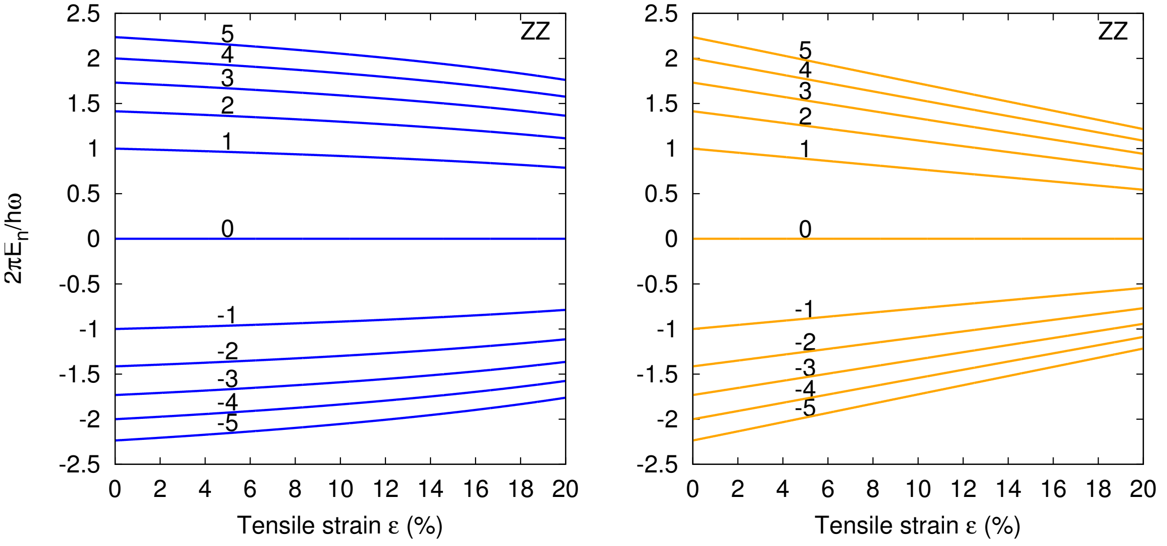

(a) LLs for uniaxial

(b) LLs for isotropic + uniaxial

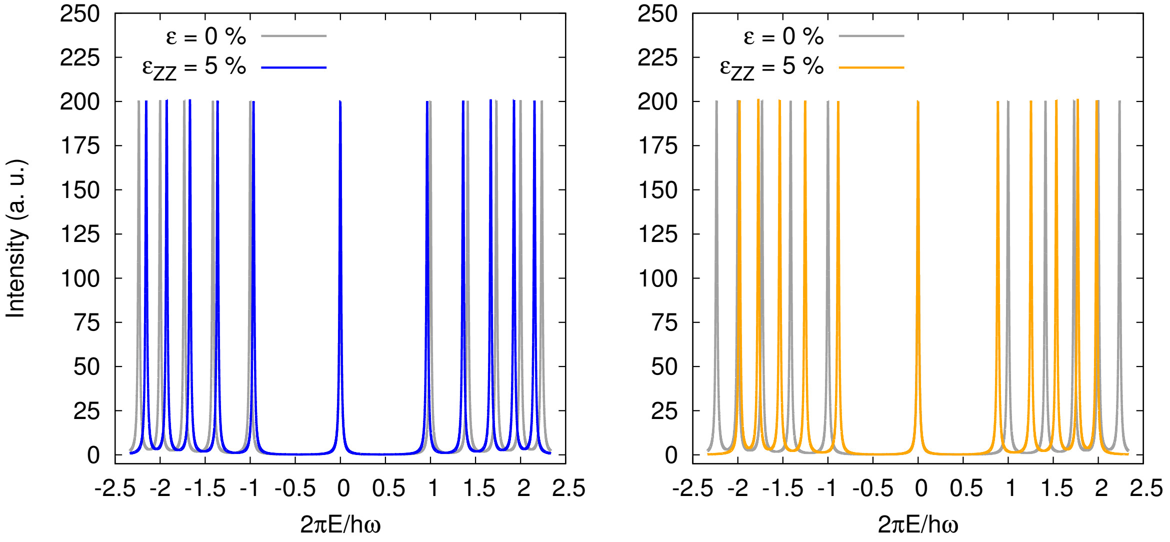

(c) DOS for uniaxial

(d) DOS for isotropic + uniaxial

Figure 4.5: Evolution of LLs in (a) uniaxial and (b) combination with isotropic strain in graphene along the ZZ direction as a function of tensile strain ($\epsilon > 0$). Calculated DOS for (a) uniaxial ZZ strain with $\epsilon = 7\%$ (blue) and for (b) a combination of uniaxial and isotropic strains with $\epsilon = 7\%$ (orange). The DOS for pristine graphene (gray) is included for references. Each peak corresponds to a Landau level of the series of eleven peaks shown.

in graphene and related DMs. For instance, the Grüneisen parameter can be obtained as $\overline{\beta} = 1 - \frac{m}{p}$, where m is the slope of (4.24) and $p = 1 + \frac{1}{2}(1 - \sigma)$ corresponds to the isotropic strain contribution of uniaxial and isotropic combination. Also, Poisson ratio is related with m

as $\sigma = 3 + \frac{2m}{\beta - 1}$.

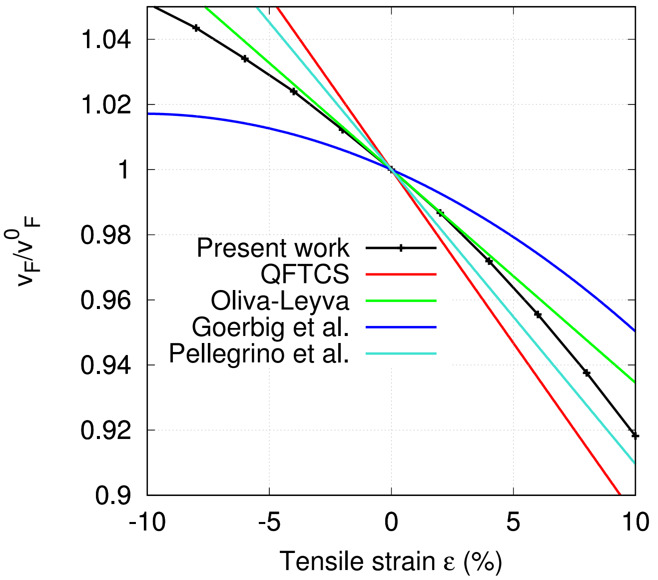

Figure 4.6: Effective Fermi velocity as a function of uniaxial strain along the ZZ direction obtained with the present approach and compared with the predicted by Amorim *et al.* [15], Oliva-Leyva and Naumis [38], Goerbig *et al.* [68], and Pellegrino *et al.* [98].

In order to compare with other approaches, we use the expression (3.4) for extracting the effective Fermi velocity of each reported model [15, 38, 39, 68, 98]. The comparison in Fig. 4.6, shows v'_F as a function of ϵ considering uniaxial strain along ZZ direction. Thus, the predicted Fermi velocity of QFTCS [15] has a slope given by $m = \frac{1}{2}\beta(1-\nu) = 1.45$ which differs with the estimated value $m \approx 0.7$ using DFT calculations. In [38], the scaling rule was expanded to first order in ϵ obtaining a similar result to the expression (4.24) with a good agreement for $\epsilon \leq 5\%$. We note that the effect of nonlinear ϵ terms must be included for tensile strains $\epsilon > 5\%$. On the other hand, in [68] was used the Harrison scaling rule $t_j \propto \frac{1}{\delta_j}$, where the expansion of v'_F for small strains has the form $v'_F/v_F \approx 1 - 0.33\epsilon$. In other model [98], the hopping scaling rule (4.20) was expanded to first order in ϵ where the lattice vectors deformation were neglected, obtaining $v'_F/v_F \approx 1 - 0.95\epsilon$. Accordingly, the differences of v'_F evidence that even for small strains, there are discrepancies among effective models predicting the effect of strain on physical properties. Hence, Fermi velocity measurements are needed for the corroboration of models. LLs spectroscopy is an option that we propose as test of these effective approaches.

4.4 Topological validity of the Geometrical Approach for homogeneous strain

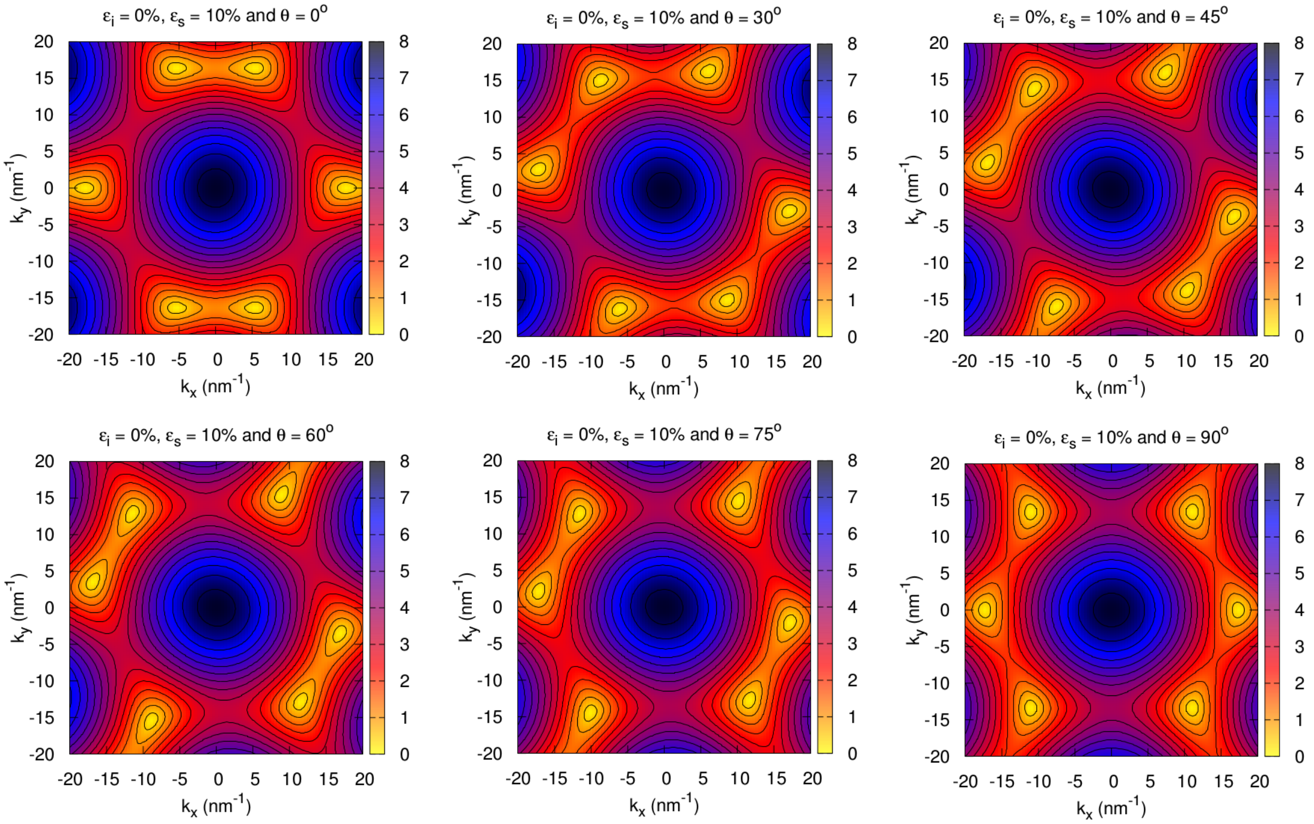

Figure 4.7: Colour maps of the energy landscape for shear strained in graphene with $\epsilon = 10\%$. Top: left to right for rotation angles $\theta = 0^o, 30^o$ and 45^o. Bottom: left to right $\theta = 60^o, 75^o$ and 90^o.

Using the hopping scaling rule (4.20) and the new nearest atomic positions of the current configuration in the dispersion relation (4.8), we can observe how the strain distortes the energy landscape, as shown in Fig. 4.7. Contour curves around Dirac point evolves from an elliptical to a more complex shape when the energy is increased. Applying strain in a different direction to ZZ and AC, the energy landscape has always a special direction where the merging of Dirac points can be reached increasing the tensile parameter.

In order to examine the topological validity of the GA for homogeneously strained graphene, we use the hopping scaling rule (4.20) and the deformed bond lenghts (4.19) looking for critical strains values for the merging of Dirac points. Strain modulation could lead to a topological phase transition from a semimetallic to insulator phase [11, 14, 16]. Although, DFT calculations have probed that such transition could not be possible. This is because the σ band pushes down preventing the gap near the critical strains [46]. Herein, we will use the merging of Dirac points condition $|t_1 - t_3| = t_2 = |t_1 + t_3|$ searching the strain range where ϵ_i, ϵ_s and θ indicate the topological validity of the GA for homogeneously strained graphene. Thus, we expanded (4.19) preserving the linear terms and we substitute the exponential decay rule on merging of Dirac points condition $t_2 = t_1 + t_3$, obtaining

$$\epsilon_s \cos 2\theta = \tfrac{2}{3\beta} \ln \left[2 \cosh \left(\tfrac{\sqrt{3}}{2} \beta \epsilon_s \sin 2\theta \right) \right] , \tag{4.25}$$

which is ϵ_i-independent. Hence from a linear dependency of the bond lenghts with strain, we observe that the shear strain contribution ϵ_s is only responsible of a Dirac cone merging. The others Dirac merging condition $t_1 = t_2 + t_3$ and $t_3 = t_1 + t_2$ lead to an identical equation (4.25) rotated $\pi/3$ and $2\pi/3$, and together with (4.25) are the equations of the hyperbolas, as shown in Fig. 4.8. The hyperbolas delimit the region having Dirac points, which corresponds to the semimetallic phase predicted by TB, while the outside region is the insulator phase. Thereby, the topological validity of the GA for homogeneously strained graphene is represented by the colour region in Fig. 4.8 (a). Thus, we can see that for $\theta = 0$, the minimum strain needed to reach the topological transition occurs with a critical value of $\epsilon_s \approx 0.14$. This value coincides with the predicted for gap opening in graphene by shear strain [59]. Whereas in uniaxial strain, the critical value is $\epsilon_s = \frac{1}{2}(1+\nu)\epsilon = 0.14$. In the same way, the critical value of $\epsilon \approx 0.24$ matches with the reported [11]. On the other hand, straining along the AC directions, the topological transition seems impossible to perform. A more exact calculation considering nonlinear terms in (4.19) is required to confirm the impossibility of transitions along AC directions.

An examination of the whole possible values within topological validity for extremal elliptical cone angles θ_1 and θ_2, as well as the Dirac point location (K_x, K_y), reveals how the geometrical parameters are modulated by homogeneous strain. Fig. 4.8 shows these quantities for the specific case of shear strain. The Dirac point location and extremal elliptical cone angle θ_1 are delimited by the hyperbolas found with the merging of Dirac points condition (4.8). Whereas θ_2 is not affected by the TPT because this extremal angle still remains when the transition is completed. Once more, the influence of strain-stress relationship can be also observed on the

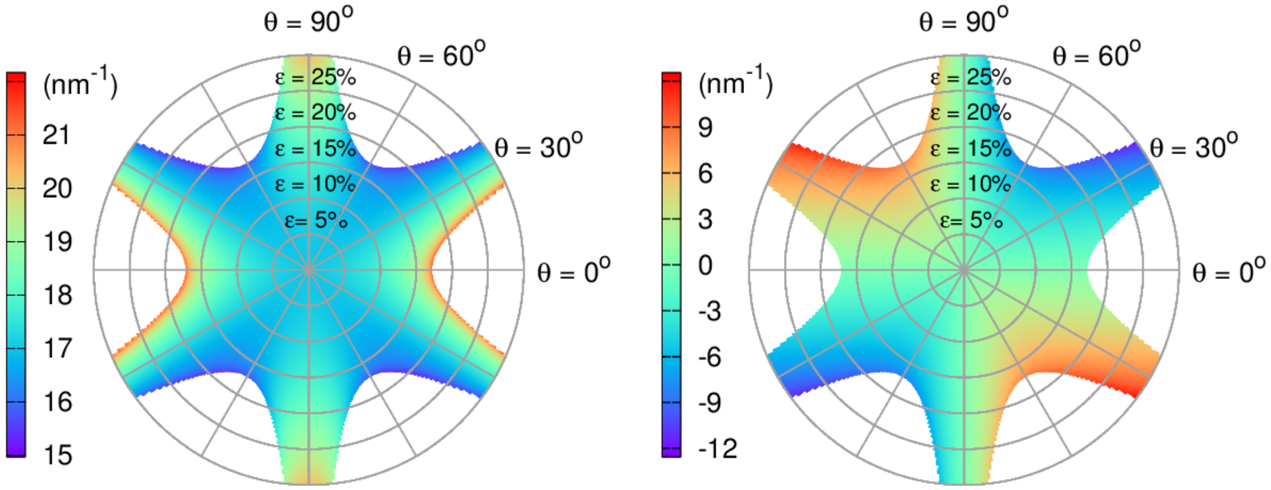

(a) K_x component

K_y component

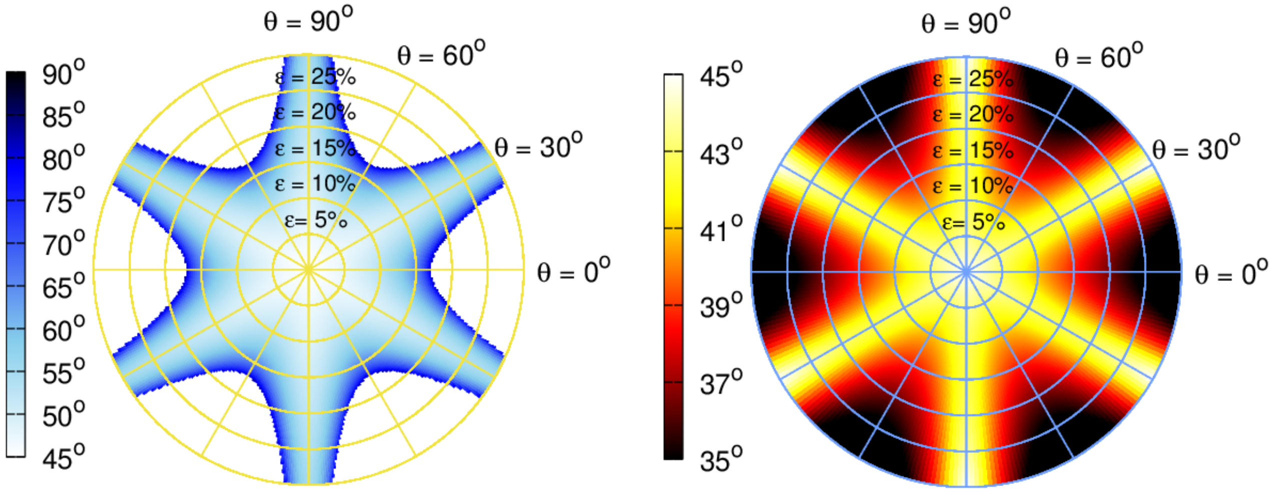

(c) θ_1 Dirac cone parameter

(d) θ_2 Dirac cone parameter

Figure 4.8: GA parameters as a function of shear strain within topological validity. The hyperbolas obtained using the merging of Dirac points condition, delimite the colour region where GA is valid in the semimetallic phase of graphene. Outside of them, TB predicts an insulator phase and the transition occurs when the hyperbola is crossed with the increase of ϵ_s in a specific θ direction. The minimum ϵ_s for a TPT is given along the ZZ direction. The colour map in (a) and (b) correspond to the K_x and K_y components of Dirac point position values. (c) and (d) show the whole allowed values for θ_1 with topological validity of the GA, while θ_2 does not have a topological restriction.

Dirac cone parameters. We note that with strains up to 10%, the change in the values of K_x, K_y, θ_1 and θ_2 are small and approximately the same that for pristine graphene. Further, these parameters have a linear and isotropic behavior for $\epsilon \leq 10\%$. The imposed tendency by the strain-stress relationship on the Dirac cone parameters is completed for $\epsilon > 10\%$, nonlinear and anisotropic behavior appear. Therefore, a strong variation on the Dirac point location and eccentricity of Dirac cone with respect of pristine values can be observed in proximity to the merging of Dirac points.

The strain effect on the Dirac cone parameters can be an useful information for the designing of devices based in strain-engineering, and modulation of physical properties. An example is given with the implementation of AMDFs optics in homogeneously strained graphene.

4.5 Electron Quantum Optics in Homogeneously Strained Graphene

The implementation of an electron quantum optics with AMDFs can be obtained from the building of homogeneously strained graphene systems. Unconventional optics devices described in the previous chapter can be designed using two different homogeneously strained graphene regions. These devices can be developed in strained graphene due mainly to the singular effect of strain on the electronic band structure. The use of two strained reciprocal regions allow a relative sideshift among Dirac cones, which are caused by the different location of Dirac points. Further, the intrinsic rotation of elliptical Dirac cone changes the habitual reflection law and KT. These essential elements given by the strain engineering in graphene make possible the development of an optics of AMDFs.

Indeed, a collimator as the illustrated in Fig. 3.3 (c), can be designed applying a shear strain of $\epsilon = 15\%$ along the $\theta = 0^{\circ}$ direction in the region I. With these set of strain values, we can see in Fig. 4.8 (c) and (d) that the corresponding Dirac cone parameters are $\theta_1 \approx 80^{\circ}$ and $\theta_2 \approx 36^{\circ}$. The region II could not be strained. Thus, collimation effect can be obtained for energies $E << V_0$. For the valley-dependent collimation showed in Fig. 3.3 (f), the region I can be set with the same strain values that the previous case. While in the region II, the used shear strain has the values of $\epsilon = 15\%$ and $\theta = -30^{\circ}$. Then, the shifting of Dirac points is

$\Delta K = 0.6$ nm^{-1} obtaining the split of AMDFs from K^+ and K^- valleys. On the other hand, the design of a valley beam splitter can be performed using the set of shear strain parameters in the region I (II) as $\epsilon = 11\%(13\%)$, $\theta = 60^o(70^o)$, $V = V' = 0$ mev and $E = 230$ meV. In this way, valley filter is obtained with the set of values in the region I (II) as $\epsilon = 13\%(13\%)$, $\theta = 45^o(65^o)$, $V = V' = 0$ mev and $E = 80$ meV.

The Veselago lenses showed in Fig. 3.6, can be fabricated using a fully strained graphene sheet, where the focusing condition is given by $E = V_0/2$. A simplified version of the asymmetric Veselago lens is reached straining the graphene sheet along a direction $\theta \neq 0, \frac{\pi}{2}$. For this device, KT shows an angular shifting. Symmetric Veselago lenses are obtained when graphene is strained along $\theta = 0$ or $\frac{\pi}{2}$ direction. The obtention of a symmetric super divergent lens (see Fig. 3.7) requires the application of a strain along ZZ (AC) direction in the region I (II) or vice versa. In the diverging condition $E = V_0(1 - \lambda_1'\lambda_2'w/\lambda_1\lambda_2 w')^{-1}$, super KT of AMDFs is also predicted. Asymmetric super divergent lens is obtained when the strains in the region I and II have the same K_y component for the Dirac points.

4.6 Klein tunneling in homogeneously strained graphene

In order to emphasize how the Dirac cone distortion also affects the KT, we study the transmission of Dirac fermions crossing a potential barrier in fully strained graphene, as shown in Fig. 4.9. Since the three regions are identically deformed, the Dirac cones show the same position at reciprocal lattice. Thus, the refraction of AMDFs is valley independent. Under these considerations, other approaches which only considered the strain effects through a pseudo vector potential, predict that the KT of AMDFs does not have some difference with pristine graphene. In contrast, the study of KT from the GA allows us to prove that the Dirac cone distortion changes drastically the transmission of Dirac fermions. In the present case, the AMDFs Snell's law (3.18) in fully strained graphene is written as

$$\lambda_2 \sin\theta_R \cos\chi + \lambda_1 \cos\theta_R \sin\chi = \frac{ss'|E - V'|}{|E|}(\lambda_2 \sin\theta_R \cos\chi' + \lambda_1 \cos\theta_R \sin\chi'). \tag{4.26}$$

where χ and χ' are related with the angles of incidence θ and refraction θ', respectively in (3.19). Using the matching conditions for the wavefunctions in each region, we obtain the same form

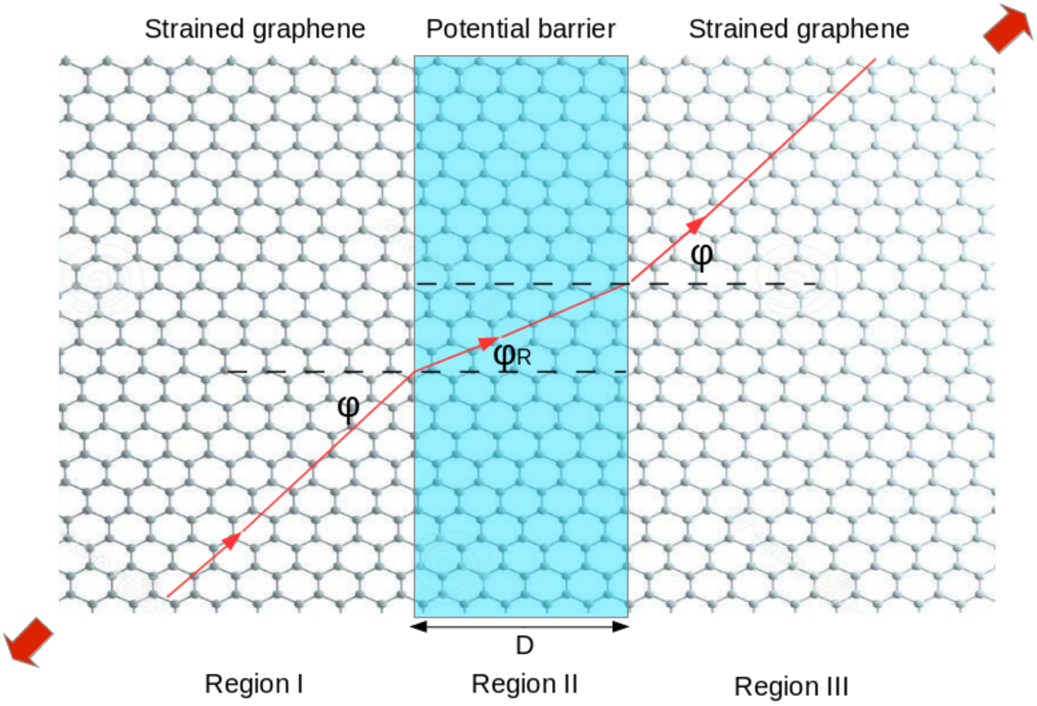

Figure 4.9: Klein tunneling of electrons through a potential barrier in fully strained graphene. The turquoise area denotes the region positively doped in the energy range where the dispersion relation is lineal. The red wide arrows indicate the direction where a strain is applied to graphene. The oriented path shows how the electron beams coming from region I are refracted inside the barrier, and later the beams outcoming at region III.

of the transmission probability coefficient of pristine graphene

$$T(\phi) = \frac{\cos^2\phi\cos^2\phi'}{\cos^2\phi\cos^2\phi'\cos^2(q_xD) + (1 - ss'\sin\phi\sin\phi')^2\sin^2(q_xD)}, \tag{4.27}$$

where D is the potential barrier width. The wavefunction's phases ϕ and ϕ' are expressed in terms of θ and θ' using $\phi = \alpha + \chi(\theta)$. In this way, the transmission probability is completely specified as a function of θ and E. An example system is set up with a barrier width $D = 100$ nm and height of $V = 200$ meV. In particular, we show how the strain modifies the KT and Fabry Perot interference when graphene has an applied shear strain of 16% along ZZ, with $\theta = \frac{\pi}{3}$, and AC directions. In fig 4.10 (a) is shown $T(E, \theta)$ for pristine graphene in the range of energies 50-100 meV. The extended red area indicates the values of E and θ where the potential barrier is transparent and for normal incidence the KT occurs. While in other angles of incidence, the perfect transmission is reached due to the Fabry-Perot resonances $q_x D = n\pi$. When a shear strain is applied in the fully graphene sheet, $T(E, \theta)$ has a drastic change in the KT and the Fabry-Perot interferences, as shown in Fig. 4.10 (b), (c) and (d). These figures have the same range of E and θ as in the nondeformed case. We can see in Fig. 4.10 (b) that the potential barrier becomes transparent for a wide range of θ and the absence of backscattering along the normal incidence persists. This can be explained from the kinematical construction, since the Dirac cone transversal section has a similar shape to the shown in Fig. 3.6 (e). Thus, the narrow range for q_y makes that the KT condition can be approximately satisfied for a wide range of incidence. Furthermore, the resonances are increased due to the widened range of q_x. Stretching along the AC direction, the complementary effect is noted in Fig. 4.10 (c). This effect occurs because the Dirac cone transversal section rotates $\frac{\pi}{2}$. Then, the range of q_x (q_y) is decreased (increased) obtaining a narrowed range of θ for the transparency of potential barrier.

So far, the KT seems to be unaffected when graphene is strained. However, the application of strain along a different direction of the aforementioned, generates the angular shifting of KT and the asymmetry of Fabry-Perot resonances, (see Fig. 4.10 (d)). Such behavior can be explained through the concept of pseudospin sublattice: when graphene is strained along ZZ or AC direction, the pseudospin is aligned with the group velocity under normal incidence. In the present case, the deformation of graphene along a different direction ZZ and AC direction causes an intrinsic rotation of the Dirac cone. Hence, the pseudospin conservation is shifted for $\theta \neq 0$, and the asymmetry of Fabry-Perot interference emerges due to the breaking of the mirror symmetry under the operation $q_y \to -q_y$.

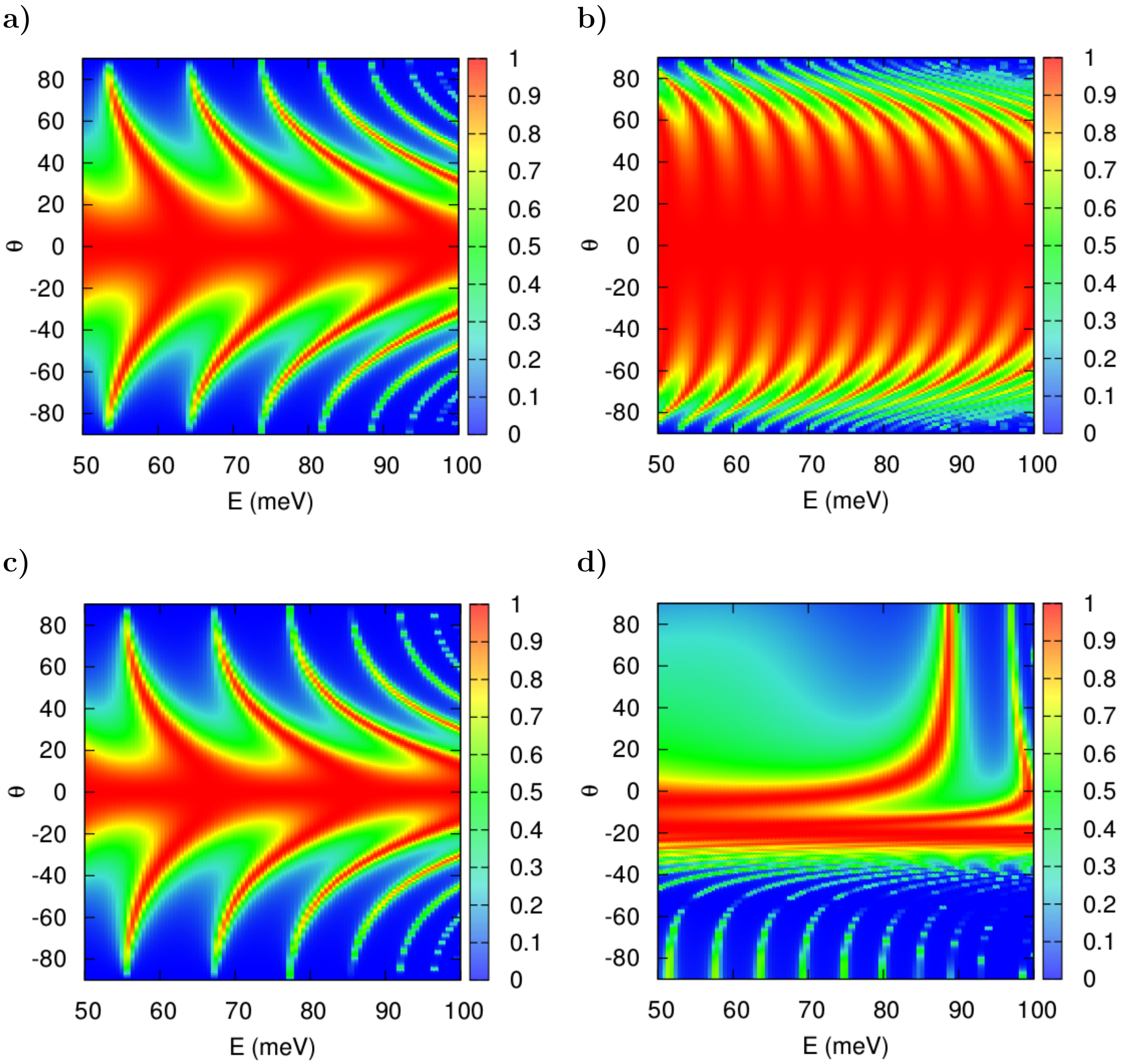

Figure 4.10: Transmission probability as a function of E and θ using a potential barrier width $D = 100$ nm and height $V = 200$ meV in all studied cases: pristine graphene in (a), shear strain in graphene where a tensile strain of 16% is applied along the ZZ (b), AC (c), and $\frac{\pi}{3}$ (d) direction.

Conclusions

- We have developed a novel model called Geometrical Approach to the study of anisotropic Dirac materials, which considers the geometry of the Dirac cones, applying a canonical transformation of linear momentum on the Dirac-like hamiltonian. The matrix associated with the canonical transformation, called anisotropy matrix, possesses all the relevant physical information of the system, having a direct relation with the Fermi velocity tensor, the rotation pseudospin operator, and the renormalization of linear momentum.

- We show that the Geometrical Approach offers a direct way to relate electronic, vibrational and transport properties with the geometry of anisotropic Dirac cones. Further, the parameters can be obtained using TB method, DFT calculations or experimental data, presenting a great versatility with respect to other models and removing the group velocity indeterminacy at Dirac point.

- We demonstrate that the effective Fermi velocity is related with the extremal angles that define the elliptical Dirac cone. Since most of the physical quantities in anisotropic Dirac materials are Fermi velocity dependents, they also are function of the Dirac cone parameters. Thus, the electronic, optical and transport properties can be tuned using the anisotropy as the induction mechanism via the effective Fermi velocity. An example was shown with homogeneous strain in graphene, where we evidence how the modulation of Fermi velocity induces the contraction or expansion of Landau levels spectra.

- The modulation of Landau levels spectra help to set a novel spectroscopy in Dirac materials, which could be used to measure quantities of interest as the Fermi velocity, Hall resistance and related electronic properties, as well as solve discrepancies among models about the prediction of Fermi velocity in strained graphene.

- We proposed the development of electron quantum optics in anisotropic Dirac materials based on a generalized reflection and Snell's law for massless Dirac fermions, embodying the negative refraction which is useful in the design of Veselago lenses, and the valley-dependent refraction of relevance in the generation of beam splitters and filters. We have shown that the optics of anisotropic massless Dirac fermions offers a wide variety of phenomenologies, like super diverging particles flow, omnidirectional Klein tunneling, and asymmetrical Veselago lenses. Using homogeneously strained graphene as an example of an anisotropic Dirac material, we show the feasibility to improve and design novel electron quantum optics devices.
- We evidence the importance of Dirac cone distortion on the Klein tunneling in fully strained graphene, showing how the strain changes the resonance peaks and suppresses the Klein tunneling when the pseudospins are rotated.

Future work

- The study of Klein tunneling of massive pseudospin one particles, (in progress).
- The emergence of pseudo-magnetic fields in spatial inhomogeneous systems using the Geometrical Approach.
- Electron dynamics of anisotropic Dirac materials with Rashba or electron-electron interactions.
- Hong-Ou-Mandel interference of anisotropic massless Dirac fermions.
- Quantum Goos-Hanchen effect in anisotropic Dirac materials.
- The development of super divergent lenses in light optics.
- The study of Landau levels and electron quantum optics in other anisotropic Dirac materials.
- The study of superconductivity in Dirac materials.

Appendix

Appendix A: Outstanding developments in the Geometrical Approach

A1: Equivalence between the Weyl hamiltonian $\mathbf{H_W}$ and the mapped Dirac hamiltonian $\mathbf{H(\tilde{p}\ ')}$

We can prove that the obtained hamiltonian $H(\vec{p}\ ')$ from the transformation (3.1) is the same that the 2D generalized Weyl hamiltonian H_W without the tilt velocity term [24], of the following way

$$\begin{aligned} H(\vec{p}\ ') &= v_F \vec{\sigma} \cdot \vec{p}\ ' \\ &= v_F \vec{\sigma} \cdot A\vec{p} \\ &= v_F \{\sigma_x(a_{11}p_x + a_{12}p_y) + \sigma_y(a_{21}p_x + a_{22}p_y)\} \\ &= v_{ij}\sigma_i p_j = H_W. \end{aligned}$$

Where the Fermi velocity tensor is related with the anisotropy matrix elements as $v_{ij} = v_F a_{ij}$.

A2: Symplectic or anti symplectic group condition

We show that the defined transformation $S = \xi^{-1}A$ with $\xi = \sqrt{|\mathrm{det}A|}$ is symplectic (anti symplectic), if $\mathrm{det}A > 0$ ($\mathrm{det}A < 0$). Since the Jacobian of the transformation $\vec{p}_c = S\vec{p}$ is

$M = S$, we have for the product of matrices

$$\begin{aligned} M^T J M &= \xi^{-2} \begin{pmatrix} a_{11} & a_{21} \\ a_{12} & a_{22} \end{pmatrix} \begin{pmatrix} 0 & 1 \\ -1 & 0 \end{pmatrix} \begin{pmatrix} a_{11} & a_{12} \\ a_{21} & a_{22} \end{pmatrix} \\ &= \xi^{-2} \begin{pmatrix} a_{11} & a_{21} \\ a_{12} & a_{22} \end{pmatrix} \begin{pmatrix} a_{21} & a_{22} \\ -a_{11} & -a_{12} \end{pmatrix} \\ &= \xi^{-2}(a_{11}a_{22} - a_{12}a_{22}) \begin{pmatrix} 0 & 1 \\ -1 & 0 \end{pmatrix} \\ &= \frac{\det A}{|\det A|} J = \mathrm{sgn}(\det A) J, \end{aligned}$$

where $\mathrm{sgn}(\det A) = 1$ indicates that S is symplectic and for $\mathrm{sgn}(\det A) = -1$, S is anti symplectic.

A3: Invariance of the commutation relations

We have ensured that $\vec{p}_c$ is a conjugated linear momentum for symplectic transformations, because the commutation relations $[x_i, p_j]$ do not change if we transform the position operator as $\vec{r}_c = (S^{-1})^T \vec{r}$. Calculating $[x_c, p_{xc}]$, we obtain

$$\begin{aligned} [x_c, p_{xc}] &= \xi^{-2}[a_{22}x - a_{21}y\ , a_{11}p_x + a_{12}p_y] \\ &= \xi^{-2}(a_{11}a_{22}[x, p_x] - a_{12}a_{21}[y, p_y]) \\ &= \mathrm{sgn}(\det A) i\hbar, \end{aligned}$$

for symplectic transformations, the commutator of x_c and p_{xc} remains invariant. While for anti symplectic transformations $[x_c, p_{xc}] = -i\hbar$, we obtain for $[x_c, p_{yc}]$

$$\begin{aligned} [x_c, p_{yc}] &= \xi^{-2}[a_{22}x - a_{21}y\ , a_{21}p_x + a_{22}p_y] \\ &= \xi^{-2}(a_{21}a_{22}[x, p_x] - a_{21}a_{22}[y, p_y]) \\ &= 0. \end{aligned}$$

Using $y_c = \xi^{-1}(-a_{12}x + a_{11}y)$, we obtain $[y_c, p_{yc}] = \mathrm{sgn}(\det A) i\hbar$ and $[y_c, p_{xc}] = 0$.

A4: Anisotropy matrix decomposition

In order to obtain the decomposition $A = R(-\alpha)D(\lambda_1, \lambda_2)R(\theta_R)$, we must note that the rotation of $\vec{p}$ and the scaling of axes lead to a rotated elliptical cone in the momentum space

$$\begin{aligned}
\vec{\tilde{p}} &= D(\lambda_1, \lambda_2)R(\theta_R)\vec{p} \\
&= \begin{pmatrix} \lambda_1 & 0 \\ 0 & \lambda_2 \end{pmatrix} \begin{pmatrix} \cos\theta_R & \sin\theta_R \\ -\sin\theta_R & \cos\theta_R \end{pmatrix} \begin{pmatrix} p_x \\ p_y \end{pmatrix} \\
&= p \begin{pmatrix} \lambda_1 \cos(\theta - \theta_R) \\ \lambda_2 \sin(\theta - \theta_R) \end{pmatrix}
\end{aligned}$$

where p_x and p_y were expressed in polar coordinates. The magnitude of $\vec{\tilde{p}}$ is the rotated elliptical cone equation in (3.7). On the other hand, the unitary transformation $U(\alpha) = \cos(\alpha/2)\mathbb{I} + i\sin(\alpha/2)\sigma_z$ produces a rotation around z axis in the SU(2) space

$$\vec{\sigma}_r = U^\dagger(\alpha)\vec{\sigma}U(\alpha) = R(\alpha)\vec{\sigma}.$$

With these considerations, the transformation of the Dirac hamiltonian $H(\vec{p})$ is written as

$$\begin{aligned}
H &= v_F \vec{\sigma}_r \cdot \vec{\tilde{p}} \\
&= v_F \{R(\alpha)\vec{\sigma}\} \cdot D(\lambda_1, \lambda_2)R(\theta_R)\vec{p} \\
&= v_F \vec{\sigma} \cdot R^T(\alpha)D(\lambda_1, \lambda_2)R(\theta_R)\vec{p} \\
&= v_F \vec{\sigma} \cdot A\vec{p},
\end{aligned}$$

where $A = R(-\alpha)D(\lambda_1, \lambda_2)R(\theta_R)$ since $R^T(\alpha) = R(-\alpha)$. Setting $\alpha = -\frac{\pi}{2}$, $\lambda_1 = \lambda_2 = 1$ and $\theta_R = 0$, we have $A = J$ and the Rashba hamiltonian is obtained

$$\begin{aligned}
H_R &= v_F \vec{\sigma} \cdot J\vec{p} \\
&= v_F(\sigma_x p_y - \sigma_y p_x) \\
&= v_F(\vec{\sigma} \times \vec{p}) \cdot \hat{z}.
\end{aligned}$$

A5: Hermiticity of $\tilde{\mathbf{p}}\,'$ and $\mathbf{H}(\tilde{\mathbf{r}}, \tilde{\mathbf{p}}\,')$

Using the properties of hermitian conjugated matrices, the hermiticity of $\vec{p}\,'$ in (3.8) and $H(\vec{r}, \vec{p}\,')$ in (3.10) are proved

$$\begin{aligned}
\vec{p}\,'^{\dagger} &= \left\{\frac{1}{2}\Lambda(\vec{r})\vec{p} + \frac{1}{2}(\Lambda(\vec{r})\vec{p})^{\dagger}\right\}^{\dagger} \\
&= \frac{1}{2}(\Lambda(\vec{r})\vec{p})^{\dagger} + \frac{1}{2}\left\{(\Lambda(\vec{r})\vec{p})^{\dagger}\right\}^{\dagger} \\
&= \frac{1}{2}(\Lambda(\vec{r})\vec{p})^{\dagger} + \frac{1}{2}\Lambda(\vec{r})\vec{p} = \vec{p}\,'.
\end{aligned}$$

With the above result, the mapped hamiltonian is hermitian

$$H^{\dagger} = v_F\{\vec{\sigma}\cdot\vec{p}\,'\}^{\dagger} = v_F\vec{p}\,'^{\dagger}\cdot\vec{\sigma}^{\dagger} = v_F\vec{\sigma}\cdot\vec{p}\,' = H.$$

Likewise, we prove that the transformation (3.8) is a generalization of the homogeneous anisotropy transformation (3.1) when λ_{ij} are constants

$$\begin{aligned}
\vec{p}\,' &= \frac{1}{2}\Lambda\vec{p} + \frac{1}{2}(\Lambda\vec{p})^{\dagger} \\
&= \frac{1}{2}\Lambda\vec{p} + \frac{1}{2}\vec{p}^{\,\dagger}\Lambda^{\dagger} \\
&= \frac{1}{2}\Lambda\vec{p} + \frac{1}{2}\Lambda^{*}\vec{p} \\
&= \frac{1}{2}(\Lambda + \Lambda^{*})\vec{p} \\
&= \Lambda_R\vec{p} = A\vec{p}.
\end{aligned}$$

A6: Complex gauge field $\tilde{\mathbf{A}}$

Since $\lambda_{ij}(\vec{r})$ is spatially dependent, a complex gauge field $\vec{A}$ has emerged as consequence of the hermiticity of $\vec{p}\,'$ and the noncommutativity of $\vec{r}$ and $\vec{p}$. The expression of $\vec{A}$ in terms of $\lambda_{ij}(\vec{r})$ is obtained from (3.8)

$$\begin{aligned}
\vec{p}\,' &= \frac{1}{2}\Lambda(\vec{r})\vec{p} + \frac{1}{2}(\Lambda(\vec{r})\vec{p})^{\dagger} \\
&= \frac{1}{2}\Lambda(\vec{r})\vec{p} + \frac{1}{2}\vec{p}^{\,\dagger}\Lambda^{\dagger}(\vec{r}) \\
&= \frac{1}{2}\Lambda(\vec{r})\vec{p} + \frac{1}{2}\Lambda^{*}(\vec{r})\vec{p} + \vec{\omega}(\vec{r}) \\
&= \Lambda_R(\vec{r})\vec{p} + \vec{\omega}(\vec{r}) \\
&= \Lambda_R(\vec{r})(\vec{p} + \vec{A}),
\end{aligned}$$

where $\vec{A} = \Lambda_R^{-1}(\vec{r})\vec{\omega}$, with $\omega_j = -\frac{i\hbar}{2}\partial_k \lambda_{jk}^*$ obtained from the commutator $[\lambda_{ij}^*(\vec{r}), p_k] = i\hbar\partial_k\lambda_{ij}^*(\vec{r})$. Separating $\vec{\omega} = \vec{\omega}_R + i\vec{\omega}_I$, where the compnents are $\omega_j^R = -\frac{\hbar}{2}\partial_k\lambda_{jk}^I$ and $\omega_j^I = -\frac{\hbar}{2}\partial_k\lambda_{jk}^R$, we have the real and imaginary gauge fields $\vec{A}_R = \Lambda_R^{-1}(\vec{r})\vec{\omega}_R$ and $\vec{A}_I = \Lambda_R^{-1}(\vec{r})\vec{\omega}_I$, generating pseudomagnetic fields and pseudospin precessions, respectively. Thus, the real gauge field $\vec{A}_R$ is given by

$$\begin{aligned}
\vec{A}_R &= \Lambda_R^{-1}(\vec{r})\vec{\omega}_R(\vec{r}) \\
&= \frac{1}{\det\Lambda_R}\begin{pmatrix} \lambda_{22}^R & -\lambda_{12}^R \\ -\lambda_{21}^R & \lambda_{11}^R \end{pmatrix}\begin{pmatrix} \omega_1^R \\ \omega_2^R \end{pmatrix} \\
&= \frac{1}{\det\Lambda_R}\begin{pmatrix} \omega_1^R\lambda_{22}^R - \lambda_{12}^R\omega_2^R \\ -\omega_1^R\lambda_{21}^R + \lambda_{11}^R\omega_2^R \end{pmatrix}.
\end{aligned}$$

Defining $\chi = \det\Lambda_R$ and using the expression of $\vec{\omega}_R$ in terms of λ_{ij}, the components of $\vec{A}_R$ are written as

$$\begin{aligned}
A_x^R &= -\frac{\hbar}{2\chi}\left\{\lambda_{22}^R(\partial_x\lambda_{11}^I + \partial_y\lambda_{12}^I) - \lambda_{12}^R(\partial_x\lambda_{21}^I + \partial_y\lambda_{22}^I)\right\} \\
A_y^R &= -\frac{\hbar}{2\chi}\left\{\lambda_{11}^R(\partial_x\lambda_{21}^I + \partial_y\lambda_{22}^I) - \lambda_{21}^R(\partial_x\lambda_{11}^I + \partial_y\lambda_{12}^I)\right\},
\end{aligned}$$

which are mainly determined by Λ_I because if $\Lambda_I = 0$, then $\vec{A}_R = 0$. An identical development for the imaginary gauge field $\vec{A}_I$ leads to the expressions

$$\begin{aligned}
A_x^I &= -\frac{\hbar}{2\chi}\left\{\lambda_{22}^R(\partial_x\lambda_{11}^R + \partial_y\lambda_{12}^R) - \lambda_{12}^R(\partial_x\lambda_{21}^R + \partial_y\lambda_{22}^R)\right\} \\
A_y^I &= -\frac{\hbar}{2\chi}\left\{\lambda_{11}^R(\partial_x\lambda_{21}^R + \partial_y\lambda_{22}^R) - \lambda_{21}^R(\partial_x\lambda_{11}^R + \partial_y\lambda_{12}^R)\right\}.
\end{aligned}$$

A7: Relation with other approaches

The hamiltonian (3.10) can be reduced to the used hamiltonian with other approaches [15, 129, 130], taking into account the expressions for the Fermi velocity tensor as $v_{ij} = v_F\lambda_{ij}^R$ and the

Dirac point shift $\vec{K}_D = -\vec{A}_R$, we obtain

$$\begin{aligned}
H &= v_F \vec{\sigma} \cdot \vec{p}\,' \\
&= v_F \vec{\sigma} \cdot \Lambda_R(\vec{r})(\vec{p} + \vec{A}) \\
&= v_F \vec{\sigma} \cdot \Lambda_R(\vec{r})(\vec{p} + \vec{A}_R) + i v_F \vec{\sigma} \cdot \Lambda_R(\vec{r}) \vec{A}_I \\
&= v_{ij} \sigma_i (p_j - K_j^D) + i v_F \vec{\sigma} \cdot \Lambda_R \Lambda_R^{-1} \vec{\omega}_I \\
&= v_{ij} \sigma_i (p_j - K_j^D) + i v_F \sigma_j \omega_j^I \\
&= v_{ij} \sigma_i (p_j - K_j^D) - \hbar v_F \sigma_j \Gamma_j,
\end{aligned}$$

where $\Gamma_j = -\frac{i}{\hbar}\omega_j^I = \frac{i}{2}\partial_k \lambda_{jk}^R = \frac{i}{2v_F}\partial_k v_{jk}$ is the imaginary gauge field generating pseudospin precession in the approaches [15, 129]. On the other hand, setting $\lambda_{11}(\vec{r}) = a(\vec{r})$, $\lambda_{12}(\vec{r}) = -ib(\vec{r})$, $\lambda_{21}(\vec{r}) = ia(\vec{r})$ and $\lambda_{22}(\vec{r}) = b(\vec{r})$ in the expression (3.8), we show that the components of $\vec{p}\,'$ have the form

$$\begin{aligned}
p'_x &= \frac{1}{2}\left\{a(\vec{r})p_x + p_x a(\vec{r}) - ib(\vec{r})p_y + ip_y b(\vec{r})\right\} \\
p'_y &= \frac{1}{2}\left\{ia(\vec{r})p_x - ip_x a(\vec{r}) + b(\vec{r})p_y + p_y b(\vec{r})\right\}.
\end{aligned}$$

substituting the expressions of p'_x and p'_y in the hamiltonian (3.10), we obtain

$$\begin{aligned}
H &= v_F \vec{\sigma} \cdot \vec{p}\,' \\
&= v_F \begin{pmatrix} 0 & p'_x - ip'_y \\ p'_x + ip'_y & 0 \end{pmatrix} \\
&= v_F \begin{pmatrix} 0 & a(\vec{r})p_x - ib(\vec{r})p_y \\ p_x a(\vec{r}) + ip_y b(\vec{r}) & 0 \end{pmatrix},
\end{aligned}$$

which is the same hamiltonian obtained in [67].

A8: Relation between $\tilde{\mathbf{p}}_\mathbf{c}$ and $\tilde{\mathbf{p}}\ '$

We choose a new linear momentum $\vec{p}_c$ instead of $\vec{p}\ '$ for solve the indefiniteness of the group velocity at Dirac point. The relation between $\vec{p}_c$ and $\vec{p}\ '$ is found from (3.11)

$$\begin{aligned}
\vec{p}_c &= \frac{1}{2}\xi^{-1}(\vec{r})\Lambda(\vec{r})\vec{p} + \frac{1}{2}\left(\xi^{-1}(\vec{r})\Lambda(\vec{r})\vec{p}\right)^\dagger \\
&= \frac{1}{2}\xi^{-1}(\vec{r})\Lambda(\vec{r})\vec{p} + \frac{1}{2}\vec{p}^{\ \dagger}\left\{\xi^{-1}(\vec{r})\Lambda(\vec{r})\right\}^\dagger \\
&= \frac{1}{2}\xi^{-1}(\vec{r})\Lambda(\vec{r})\vec{p} + \frac{1}{2}\xi^{-1}(\vec{r})\Lambda^*(\vec{r})\vec{p} + \vec{\overline{\omega}}(\vec{r}) \\
&= \xi^{-1}(\vec{r})\Lambda_R(\vec{r})\vec{p} + \vec{\overline{\omega}}(\vec{r}),
\end{aligned}$$

where the components of $\vec{\overline{\omega}}$ are $\overline{\omega}_j = -\frac{i\hbar}{2}\partial_k(\xi^{-1}\lambda^*_{jk})$ which are obtained from the commutator $[\xi^{-1}(\vec{r})\lambda^*_{ij}(\vec{r}), p_k] = i\hbar\partial_k(\xi^{-1}(\vec{r})\lambda^*_{ij}(\vec{r})$. Developing $\overline{\omega}_j = -\frac{i\hbar}{2}\xi^{-1}\partial_k\lambda^*_{jk} - \frac{i\hbar}{2}\lambda^*_{jk}\partial_k\xi^{-1} = \xi^{-1}\omega_j - \rho_j$ with $\rho_j = \frac{i\hbar}{2}\lambda^*_{jk}\partial_k\xi^{-1}$ and continuing with the calculation of $\vec{p}_c$, we have

$$\begin{aligned}
\vec{p}_c &= \xi^{-1}(\vec{r})\Lambda_R(\vec{r})\vec{p} + \xi^{-1}(\vec{r})\vec{\omega}(\vec{r}) - \vec{\rho}(\vec{r}) \\
&= \xi^{-1}(\vec{r})\Lambda_R(\vec{r})(\vec{p} + \vec{A}) - \vec{\rho}(\vec{r}) \\
&= \xi^{-1}(\vec{r})\vec{p}\ ' - \vec{\rho}(\vec{r}).
\end{aligned}$$

With $\vec{p}_c = \xi^{-1}(\vec{r})\Lambda_R(\vec{r})\vec{p} + \vec{\overline{\omega}}(\vec{r})$, we can see that the Jacobian of the transformation is $M = \xi^{-1}(\vec{r})\Lambda_R(\vec{r})$. As in the homogeneous case, $M^TJM = \mathrm{sgn}(\det\Lambda_R(\vec{r}))J$ and the transformation is symplectic (anti symplectic) if $\mathrm{sgn}(\det\Lambda_R(\vec{r})) = 1(-1)$. Hence, using the relation between $\vec{p}_c$ and $\vec{p}\ '$, the effective Dirac hamiltonian for inhomogeneous and anisotropic systems is

$$\begin{aligned}
H &= v_F\vec{\sigma}\cdot\vec{p}\ ' \\
&= v_F(\vec{r})\vec{\sigma}\cdot(\vec{p}_c + \vec{\rho}),
\end{aligned}$$

where $v_F(\vec{r}) = v_F\xi(\vec{r})$ and $\vec{\rho} = \frac{v_F}{2}i\hbar\Lambda^*\vec{\nabla}v_F^{-1}(\vec{r})$.

A9: Isotropic and inhomogeneous Dirac hamiltonian

Using the isotropic and inhomogeneous transformation $\Lambda(\vec{r}) = a(\vec{r})\mathbb{I}$, where $a(\vec{r})$ is a real function and $\mathbb{I}$ is the 2×2 identity matrix, we have that $\xi(\vec{r}) = a(\vec{r})$ then $\xi^{-1}\Lambda(\vec{r}) = \mathbb{I}$. Therefore, the linear momentum $\vec{p}_c$ from (3.11) is $\vec{p}_c = \vec{p} = -i\hbar\vec{\nabla}$ and the complex gauge field is given by $\vec{\rho}(\vec{r}) = \frac{i\hbar}{2} a(\vec{r}) \vec{\nabla} a^{-1}(\vec{r}) = \frac{i\hbar}{2} v_F(\vec{r}) \vec{\nabla} v_F^{-1}(\vec{r})$. Substituting these expressions in the hamiltonian (3.12)

$$\begin{aligned}
H &= v_F(\vec{r})\vec{\sigma} \cdot (\vec{p}_c + \vec{\rho}) \\
&= v_F(\vec{r})\vec{\sigma} \cdot (-i\hbar\vec{\nabla} + \tfrac{i\hbar}{2} v_F(\vec{r})\vec{\nabla} v_F^{-1}(\vec{r})) \\
&= -i\hbar\vec{\sigma} \cdot (v_F(\vec{r})\vec{\nabla} - \tfrac{1}{2} v_F^2(\vec{r})\vec{\nabla} v_F^{-1}(\vec{r})) \\
&= -i\hbar\vec{\sigma} \cdot (v_F(\vec{r})\vec{\nabla} + \tfrac{1}{2}\vec{\nabla} v_F(\vec{r})) \\
&= -i\hbar\sqrt{v_F(\vec{r})}\vec{\sigma} \cdot \vec{\nabla}[\sqrt{v_F(\vec{r})}],
\end{aligned}$$

where we have used the property $\sqrt{f(\vec{r})}\vec{\nabla}[\sqrt{f(\vec{r})}\Psi(\vec{r})] = f(\vec{r})\vec{\nabla}\Psi(\vec{r}) + \frac{1}{2}\Psi(\vec{r})\vec{\nabla} f(\vec{r})$ with $f(\vec{r})$ a function real and positive, and $\Psi(\vec{r})$ an arbitrary function.

Bibliography

[1] K.S. Novoselov, A.K. Geim, S.V. Morozov, D. Jiang, Y. Zhang, S.V. Dubonos, I.V. Gregorieva, and A.A. Firsov, *Science* **306**, 666 (2004).

[2] P.R. Wallace, *Phys. Rev.* **71**, 622 (1947).

[3] K.S. Novoselov, A.K. Geim, S.V. Morozov, D. Jiang, M.I. Katsnelson, I.V. Grigorieva, S.V. Dubonos, and A.A. Firsov, *Nature* **438**, 197 (2005).

[4] M.I. Katsnelson, K.S. Novoselov, and A.K. Geim, *Nat. Phys.* **2**, 620 (2006).

[5] O. Klein, *Z. Phys.* **53**, 157 (1929).

[6] N. Dombey and A. Calogeracos, *Phys. Rep.* **315**, 41 (1999).

[7] A.A. Balandin, S. Ghosh, W. Bao, I. Calizo, D. Teweldebrhan, F. Miao, and C.N. Lau, *Nano Lett.* **8**, 902 (2008).

[8] R.R. Nair, P. Blake, A.N. Grigorenko, K.S. Novoselov, T.J. Booth, T. Stauber, N.M.R. Peres, and A.K. Geim, *Science* **320**, 1308 (2008).

[9] C. Lee, X. Wei, J.W. Kysar, and J. Hone, *Science* **321**, 385 (2008).

[10] J.H. Chen, C. Jang, S. Xiao, M. Ishigami, and M.S. Fuhrer, *Nat. Nanotechnol.* **3**, 206 (2008).

[11] V. M. Pereira, A. H. Castro Neto, and N. M. R. Peres, *Phys. Rev. B* **80**, 045401 (2009).

[12] T.O. Wehling, A.M. Black-Schaffer, and A.V. Balatsky, *Adv. Phys.* **63**, 1 (2014).

[13] G. Montambaux, F. Pièchon, J.-N. Fuchs, and M.O. Goerbig, *Phys. Rev. B* **80**, 153412 (2009).

[14] Y. Hasegawa, R. Konno, H. Nakano, and M. Kohmoto, *Phys. Rev. B* **74**, 033413 (2006).

[15] B. Amorim, A. Cortijo, F. de Juan, A.G. Grushin, F. Guinea, A. Gutiérrez-Rubio, H. Ochoa, V. Parente, R. Roldán, P. San-José, J. Schiefele, M. Sturla, and M.A.H. Vozmediano, *Phys. Rep.* **617**, 1 (2016).

[16] B. Wunch, F. Guinea, and F. Sols, *New J. Phys.* **10**, 103027 (2008).

[17] M.Y. Han, B. Özyilmaz, Y. Zhang, and P. Kim, *Phys. Rev. Lett.* **98**, 206805 (2007).

[18] L.A. Ponomarenko, F. Schedin, M.I. Katsnelson, R. Yang, E.W. Hill, K.S. Novoselov, and A.K. Geim, *Science* **320**, 356 (2008).

[19] C.M. Ramos-Castillo, *Electronic properties of graphene-based nanostructures: quantum confinement, edge magnetism, and hydrogen adsorption on transition metal cluster-monovacancy systems.* PhD's thesis, Cinvestav-Mérida, México (2016).

[20] M. Dvorak, W. Oswald, and Z. Wu, *Sci. Rep.* **3**, 2289 (2013).

[21] X.L. Qi, and S.C. Zhang, *Rev. Mod. Phys.* **83**, 1057 (2011).

[22] A.H. Castro Neto, F. Guinea, N.M.R. Peres, K.S. Novoselov, and A.K. Geim, *Rev. Mod. Phys.* **81**, 109 (2009).

[23] N.M.R. Peres, *Rev. Mod. Phys.* **82**, 2673 (2010).

[24] M.O. Goerbig, *Rev. Mod. Phys.* **83**, 1193 (2011).

[25] J.W. Jiang, *Front. Phys.* **10**, 106801 (2015).

[26] A. Kobayashi, S. Katayama, Y. Suzumura, and H. Fukuyama, *J. Phys. Soc. Jpn.* **76**, 034711 (2007).

[27] A. Kara, H. Enriquez, A.P. Seitsonen, L.C. Lew Yan Voon, S. Vizzini, B. Aufray, H. Oughaddou, *Surf. Sci. Rep.* **67**, 1 (2012).

[28] J. Wang, S. Deng, Z. Liu, and Z. Liu, *Nat. Sci. Rev.* **2**, 22 (2015).

[29] M. Ezawa, *J. Phys. Soc. Jpn.* **84**, 121003 (2015).

[30] X. Wan, A.M. Turner, A. Vishwanath, and S.Y. Savrasov, *Phys. Rev. B* **83**, 205101 (2011).

[31] L. Kou, C. Chen, and S.C. Smith, *J. Phys. Chem. Lett.* **6**, 2794 (2015).

[32] K.K. Gomes, W. Mar, W. Ko, F. Guinea, and H.C. Manoharan, *Nature* **483**, 306 (2012).

[33] L. Tarruel, D. Greif, T. Uehlinger, G. Jotzu, and T. Esslinger, *Nature* **483**, 302 (2012).

[34] Q. Peng, A.K. Dearden, J.Crean, L. Han, S. Liu, X. Wen, and S. De, *Nanotechnol. Sci. Appl.* **7**, 1 (2014).

[35] N. Levy, S.A. Burke, K.L. Meaker, M. Panlasigui, A. Zettl, F. Guinea, A.H. Castro Neto, and M.F. Crommie, *Science* **329**, 544 (2010).

[36] M.C. Rechtsman, J.M. Zeuner, A. Tünnermann, S. Nolte, M. Segev, and A. Szameit, *Nat. Photon.* **7**, 153 (2013).

[37] F.M.D. Pellegrino, G.G.N Angilella, and R. Pucci, *Phys. Rev. B* **81**, 035411 (2010).

[38] M. Oliva-Leyva and G.G. Naumis, *Phys. Rev. B* **88**, 085430 (2013).

[39] M. Ramezani-Masir, D. Moldovan, and F.M. Peeters, *Solid State Commun.* **175**, 76 (2013).

[40] F. Guinea, M. I. Katsnelson, and A. K. Geim, *Nat. Phys.* **6**, 30 (2010).

[41] Y.H. Lee, X.Q. Zhang, W. Zhang, M.T. Chang, C.T. Lin, K.D. Chang, Y.C. Yu, J.T. Wang, C.S. Chang, and L.J. Li, *Adv. Mater.* **24**, 2320 (2012).

[42] H. Liu, A.T. Neal, Z. Zhu, Z. Luo, X. Xu, D. Tománek, and P.D. Ye, *ACS nano* **8**, 4033 (2014).

[43] A. Castellanos-Gomez, R. Roldán, E. Cappelluti, M. Buscema, F. Guinea, H.S.J. van der Zant, and G.A. Steele, *Nano Lett.* **13**, 5361 (2013).

[44] A.S. Rodin, A. Carvalho, and A.H. Castro Neto, *Phys. Rev. Lett.* **112**, 176801 (2014).

[45] G. Cocco and V. Fiorentini, *Phys. Rev. B* **92**, 045411 (2015).

[46] I.I. Naumov and A.M. Bratkovsky, *Phys. Rev. B* **84**, 245444 (2011).

[47] M. A. H. Vozmediano, M. I. Katsnelson, and F. Guinea, *Phys. Rep.* **496**, 109 (2010).

[48] H. Shioya, M.F. Craciun, S. Russo, M. Yamamoto, and S. Tarucha, *Nano Lett.* **14**, 1158 (2014).

[49] H.H. Pérez Garza, E.W. Kievit, G.F. Schneider, and U. Staufer, *Nano Lett.* **14**, 4107 (2014).

[50] V.N. Kotov, B. Uchoa, V.M. Pereira, F. Guinea, and A.H. Castro Neto, *Rev. Mod. Phys.* **84**, 1067 (2012).

[51] C. Si, Z. Liu, W. Duan, and F. Liu, *Phys. Rev. Lett.* **111**, 196802 (2013).

[52] D. Nelson, D.R. Piran, and S. Weinberg, *Statistical Mechanics of Membranes and Surfaces* (World Scientific, Singapore, 2004).

[53] M. Sprinkle, D. Siegel, Y. Hu, J. Hicks, A. Tejeda, A. Taleb-Ibrahimi, P. Le Févre, F. Bertran, S. Vizzini, H. Enriquez, S. Chiang, P. Soukiassian, C. Berger, W.A. de Heer, A. Lanzara, and E.H. Conrad, *Phys. Rev. Lett.* **103**, 226803 (2009).

[54] Y. Zhang, Y.W. Tan, H.L. Stormer, and P. Kim, *Nature* **438**, 201 (2005).

[55] A.F. Young and P. Kim, *Nat. Phys.* **5**, 222 (2009).

[56] J.L. Garcia-Pomar, A. Cortijo, and M. Nieto-Vesperinas, *Phys. Rev. Lett.* **100**, 236801 (2008).

[57] V.V. Cheianov, V. Fal'ko, and B.L. Altshuler, *Science* **315**, 1252 (2007).

[58] K. Kishigi, K. Ueno, E. Miyamoto, and Y. Hasegawa, *J. Phys.: Conf. Ser.* **334**, 012047 (2011).

[59] G. Cocco, E. Cadelano, and L. Colombo, *Phys. Rev. B* **81**, 241412 (2010).

[60] R. M. Ribeiro, V. M. Pereira, N. M. R. Peres, P. R. Briddon, and A. H. Castro Neto, *New J. Phys.* **11**, 115002 (2009).

[61] M. Mohr, K. Papagelis, J. Maultzsch, and C. Thomsen, *Phys. Rev. B* **80**, 205410 (2009).

[62] N. Kerszberg and P. Suryanarayana, *RSC Adv.* **5**, 43810 (2015).

[63] P. Kumar, R. Skomski, P. Manchanda, A. Kashyap, and P.A. Dowben, *Curr. Appl. Phys.* **14**, S136 (2013).

[64] Z.H. Ni, T. Yu, Y.H. Lu, Y.Y. Wang, Y.P. Feng, and Z.X. Shen, *ACS Nano* **2**, 2301 (2008).

[65] Z.H. Ni, T. Yu, Y.H. Lu, Y.Y. Wang, Y.P. Feng, and Z.X. Shen, *ACS Nano* **3**, 483 (2009).

[66] S.M. Choi, S.H. Jhi, and Y.W. Son, *Phys. Rev. B* **81**, 081407 (2010).

[67] Y. Betancur-Ocampo, M.E. Cifuentes-Quintal, G. Cordourier-Maruri, and R. de Coss, *Ann. Phys.* **359**, 243 (2015).

[68] M.O. Goerbig, J.-N. Fuchs, G. Montambaux, and F. Pièchon, *Phys. Rev. B* **78**, 045415 (2008).

[69] V. M. Pereira and A. H. Castro Neto, *Phys. Rev. Lett.* **103**, 046801 (2009).

[70] H. Yan, Z.D. Chu, W. Yan, M. Liu, L. Meng, M. Yang, Y. Fan, J. Wang, R.F. Dou, Y. Zhang, Z. Liu, J.C. Nie, and L. He, *Phys. Rev. B* **87**, 075405 (2013).

[71] W.J. Jang, H. Kim, Y.R. Shin, M. Wang, S.K. Jang, M. Kim, S. Lee, S.W. Kim, Y.J. Song, and S.J. Kahng, *Carbon* **74**, 139 (2014).

[72] H. Rostami and R. Asgari, *Phys. Rev. B* **86**, 155435 (2012).

[73] D.C. Elias, R.V. Gorbachev, A.S. Mayorov, S.V. Morozov, A.A. Zhukov, P. Blake, L.A. Ponomarenko, I.V. Grigorieva, K.S. Novoselov, F. Guinea, and A.K. Geim, *Nat. Phys.* **7**, 701 (2011).

[74] A. Luican, G. Li, and E.Y. Andrei, *Phys. Rev. B* **83**, 041405 (2011).

[75] J. Martin, N. Akerman, G. Ulbricht, T. Lohmann, J.H. Smet. K. von Klitzing, and A. Yacoby, *Nat. Phys.* **4**, 144 (2008).

[76] D.A. Papaconstantopoulos, M.J. Mehl, S.C. Erwin, and M.R. Pederson, *Materials Research Society* (Pittsburgh, p. 221. (1998)).

[77] V.M. Pereira, R.M. Ribeiro, N.M.R. Peres, and A.H. Castro Neto *Europhys. Lett.* **92**, 67001 (2010).

[78] M. Oliva-Leyva and G.G. Naumis, *J. Phys. Condens. Matt.* **26**, 125302 (2014).

[79] S. Reich, J. Maultzsch, C. Thomsen, and P. Ordejón, *Phys. Rev. B* **66**, 035412 (2002).

[80] M. Assili, S. Haddad, and W. Kang, *Phys. Rev. B* **91**, 115422 (2015).

[81] J. Sári, M.O. Goerbig, and C. Töke, *Phys. Rev. B* **92**, 035306 (2015).

[82] T.L. Linnik, *J. Phys.: Condens. Matter* **24**, 205302 (2012).

[83] F. de Juan, M. Sturla, and M.A.H. Vozmediano, *Phys. Rev. Lett.* **108**, 227205 (2012).

[84] H. Suzuura and T. Ando, *Phys. Rev. B* **65**, 235412 (2002).

[85] T. Sohier, M. Calandra, C.H. Park, N. Bonini, N. Marzari, and F. Mauri, *Phys. Rev. B* **90**, 125414 (2014).

[86] F. Deng, Y. Li, Y. Sun, X. Wang, Z. Guo, Y. Shi, H. Jiang, K. Chang, and H. Chen, *Opt. Lett.* **40**, 3380 (2015).

[87] Z. Qi, A.L. Kitt, H.S. Park, V.M. Pereira, D.K. Campbell, and A.H. Castro Neto, *Phys. Rev. B* **90**, 125419 (2014).

[88] T.L. Linnik, *Phys. Rev. B* **90**, 075406 (2014).

[89] M. Trescher, B. Sbierski, P.W. Brouwer, and E.J. Bergholtz, *Phys. Rev. B* **91**, 115135 (2015).

[90] J. Mañes, F. de Juan, M. Sturla, and M.A.H Vozmediano, *Phys. Rev. B* **88**, 155405 (2013).

[91] Z. Wu, F. Zhai, F.M. Peeters, H.Q. Xu, and K. Chang, *Phys. Rev. Lett.* **106**, 176802 (2011).

[92] F. Zhai, Y. Ma, and K. Chang, *New J. Phys.* **13**, 083029 (2011).

[93] Y. Song, F. Zhai, and Y. Guo, *Appl. Phys. Lett.* **103**, 183111 (2013).

[94] H. Yan, Y. Sun, L. He, J.C. Nie, and M.H.W. Chan, *Phys. Rev. B* **85**, 035422 (2012).

[95] O. Bahat-Treidel, O. Peleg, and M. Segev, *Opt. Lett.* **33**, 2251 (2008).

[96] M.J. Ablowitz, S.D. Nixon, and Y. Zhu, *Phys. Rev. A* **79**, 053830 (2009).

[97] O. Bahat-Treidel, O. Peleg, M. Grobman, N. Shapira, M. Segev, and T. Pereg-Barnea, *Phys. Rev. Lett.* **104**, 063901 (2010).

[98] F.M.D. Pellegrino, G.G.N Angilella, and R. Pucci, *Phys. Rev. B* **84**, 195404 (2011).

[99] F. Goos and H. Hänchen, *Ann. Phys.* (Leipzig) **436**, 333 (1947).

[100] C.W.J. Beenakker, R.A. Sepkhanov, A.R. Akhmerov, and J. Tworzydlo, *Phys. Rev. Lett.* **102**, 146804 (2009).

[101] C.W.J. Beenakker, *Rev. Mod. Phys.* **80**, 1337 (2008).

[102] J.L. Manes, *Phys. Rev. B* **76**, 045430 (2007).

[103] J.A. Crosse, *Phys. Rev. B* **90**, 045201 (2014).

[104] A.L. Kitt, V.M. Pereira, A.K. Swan, and B.B. Goldberg, *Phys. Rev. B* **85**, 115432 (2012).

[105] A.L. Kitt, V.M. Pereira, A.K. Swan, and B.B. Goldberg, *Phys. Rev. B* **87**, 159909 (2013).

[106] F. de Juan, J.L. Mañes, and M.A.H. Vozmediano, *Phys. Rev. B* **87**, 155436 (2013).

[107] L. Colombo and S. Giordano, *Rep. Prog. Phys.* **74**, 116501 (2011).

[108] E. Cadelano, P. L. Palla, S. Giordano, and L. Colombo, *Phys. Rev. Lett.* **102**, 235502 (2009).

[109] G. Montambaux, F. Pièchon, J.-N. Fuchs, and M.O. Goerbig, *Eur. Phys. J. B* **72**, 509 (2009).

[110] R. de Gail, J.-N. Fuch, M.O. Goerbig, F. Pièchon, and G. Montambaux, *Physica B* **407**, 1948 (2012).

[111] J.M. Hou, W.X. Yang, and X.J. Liu, *Phys. Rev. A* **79**, 043621 (2009).

[112] S. Banerjee, R.R.P. Singh, V. Pardo, and W.E. Pickett, *Phys. Rev. Lett.* **103**, 016402 (2009).

[113] L. Onsager, *Phil. Mag.* **43**, 1006 (1952).

[114] I.S. Gradshteyn, I.M. Ryzhik, and A. Jeffrey, *Tables of integrals, series, and products* (Academic Press, 2007).

[115] P. Dietl, F. Pièchon, and G. Montambaux, *Phys. Rev. Lett.* **100**, 236405 (2008).

[116] T. Morinari, T. Himura, and T. Tohyama, *J. Phys. Soc. Jpn.* **78**, 023704 (2009).

[117] W.A. Harrison, *Elementary Electronic Structure* (World Scientific, Singapore, 1999).

[118] M.O. Goerbig, J.-N. Fuchs, G. Montambaux and F. Pièchon, *Europhys. Lett.* **85**, 57005 (2009).

[119] V. Lukose, R. Shanckar, and G. Baskaran, *Phys. Rev. Lett.* **98**, 116802 (2007).

[120] N.M.R Peres and E.V. Castro, *J. Phys.: condens. Matter* **19**, 406231 (2007).

[121] N. Gu, M. Rudner, A. Young, P. Kim, and L. Levitov, *Phys. Rev. Lett.* **106**, 066601 (2011).

[122] F.M.D. Pellegrino, G.G.N Angilella, and R. Pucci, *Phys. Rev. B* **84**, 195407 (2011).

[123] F.M.D. Pellegrino, G.G.N Angilella, and R. Pucci, *J. Phys.: Conf. Ser.* **377**, 012083 (2012).

[124] L. Blakslee, D. G. Proctor, E. J. Seldin, G. B. Stence, and T. Wen, *J. Appl. Phys.* **41**, 3373 (1970).

[125] Z.Z Cao, Y.F. Cheng, and G.Q. Li, *Physica B* **407**, 4254 (2012).

[126] A. H. Castro Neto and F. Guinea, *Phys. Rev. B* **75**, 045404 (2007).

[127] M. Oliva-Leyva and G.G. Naumis, *2D Mater.* **2**, 025001 (2015).

[128] A.D. Phan and T.L. Phan, *Phys. Status Solidi RRL* **8**, 1003 (2014).

[129] M. Oliva-Leyva and G.G. Naumis, *Phys. Lett. A* **379**, 2645 (2015).

[130] G.E. Volovik and M.A. Zubkov, *Ann. Phys.* **356**, 255 (2015).

[131] A. Cortijo and M.A. Zubkov, *Ann. Phys.* **366**, 45 (2016).

[132] M.A. Zubkov, *Ann. Phys.* **360**, 655 (2015).

[133] R.J. Atkin and N. Fox, *An Introduction to the Theory of Elasticity* (New York, Dover, 1980).

[134] V.V. Novozhilov, *Foundations of the Nonlinear Theory of Elasticity* (New York, Dover, 1999).

[135] L. D. Landau and E. M. Lifshitz, *Theory of Elasticity* (Pergamon Press, 3rd Edition, USA, 1986).

[136] H.B. Huntington, *The Elastic Constants of Crystals* (New York, Academic, 1958).

[137] X. Wei, B. Fragneaud, C.A. Marianetti, and J.W. Kysar, *Phys. Rev. B* **80**, 205407 (2009).

[138] K.H. Michel and B. Verberck, *Phys. Status Solidi B* **245**, 2177 (2009).

[139] F. Liu, P. Ming, and J. Li, *Phys. Rev. B* **76**, 064120 (2007).

[140] J.C. Slater and G.F. Koster, *Phys. Rev.* **94**, 1498 (1954).

[141] R. Roldán, A. Castellanos-Gomez, E. Cappelluti, and F. Guinea, *J. Phys.: Condens. Matter* **27**, 313201 (2015).

[142] C.H. Park, L. Yang, Y.W. Son, M.L. Cohen, and S.G. Louie, *Nat. Phys.* **4**, 213 (2008).

[143] Y. Barlas, T. Pereg-Barnea, M. Polini, R. Asgari, and A.H. MacDonald, *Phys. Rev. Lett.* **98**, 236601 (2007).

[144] N.M.R. Peres, *J. Phys.: Condens. Matter* **21**, 095501 (2009).

[145] A. Raoux, M. Polini, R. Asgari, A.R. Hamilton, R. Fazio, and A.H. MacDonald, *Phys. Rev. B* **81**, 073407 (2010).

[146] B.M. Levitan, *Inverse Sturm-Liouville problems* (1st Edition, VNU Science Press BV, Netherlands, 1987).

[147] S. Gómez, P. Burset, W.J. Herrera, and A. Levy Yeyati, *Phys. Rev. B* **85**, 115411 (2012).

[148] G.H. Lee, G.H. Park, and H.J. Lee, *Nat. Phys.* **11**, 925 (2015).

[149] S. Chen, Z. Han, M.M. Elahi, K.M. Masum-Habib, L. Wang, B. Wen, Y. Gao, T. Taniguchi, K. Watanabe, J. Hone, A.W. Ghosh, C.R. Dean, *Science* **353**, 1522 (2016).

[150] C.H. Park, Y.W. Son, L. Yang, M.L. Cohen, and S.G. Louie, *Nano Lett.* **8**, 2920 (2008).

[151] M.A. Khan and M.N. Leuenberger, *Phys. Rev. B* **90**, 075439 (2014).

[152] D. Gunlycke and C.T. White, *Phys. Rev. B* **90**, 035452 (2014).

[153] D. Gunlycke and C.T. White, *Phys. Rev. B* **91**, 075425 (2015).

[154] D. Gunlycke and C.T. White, *Phys. Rev. Lett.* **106**, 136806 (2011).

[155] C.H. Park, L. Yang, Y.W. Son, M.L. Cohen, and S.G. Louie, *Phys. Rev. Lett.* **101**, 126804 (2008).

[156] M.M. Grujić, M.Z. Tadić, and F.M. Peeters, *Phys. Rev. Lett.* **113**, 046601 (2014).

[157] D. Moldovan, M. Ramezani Masir, L. Covaci, and F.M. Peeters, *Phys. Rev. B* **86**, 115431 (2012).

[158] R.N. Sajjad and A.W. Ghosh, *Appl. Phys. Lett.* **99**, 123101 (2011).

[159] A. Fang, Z.Q. Zhang, S.G. Louie, and C.T. Chan, *Phys. Rev. B* **93**, 035422 (2016).

[160] Y. Jiang, T. Low, K. Chang, M.I. Katsnelson, and F. Guinea, *Phys. Rev. Lett.* **110**, 046601 (2013).

[161] K.M. Masum, R.N. Sajjad, and A.W. Ghosh, *Phys. Rev. Lett.* **114**, 176801 (2015).

[162] E.C. Peters, A.J.M. Giesbers, U. Zeitler, M. Burghard, and K. Kern, *Phys. Rev. B* **87**, 201403 (2013).

[163] V.V. Cheianov and V.I. Fal'ko, *Phys. Rev. B* **74**, 041403 (2006).

[164] T. Low, S. Hong, J. Appenzeller, S. Datta, and M.S. Lundstrom, *IEEE T. Electron Dev.* **56**, 1292 (2009).

[165] P.E. Allain and J.N. Fuchs, *Eur. Phys. J. B* **83**, 301 (2011).

[166] D.F. Urban, D. Bercioux, M. Wimmer, and W. Häusler, *Phys. Rev. B* **84**, 115136 (2011).

[167] R. Shen, L.B. Shao, B. Wang, and D.Y. Xing, *Phys. Rev. B* **81**, 041410 (2010).

[168] C.H. Ho, Y.H. Ho, Y.H. Chiu, Y.N. Chen, and M.F. Lin, *Ann. Phys.* **326**, 721 (2011).

[169] J.S. Lee, C.W. Jang, J.M. Kim, D.H. Shin, S. Kim, S.H. Choi, and R.G. Elliman, *Carbon* **66**, 267 (2014).

[170] M.E. Cifuentes-Quintal, O. de la Peña-Seaman, R. Heid, R. de Coss, and K.P. Bohnen, *Phys. Rev. B* **94**, 085401 (2016).

[171] M. Mucha-Kruczynski, I.L. Aleiner, and V.I. Fal'ko, *Phys. Rev. B* **84**, 041404 (2011).

[172] Y. Hatsugai, *J. Phys. Conf. Ser.* **334**, 012004 (2011).

[173] C. Bena and G. Montambaux, *New J. Phys.* **11**, 095003 (2009).

[174] L.D. Landau and E.M. Lifshitz, *Quantum Mechanics Non-relativistic Theory* (3rd Edition, Pergamon Press, USA, 1977).

[175] H. Ho, Y.H. Lai, Y.H. Chiu, and M.F. Lin, *Phys. E* **40**, 1722 (2008).

[176] G. Li and E. Y. Andrei, *Nat. Phys.* **3**, 623 (2009).